

**LEBANESE AMERICAN UNIVERSITY**

**Finite Element Modelling and Optimization of Rotary  
Friction Welding Parameters of High-Density Polyethylene  
Pipes (HDPE)**

By

**Zeina Gerges**

A thesis  
submitted in partial fulfillment of the requirements  
for the degree of Master of Science in Mechanical Engineering

School of Engineering  
December 2022

© 2022

Zeina Gerges

All Rights Reserved

**THESIS APPROVAL FORM**

Student Name: Zeina Gerges I.D. #: 201407843

Thesis Title : Finite Element Modelling and Optimization of Rotary Friction Welding Parameters of High-Density Polyethylene Pipes (HDPE)


Program: Master of Science


Department: Mechanical Engineering


School: School of Engineering

The undersigned certify that they have examined the final electronic copy of this thesis and approved it in Partial Fulfillment of the requirements for the degree of:

Master of Science in the major of Mechanical Engineering

Thesis Advisor's Name Ali Ammouri | Signature  | DATE: 16 / 12 / 2022  
Day Month Year

Committee Member's Name Evan Fakhoury | Signature  | DATE: 16 / 12 / 2022  
Day Month Year

Committee Member's Name Charbel Tawk | Signature  | DATE: 16 / 12 / 2022  
Day Month Year

## THESIS COPYRIGHT RELEASE FORM

### LEBANESE AMERICAN UNIVERSITY NON-EXCLUSIVE DISTRIBUTION LICENSE

By signing and submitting this license, you (the author(s) or copyright owner) grants the Lebanese American University (LAU) the non-exclusive right to reproduce, translate (as defined below), and/or distribute your submission (including the abstract) worldwide in print and electronic formats and in any medium, including but not limited to audio or video. You agree that LAU may, without changing the content, translate the submission to any medium or format for the purpose of preservation. You also agree that LAU may keep more than one copy of this submission for purposes of security, backup and preservation. You represent that the submission is your original work, and that you have the right to grant the rights contained in this license. You also represent that your submission does not, to the best of your knowledge, infringe upon anyone's copyright. If the submission contains material for which you do not hold copyright, you represent that you have obtained the unrestricted permission of the copyright owner to grant LAU the rights required by this license, and that such third-party owned material is clearly identified and acknowledged within the text or content of the submission. IF THE SUBMISSION IS BASED UPON WORK THAT HAS BEEN SPONSORED OR SUPPORTED BY AN AGENCY OR ORGANIZATION OTHER THAN LAU, YOU REPRESENT THAT YOU HAVE FULFILLED ANY RIGHT OF REVIEW OR OTHER OBLIGATIONS REQUIRED BY SUCH CONTRACT OR AGREEMENT. LAU will clearly identify your name(s) as the author(s) or owner(s) of the submission, and will not make any alteration, other than as allowed by this license, to your submission.

Name: Zeina Gerges

Signature:



Date: 06 / 12 / 2022

Day

Month

Year

## PLAGIARISM POLICY COMPLIANCE STATEMENT

I certify that:

1. I have read and understood LAU's Plagiarism Policy.
2. I understand that failure to comply with this Policy can lead to academic and disciplinary actions against me.
3. This work is substantially my own, and to the extent that any part of this work is not my own I have indicated that by acknowledging its sources.

Name: Zeina Gerges

Signature:



Date: 06 / 12 / 2022

Day

Month

Year

# DEDICATION

This thesis is dedicated to all the people who supported me in this journey. A special gratitude to my parents who never ceased to encourage me, to my brother who never left my side, to my best friend Helen who provided me with emotional support, and to my colleague and friend Serge who guided me along the process. This thesis would not have been possible without these people, and words can't express how grateful I am to have them in my life. Thank you to all other relatives and friends who shared advice and support.

# **ACKNOWLEDGMENT**

I would like to thank my advisor Dr. Ali Ammouri because this project would not have been possible without his guidance and support.

# Finite Element Modelling and Optimization of Rotary Friction Welding Parameters of High-Density Polyethylene Pipes (HDPE)

Zeina Gerges

## ABSTRACT

Rotary friction welding (RFW) is a highly efficient and sustainable process for joining both metals and plastics. The welding process parameters of RFW must be carefully selected to ensure a good quality weld with minimum energy consumption. Few studies in the literature simulate RFW of plastics and none aim to optimize the welding process parameters. This study aims to optimize the process parameters of the continuous drive rotary friction welding of high-density polyethylene (HDPE) pipes. To simulate the RFW process, a 2D axisymmetric fully coupled thermo-mechanical model was developed using DEFORM software package. The model used an elastic-plastic material behavior model that varies with temperature, strain, and strain rate, and a temperature-dependent coefficient of friction. The material behavior was modeled using a Zerilli Armstrong equation and the 2D model was validated against experimental data from the literature. The model successfully predicted the material behavior and captured the thermal and mechanical behavior of HDPE during the welding process. The model was then used to optimize the process parameters of the RFW of HDPE pipes using the Taguchi method. A linear regression model was used to estimate the response in terms of the input process parameters for a specific pipe geometry of 63 mm diameter and 5.8 mm thickness. The optimized process parameters that minimized the power consumption for the selected pipe were found to be 800 RPM rotational speed, 20mm/min feed rate and a friction time of 9 seconds. By relying upon these optimized parameters, industry professionals can produce high quality HDPE welds which would result in a reduction in welding operations cost, and a shift towards more sustainable manufacturing operations.

Keywords: Rotary Friction Welding, High Density Polyethylene, Taguchi, Optimization, Finite Element Model



# TABLE OF CONTENTS

<b>DEDICATION</b> .....	<b>V</b>
<b>ACKNOWLEDGMENT</b> .....	<b>VI</b>
<b>ABSTRACT</b> .....	<b>VII</b>
<b>TABLE OF CONTENTS</b> .....	<b>VIII</b>
<b>LIST OF TABLES</b> .....	<b>XI</b>
<b>LIST OF FIGURES</b> .....	<b>XII</b>
<b>LIST OF ABBREVIATIONS</b> .....	<b>XIV</b>
<b>INTRODUCTION AND BACKGROUND</b> .....	<b>1</b>
<b>1.1 Welding of Plastics</b> .....	<b>4</b>
<b>1.2 HDPE Pipe Systems</b> .....	<b>5</b>
<b>1.3 Friction Welding</b> .....	<b>6</b>
1.3.1 Principal Friction Welding Processes.....	7
1.3.2 Rotary Friction Welding VS. Butt Fusion Welding .....	10
1.3.3 Advantages and Disadvantages .....	11
1.3.4 Stages of RFW.....	12
1.3.5 Energy Variants .....	14
1.3.6 Friction Welding Parameters .....	16
1.3.7 Heat Generation in Friction Welding .....	18
1.3.8 Tensile Strength of Welded Specimen .....	19
<b>LITERATURE REVIEW</b> .....	<b>20</b>
<b>2.1 Numerical Modelling of Metals</b> .....	<b>20</b>

<b>2.2 Numerical Modelling of Plastics.....</b>	<b>31</b>
<b>2.3 Experimental Studies on RFW of Plastics.....</b>	<b>32</b>
<b>2.4 Aim, Objectives and Scope .....</b>	<b>37</b>
<b>2D FEM MODEL .....</b>	<b>40</b>
<b>3.1 Modelling Using DEFORM 2D .....</b>	<b>40</b>
<b>3.2 Numerical Model .....</b>	<b>41</b>
3.2.1 Modelling Method and Geometry .....	42
3.2.2 Mesh Design.....	43
3.2.3 Material Properties .....	44
3.2.4 Process Parameters .....	57
3.2.5 Boundary Conditions.....	58
3.2.6 Inter-Object Relations and Friction Coefficient.....	59
3.2.7 Simulation Controls.....	60
3.2.8 Model Assumptions.....	61
3.2.9 Model Results and Validation .....	61
<b>DESIGN OF EXPERIMENT: TAGUCHI.....</b>	<b>69</b>
<b>4.1 Definition and Advantages.....</b>	<b>69</b>
<b>4.2 DOE Steps and Design Generation .....</b>	<b>70</b>
<b>OPTIMIZATION RESULTS &amp; DISCUSSION .....</b>	<b>74</b>
<b>5.1 Designed Experiment Results.....</b>	<b>74</b>
<b>5.2 Analysis of signal to noise ratio .....</b>	<b>75</b>
<b>5.3 Analysis of Variance (ANOVA) .....</b>	<b>77</b>
<b>5.4 Regression Model.....</b>	<b>79</b>
<b>5.5 Confirmation Test .....</b>	<b>80</b>
<b>CONCLUSION, LIMITATIONS &amp; FUTURE WORK .....</b>	<b>82</b>
<b>REFERENCES .....</b>	<b>84</b>

<b>APPENDIX .....</b>	<b>98</b>
<b>APPENDIX A: Flow Stress Data .....</b>	<b>98</b>

# LIST OF TABLES

Table 1 - Zerilli Armstrong model constants .....	46
Table 2 - Zerilli Armstrong model constants extrapolated to higher temperatures.....	50
Table 3 - Zerilli Armstrong model constants extrapolated to higher strain rates at 25°C.	51
Table 4 - Extrapolated elastic moduli.....	53
Table 5 - Thermal properties of HDPE .....	57
Table 6 - Model input process parameters .....	58
Table 7 - Factors and factor levels .....	71
Table 8 - Taguchi design .....	73
Table 9 - Maximum force, torque, and temperature of the L9 test matrix .....	75
Table 10 – Power consumption and signal to noise ratios .....	75
Table 11 - Response table for signal to noise ratios (smaller is better).....	76
Table 12 - Analysis of variance for S/N ratios .....	78
Table 13 - Confirmation test results .....	80
Table 14 - Zerilli Armstrong model constants extrapolated to higher strain rates at different temperatures.....	104
Table 15 - Flow Stress Data at 25°C .....	105
Table 16 - Flow Stress Data at 50°C .....	105
Table 17 - Flow Stress Data at 70°C .....	106
Table 18 - Flow Stress Data at 90°C .....	106
Table 19 - Flow Stress Data at 120°C .....	107
Table 20 - Flow Stress Data at 150°C .....	107
Table 21 - Flow Stress Data at 180°C .....	108
Table 22 - Flow Stress Data at 210°C .....	108
Table 23 - Flow Stress Data at 240°C .....	109
Table 24 - Flow Stress Data at 280°C .....	109
Table 25 - Flow Stress Data at 350°C .....	110
Table 26 - Flow Stress Data at 500°C .....	110

# LIST OF FIGURES

Figure 1- Rotary friction welding process.....	2
Figure 2 - Distribution of heat generation in friction welding .....	9
Figure 3 - Typical meltdown (displacement) as a function of time in friction welding....	13
Figure 4 - Variation of welding parameters with time for CDFW .....	14
Figure 5 - Characteristics of CDFW parameters .....	14
Figure 6 - Variation of welding parameters with time for IFW .....	16
Figure 7 - Characteristics of IFW parameters .....	16
Figure 8 - Model Geometry .....	42
Figure 9 - Model Mesh (rotating pipe) .....	44
Figure 10 - Zerilli Armstrong model results.....	47
Figure 11 - Constant C vs Temperature at $0.001s^{-1}$ .....	48
Figure 12 - Constant $\epsilon_r$ vs Temperature at $0.001s^{-1}$ .....	48
Figure 13 - Constant C vs Temperature at $935s^{-1}$ .....	49
Figure 14 - Constant $\epsilon_r$ vs Temperature at $935s^{-1}$ .....	49
Figure 15 - True Stress True Strain Curves at $25^{\circ}C$ and different strain rates.....	51
Figure 16 - Variation of Elastic Modulus with Temperature .....	52
Figure 17 - Yield Stress variation with strain rate at different temperatures .....	55
Figure 18 - Yield Stress variation with temperature at $0.001s^{-1}$ .....	55
Figure 19 - Variation of coefficient of friction with temperature .....	60
Figure 20 - Predicted vs Experimental Load Curves - Experiment A3.....	62
Figure 21 - Predicted vs Experimental Load Curves - Experiment B3.....	62
Figure 22 - Predicted vs Experimental Thermal Profiles - Experiment A3 .....	63
Figure 23 - Predicted vs Experimental Thermal Profiles - Experiment B3 .....	63
Figure 24 - Deformation and Temperature Evolution at friction time 0.5, 1, 3.5 and 7.5 sec, respectively.....	65
Figure 25 - 3D representation of the welded pipe .....	65
Figure 26 - Thermal History at the Weld Interface .....	66
Figure 27 - Point-tracking of weld interface .....	68
Figure 28 - Designed experiment .....	69
Figure 29 - Main effects plot for S/N ratios .....	76
Figure 30 - Main effects plot for means .....	77
Figure 31 - Normal probability plot .....	79
Figure 32 - Model Fit at $25^{\circ}C$ and $0.001s^{-1}$ .....	98
Figure 33 - Model Fit at $50^{\circ}C$ and $0.001s^{-1}$ .....	98
Figure 34 - Model Fit at $70^{\circ}C$ and $0.001s^{-1}$ .....	99
Figure 35 - Model Fit at $90^{\circ}C$ and $0.001s^{-1}$ .....	99
Figure 36 - Model Fit at $120^{\circ}C$ and $0.001s^{-1}$ .....	99

Figure 37 - Model Fit at 25°C and 935s <sup>-1</sup> .....	100
Figure 38 - Model Fit at 50°C and 935s <sup>-1</sup> .....	100
Figure 39 - Model Fit at 70°C and 935s <sup>-1</sup> .....	100
Figure 40 - Model Fit at 90°C and 935s <sup>-1</sup> .....	101
Figure 41 - Model Fit at 120°C and 935s <sup>-1</sup> .....	101
Figure 42 - Model Fit at 25°C and 0.01s <sup>-1</sup> .....	101
Figure 43 - Model Fit at 25°C and 0.1s <sup>-1</sup> .....	102
Figure 44 - Model Fit at 25°C and 2209s <sup>-1</sup> .....	102
Figure 45 - Model Fit at 25°C and 2900s <sup>-1</sup> .....	102
Figure 46 - Model Fit at 25°C and 5450s <sup>-1</sup> .....	103

# LIST OF ABBREVIATIONS

ANOVA.....	Analysis of Variance
CDFW.....	Continuous Drive Friction Welding
DOE.....	Design of Experiment
FE.....	Finite Element
FEM.....	Finite Element Model
FSW.....	Friction Stir Welding
FW.....	Friction Welding
HDPE.....	High Density Polyethylene
IFW.....	Inertia Friction Welding
LFW.....	Linear Friction Welding
OFW.....	Orbital Friction Welding
RFW.....	Rotary Friction Welding
S/N.....	Signal to Noise Ratio

# CHAPTER ONE

## INTRODUCTION AND BACKGROUND

High Density Polyethylene (HDPE) pipe systems are a cost-effective solution to a wide range of pipe problems in industrial, marine, mining applications and many others. They can transfer chemicals, hazardous waste, compressed gases, water and slurries. PE pipe has the lowest repair frequency per mile per year, has a high strength, toughness and durability. HDPE pipes can save time and money because they are lightweight and flexible, leak free, and corrosion and abrasion resistant (Plastics Pipe Institute, 2019).

Polyethylene is the most commonly used polymer globally (Zhu et al., 2022), and the importance of quality, cost, and speed in welding operations increases with the increased use of the material. The most common method for joining HDPE pipes is butt fusion welding, which is energy-intensive due to the need for high temperatures and an external heat source. Rotary friction welding (RFW) is an energy-efficient alternative that converts mechanical energy into heat and concentrates it where needed (Hamade et al., 2019; Uday et al., 2010). This process involves one part rotating against a stationary part under compressive force, which generates interfacial heat and causes the materials to soften and flow outward, forming a weld. The RFW process produces high-quality welds with superior mechanical properties compared to the joined materials (Alves et al. 2012). The weld cycle can be divided into two stages: the friction stage, during which heat is produced, and the forging stage, in which the material is expelled, and a flash is formed (Uday et al., 2010). Friction welding is also a cost-effective and efficient technique for welding similar and dissimilar materials (Uday et al. 2010).



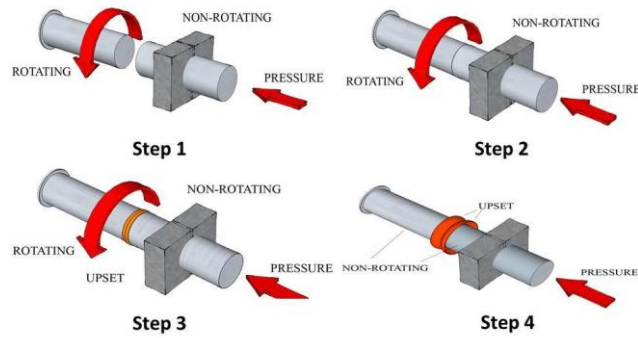


*Figure 1- Rotary friction welding process*

FW is a fast and complex process during which there is an interaction between the temperature evolution and mechanical deformation. Therefore, it significantly depends on the process parameters and is very difficult to investigate experimentally. This implies that an analysis through numerical modelling has significant value. Numerical modelling provides better insight into the process than only through the inspection of finished welds because it allows a better investigation of stress, strains and strain rate fields, residual stresses as well as their variations with process parameters. The thermal profile can be studied regardless of the severe plastic deformation taking place. The process can also be expressed in terms of material flow and surface self-cleaning capability. This better understanding of the process allows for process parameters optimization and limits the expense and time associated with experimental welding trials and mechanical testing.

One of the main challenges in rotary friction welding is selecting the appropriate welding parameters (W. Li et al., 2016) because they significantly affect heat generation and material flow, thus the weld zone microstructure, residual stresses and structural integrity. According to Li et al. (2016), if the parameters are chosen correctly, the weld will have well-bonded recrystallized grains. However, if the parameters are not appropriate, the weld may have defects such as micro-pores and residual oxides due to insufficient extrusion of material. Numerical modeling can be used to understand the

relationship between weld quality and weld parameters and optimize the parameters for a given application.

A lot of research has been done on numerical modelling of RFW for metals and the influence of input parameters on weld quality. However, experimental optimization of RFW of plastics is limited and numerical modelling of the process is extremely limited. In this study, the welding parameters will be optimized to produce high quality welds with minimum power consumption through numerical modelling and Design of Experiments (DOE). First, modelling of rotary friction welding will be performed to predict the temperature evolution, load, and torque requirements of HDPE pipes during the welding process. The model will replicate the work of Hamade et al. (2019), and will be done using the commercial finite element code DEFORM because it includes a special element for torsion. It will then be validated based on experimental data. The model will provide a better understanding of the thermal and mechanical behavior of HDPE during RFW. Then, a DOE procedure will be employed to optimize input parameters using the Taguchi method. A test matrix will be developed and used as input to the FE model. The S/N ratio will be calculated, and an analysis of variance (ANOVA) will be performed to determine the optimum parameters and predict performance. As a result, industry professionals can rely upon the resulting parameters to shift their welding operations towards leaner and energy efficient manufacturing. A better understanding of the RFW of HDPE plastic pipes is also obtained to yield high-quality welds with minimum energy consumption and reduced cost.

## 1.1 Welding of Plastics

Polymers have a very wide range of applications, larger than any other material. Joining is generally the final step in manufacturing cycles and is critical for polymeric parts. As the requirements for parts rise, so do those for joining. The methods for joining plastics can be divided into three categories: mechanical fastening which uses additional components/fasteners such as bolts, screws and rivets, adhesive and solvent bonding which consists of applying adhesives between the components to be joined, and welding. The use and types of plastics have increased, and so did the importance of quality, cost, flexibility, and speed in welding processes. Plastics can be classified into two categories: Thermosets do not soften or melt with heat, once hardened. The conversion solid liquid is irreversible. Thus, their joining depends on mechanical fastening or adhesion. Examples include Epoxy resin and phenol resin.

Thermoplastics soften and melt with heat, thus can be welded. The conversion solid liquid is reversible. The welding technique should be carefully selected based on the physical properties of the plastic material. Examples include polyethylene and nylon. Thermoplastics can be amorphous or semi-crystalline. Amorphous thermoplastics have random molecular structure as they cool. They solidify below their glass transition temperature ( $T_g$ ). The glass transition temperature is that at which an amorphous polymer transforms from a rigid glassy state to a rubbery state upon heating. Its molecular mobility increases, which leads to pronounced changes in its thermal properties (Alfredo Campo, 2008). Semi-crystalline thermoplastics solidify with a specific order in the molecular structure. Those regularly ordered molecules harden below the melting temperature  $T_m$ , while those that remain not ordered solidify at the glass transition temperature  $T_g$ . HDPE is a semi-crystalline plastic, meaning that the material shows organized and tightly packed molecular chains, thus has a defined melting point. The degree of crystallinity

changes among different materials and even among the same material. Low density polyethylene (LDPE) has a lower degree of crystallinity than high density polyethylene (HDPE). The latter is more crystalline: less branched, less flexible and denser (Sercer & Raos, n.d.).

## **1.2 HDPE Pipe Systems**

HDPE pipe systems are cost-effective and can be used for different services such as chemicals, hazardous waste, compressed gases, water and slurries. HDPE pipes can save time and money because of the following features (Plastics Pipe Institute, 2019):

- Corrosion, abrasion, and chemical resistance: PE pipes last longer than many more expensive materials because they resist abrasive slurries, are nearly inert and have higher resistance to acids, bases and salts than most piping materials. They do not require costly maintenance or cathodic protection. They are not affected by bacteria or fungi in soils and resist many organic materials such as solvents and fuels.
- Excellent flow characteristics: PE piping maintains optimum flow rates because it has a high resistance to scale and build-up, and has lower drag and tendency to turbulence. Since it is smoother than steel, cast and ductile iron, and concrete, a smaller cross section can hold an identical volumetric flow rate at the same pressure.
- Lightweight and flexible: the density of PE is about 1/8 that of steel, so it is lightweight and doesn't need heavy equipment for handling and installation. PE piping allows bending and minimizes the need for fittings, has high strain allowance and resists the effects of freezing, works well in earthquake vulnerable areas, and can be installed over uneven ground continuously. Allowable bending

radius is 20-25 times the outer pipe diameter. The light weight and longer lengths result in reductions in equipment and labor costs.

- Ductility and Toughness: PE piping resists pressure surges like water hammers, vibrations, and external loads. It bends and can be handled efficiently in cold weather.
- Leak free: HDPE joints can be as strong as the base material which prevents any leakage.

### **1.3 Friction Welding**

It is a welding process that can produce high quality welds between two parts with similar and dissimilar materials, such as drilling pipes and hydraulic cylinder rods. The American Welding Society defines friction welding as “a process that produces a weld under compressive force contact of workpieces rotating or moving relative to one another to produce heat and plastically displace material from the faying surfaces” (Jenney & O’Brien, 1991). The parts rub against each other under a compressive force, to generate interfacial heat. As a result, the interfaces reach intimate contact with time, then intermolecular diffusion and chain entanglement take place (Grewell & Benatar, 2007). The material softens and flows outward to bring about a weld. After the required heat has been generated, the workpieces stop rotating or moving relative to one another, but the pressure is either maintained or increased to boost the materials’ coalescence. In brief, the friction welding machine converts mechanical energy into heat at the joint of two workpieces moving relative to one another (Maalekian, 2007).

The weld cycle can be split into two main stages: the friction stage and the forging stage. The heat is produced throughout the first stage. The higher the energy input, the

wider the softened zone. At a certain level of softening, the material is expelled out to form a flash (Grant et al., 2009; Uday et al., 2010).

In the history of FW, the concept of melting at the weld interface has been controversial. According to Uday et al. (2010), even though FW is a solid-state welding process, sometimes a molten film forms at the interface. Nevertheless, the final weld should not show proof of a molten state due to the substantial hot working in the process final stage. In other words, even though the temperatures are very high, the material stays in the solid state, so no melting takes place (The Welding Institute, n.d.-c). However, Yang (2010) stated that the friction coefficient gets as low as 0.02 and the stress gets below 10MPa, which is difficult to explain for a solid material. Also, Hamade et al. (2019) and MADEN & ÇETİNKAYA (2021) have reached peak temperatures higher than the melting points of HDPE and polypropylene (PP) respectively. Therefore, RFW welding can experience melting depending on the material type and input parameters.

Plastics are poor conductors of heat, so the heat generated by friction at the interface is slowly transferred to the interior. If the heat accumulation is fast, the interfaces melt, and a weld forms. This is what happens in RFW of thermoplastics, where one workpiece is held stationary and contacts the other, which is rotating very rapidly (Uday et al., 2010). According to The Welding Institute (n.d.-a), welding and cooling pressures for friction welding of plastics are typically between 0.5 and 2MPa. Higher weld pressures can decrease the weld strength by squeezing out most of the molten thermoplastic materials. This leads to the formation of a “cold weld”.

### **1.3.1 Principal Friction Welding Processes**

Mechanical friction welding is split into multiple categories which all depend on the relative motion between two parts to generate frictional heat. The arrangement of relative motion, frequency and amplitude are the differences among these processes (Bindal et al., 2021).

#### 1.3.1.1 Rotary Friction Welding

Also called spin welding. It has been commercially used since the 1940s (Uday et al., 2010). RFW is the oldest and most popular friction welding method: one workpiece rotates about its axis while the other is kept stationary. Then, pressure is applied to bring them together. Typical rotation speeds range from 1200 to 3500 RPM (The Welding Institute, n.d.-b). Here, the rotational energy is transformed into frictional heat. The process produces excellent quality welds which have superior mechanical properties than the joined metals (Alves et al., 2012). RFW cannot be used for non-circular cross sections, and the heat generation is not uniformly distributed across the weld interface, resulting in a non-uniform HAZ thickness. Both limitations can be prevented with linear friction welding (LFW) and orbital friction welding (OFW), which have more uniform heat distribution (figure 2). OFW shows the most uniform heat distribution because the components move in one direction across the interface with a uniform relative velocity (Uday et al., 2010).

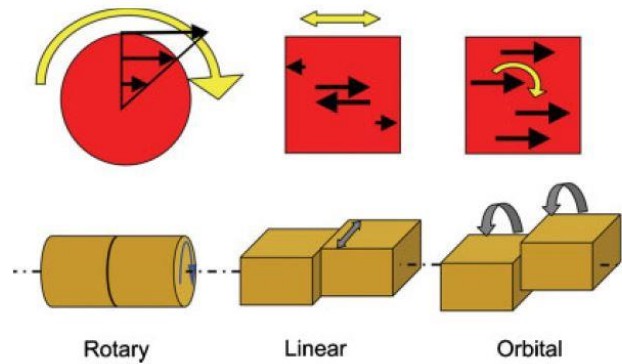


*Figure 2 - Distribution of heat generation in friction welding*

### 1.3.1.2 Linear Friction Welding

Linear friction welding has been employed since the 1980s. Here, the parts move in a reciprocating manner relative to each other. As a result, a small linear displacement is made in the joint interface. This process expands the applications of rotary friction welding to non-axisymmetric workpieces. Both processes vary as to heat input and stress field at the interface. For example, LFW generates a more uniform heat distribution than RFW (Maalekian, 2007).

### 1.3.1.3 Orbital Friction Welding

Orbital friction welding started in the 1970s. Contrary to rotary friction welding, this method applies to non-circular parts. It is a combination of linear and rotary friction: the center of one part moves around a circle relative to the other part; both parts rotate around their longitudinal axes with a constant angular velocity. The two axes are parallel except for a small offset. Neither part rotates about its central axis. The motion delivers uniform tangential speed across the whole interface. The components are aligned rapidly after motion stops. This process yields high quality joints because the relative velocity at the frictional interface is constant. OFW provides more uniform and efficient thermal energy than both RFW and LFW (Maalekian, 2007).



#### 1.3.1.4 Friction Stir Welding

Friction stir welding (FSW) was first patented in 1991 (Uday et al., 2010). It is mainly used on aluminum and large parts which are hard to heat treat post weld. Here, a non-consumable tool rotates and moves across the interface to form a plasticized region around the central pin. The material softens because of the frictional heat, then gets mixed by the rotating tool producing a bond (The Welding Institute, n.d.-c).

#### 1.3.2 Rotary Friction Welding VS. Butt Fusion Welding

According to Hamade et al. (2019), conventional butt fusion welding of HDPE pipes is energy consuming because it uses an external source of heat. However, RFW is energy efficient because it converts mechanical (rotary) motion into thermal energy. Hamade et al. concluded that RFW requires shorter cycle times than butt fusion welding and less power consumption. It is also 10 times cheaper than butt fusion welding. Therefore, a shift from conventional welding operations to RFW can achieve cost savings and reduce environmental impact. One of the remarkable advantages of FW is the reduction in costs. Parts can be pre-machined with lower costs because the HAZ is not thick.

According to Cai et al. (2019), joints have considerably less solidification defects than fusion bonded joints. Since mechanical energy is directly transformed into thermal energy at the weld interface, less energy is lost, compared to fusion welding. The process has a short cycle time, vs other solid-state processes, such as diffusion bonding welding. Diffusion bonding is a solid-state welding process whose principle is the diffusion of atoms across the joint boundary at high temperatures (The Welding Institute, n.d.-a). According to Grewell & Benatar (2007), the cycle time is typically less than 10 seconds.

Takasu (2003) states that the weld time is short, the weld interface is always clean, and it is easy to make sure that the joint is reliable because the interface, unlike the case of heat fusion, does not contact the atmosphere throughout the process. It also contributes to large cost reduction.

Maalekian (2007) adds that many materials cannot be joined with conventional welding techniques but can be joined with friction welding. A few examples include medium and high carbon steels, and alloys. FW can also weld dissimilar materials in a full-strength joint made of a completely new material composed of the two original workpieces.

As a summary, FW has the following features compared to conventional welding techniques: less energy consumption, less cost, shorter cycle time, less environmental impact, clean interface and less solidification defects.

### **1.3.3 Advantages and Disadvantages**

In addition to the benefits of RFW over butt fusion welding, friction welding process is very energy efficient and fast (Maalekian, 2007). The high temperature gradient yields a narrow HAZ thus minimum welding distortion. The mechanical deformation and temperature dominate the weld formation. The plastically deformed material is present around the weld, called flash, and there's no fusion zone. This plasticized material moves out of the interface, leaving a high integrity weld because all surface oxides and contaminants have been eliminated. Friction welding results in superior strengths without affecting product integrity (Donohue, 2001). Moreover, it is environmentally friendly and non-hazardous: little smoke, no fume, radiation, or electric hazard. There are no consumables such as shielding gases or filler metals. Plus, it can be fully automated, and

no welder certificate is necessary. The process parameters are also pre-established, which limits operator error. According to Cai et al. (2019), FW yields better tensile properties than the parent material because the high temperature and severe deformation result in recrystallized microstructures.

Nevertheless, FW has some drawbacks. The zone of non-uniform thickness. It is challenging to weld thin wall structures with LFW and RFW. Added to that, RFW can only be applied on circular cross-sections. Flash elimination procedures have to be taken into account and clamping tools must be strong enough to resist the applied frictional pressure and torque.

#### **1.3.4 Stages of RFW**

Frictional welding is distinguished by 4 phases (Grewell & Benatar, 2007). In the first phase, the parts are clamped, and rotation starts. Then, they are brought together through an axial pressure. The temperature increases rapidly, and abrasion will remove the surface roughness. With higher speed and axial pressure, this phase becomes shorter (Tappe & Potente, 1989). The surfaces then are in full contact, and heating is generated by solid-solid interfacial friction, but no material flows at first. Some thermoplastics, such as fluoro polymers, have a low friction coefficient, which makes them not weldable with this process. Others, however, such as Polyethylene (PE), need elevated clamping forces to produce high frictional forces.

In the second phase, which is also called the transition or unsteady state friction phase, a thin plasticized layer has been formed and shear deformation replaces solid frictional heating by viscous heating. As a result, the temperature increases quickly, and the thickness of the plasticized layer rises and material displacement starts.

The third phase is also called the steady-state phase. Here, material flows at a constant rate: the rate of heat generation equals that of heat loss, and there is no need for further softening because it will lead to excessive weld flash instead of a higher weld strength. Therefore, this is the ideal phase to stop motion. Here, the displacement rises linearly with time, and the softened layer has a constant thickness.

The final phase is the cooling phase where the rotary motion is stopped and material cools under the axial pressure which remains either constant or increases. Actual bonding happens throughout this forging phase which is managed by braking time, forging time and axial pressure (Maalekian, 2007).

Phases I, II and IV are essential but have no benefit, in terms of weld strength, in prolonging Phase III. Typically Phases I and II take between 0.5 and 8 seconds to complete, and this depends on the surface area being joined. Typical cooling times in Phase IV are between 4 and 10 seconds (The Welding Institute, n.d.-b).

These four friction phases are shown in terms of material displacement versus time in figure 3.

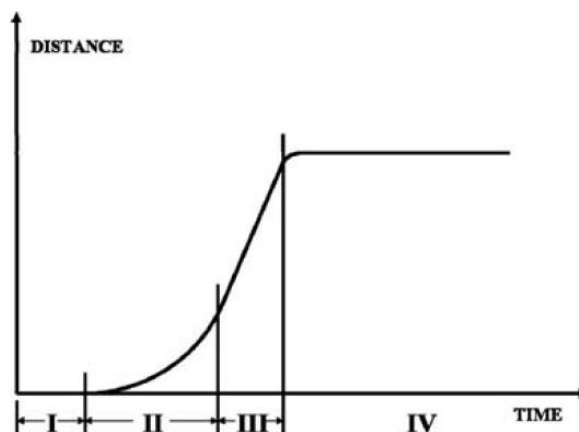


*Figure 3 - Typical meltdown (displacement) as a function of time in friction welding*

### 1.3.5 Energy Variants

There are two major process variants in rotary friction welding (Maalekian, 2007). The first variant is the direct/continuous drive friction welding (CDFW) which involves a constant energy from a source for any chosen time span. In this process, a workpiece is held stationary while the other rotates at a constant velocity. Axial force is applied, and after a pre-determined time or axial shortening, the drive is detached, and rotation stopped. Axial pressure is maintained or increased until the material cools. The main welding parameters are rotational speed, axial force and welding time. They determine the amount of energy input and rate of heat generation.

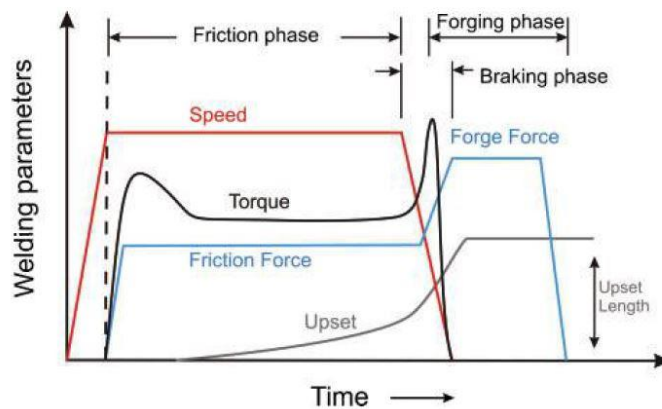


Figure 4 - Variation of welding parameters with time for CDFW

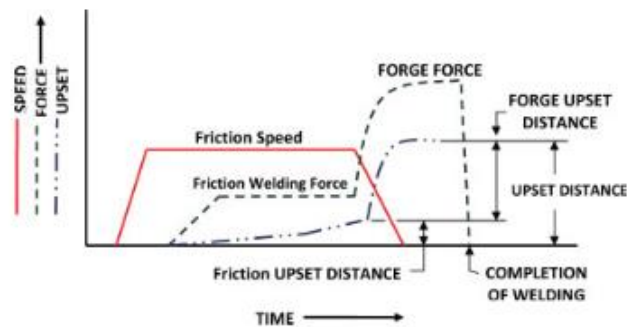


Figure 5 - Characteristics of CDFW parameters

The variations of the welding parameters with time and their characteristics are shown in figures 4 and 5 respectively. First, the torque increases fast and reaches a peak, before gradually reducing to an equilibrium value. This is due to the mesh of asperities and material softening on the joining interface. In the 2<sup>nd</sup> phase, the torque remains constant, meaning that there is a balance between strain rate hardening and temperature softening. In the 3<sup>rd</sup> phase, forging begins at the time of braking. Axial force rises and the torque makes another peak, then goes to zero. This peak depends on the axial pressure and deceleration.

The second variant is the inertia drive friction welding (IFW) which uses the kinetic energy stored in a rotating flywheel. In this process, a workpiece is held stationary while the other is engaged to a flywheel. The flywheel spins at a certain speed, to store a pre-established amount of energy. After the drive to the flywheel is detached, an axial force is exerted. The kinetic energy stored in the flywheel will generate heat at the interface, and the rotational speed will decrease gradually until rotation ceases. Axial pressure is maintained or increased until the material cools. The main welding parameters are rotational speed, axial force and flywheel mass. The variations of welding parameters are the same as direct drive, except for the rotational speed, which decreases with time. Here, the rotation and forging times are not pre-selected, rather governed by the three main variables mentioned above. Figures 6 and 7 show the variation of process parameters and their characteristics during IFW.

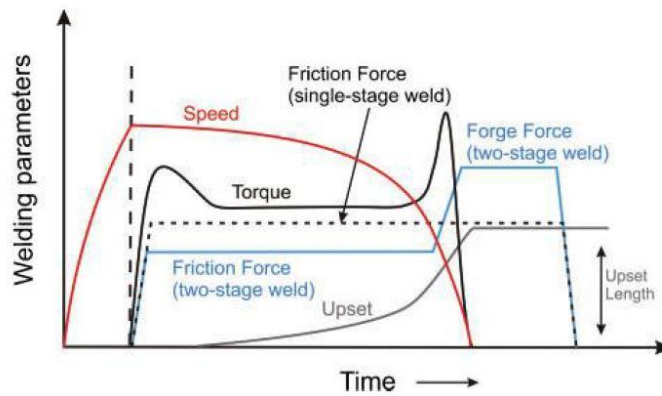


Figure 6 - Variation of welding parameters with time for IFW

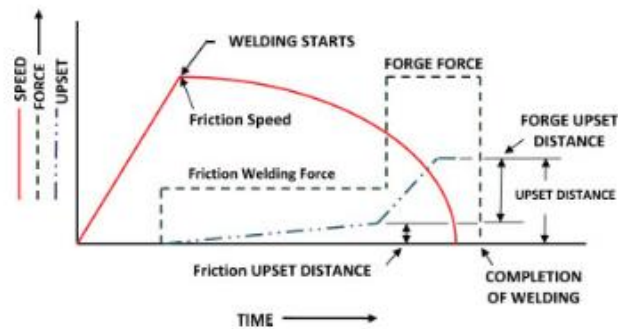


Figure 7 - Characteristics of IFW parameters

Both processes result in very good joints. There are, however, non-universal differences, that depend on the application: material composition, geometry and size considerations. Other parameters affecting FW include axial shortening rate and coefficient of friction. For example, direct drive process usually employs low RPM and axial pressure. It also provides more flexibility since welding parameters are pre-set. However, energy is delivered faster in inertia welding thus the temperature gradients are more pronounced and the HAZ is narrower.

### 1.3.6 Friction Welding Parameters

There are three important parameters in FW process: speed, pressure and time. They should be investigated individually or in combinations to figure out their effects on the

joint produced. (Uday et al., 2010). In friction welding, the parts being joined retain their original properties and the HAZ is very small compared to fusion welding techniques where most of the decline in strengths and ductility starts.

### Speed

The rotational speeds are associated with the material and the diameter of the weld at the interface. Increasing rotational speed produces more heat, thus more softening of the material. Different intervals of rotational speeds affect the quality of the joint differently, depending on the mechanical and physical properties of the materials included. Therefore, rotational speeds must be chosen appropriately to reduce any harmful effects and produce good quality joints.

### Pressure

The temperature gradient in the weld, the power and the burn-off are governed by the pressure (W. Li et al., 2016). The pressure is determined by the parts and the joint geometry. It should be high enough to retain the faying surfaces in close contact and prevent oxidation (Mousavi & Kelishami, 2008). For a given speed, low pressure restricts heating and leads to very little burn-off. On the opposite, high pressure results in local heating, high temperature and quick burn-off. For mild steel, the burn-off rate is proportionate to pressure. For a given pressure, low speed gives greater axial shortening than high speed during the heating phase. The application of an increased forging force at the end of the heating period boosts the joint quality in multiple materials.



## Heating time

Too much heating causes lower productivity and material waste. Too little time may lead to uneven heating, trapped oxides, and non-welded areas at the interface. Heating time can be managed by using a suitable timing device where rotation stops after a preset period, or by ceasing rotation after a pre-established axial shortening to consume a sufficient length and secure enough heating before upsetting. Changes in surface condition can be handled without losing quality. Heating time decreases with increases in pressure (Uday et al., 2010).

### **1.3.7 Heat Generation in Friction Welding**

FW process includes both heating and plastic deformation of the parent material under extreme thermal and strain rate conditions. At first, deformation occurs at low strain rates and high temperatures. However, because of the axial displacement, the material becomes fully plasticized with strain rates reaching  $10^3 \text{ s}^{-1}$ . It is difficult to get a correct description of the energy input at the mating interface in heat transfer modelling during FW because the friction coefficient  $\mu$  is always varying during the welding cycle from  $\mu > 1$  initially or at the dry sliding to zero when the temperature required for the melting of irregularities is attained (Uday et al., 2010).

Although each welding parameter individually has an effect on joint performance, the relationship among them is what forms a joint with good mechanical properties (G. Wang et al., 2018). The relationship between pressure, rotary speed and time in the heating phase, leads to an increase in frictional temperature. This temperature rise, along with a constant pressure, results in plastic deformation and flash formation. Then, when sufficient heat is generated and forging pressure is applied, the weld is successfully achieved. If the temperature had not been enough for diffusion and forging, a poor-quality

joint with poor mechanical properties would have resulted, and the layers of oxides and impurities would not have been completely eliminated. The welding parameters also dictate the amount of energy input and rate of heat generation which fluctuates throughout the phases of FW (Maalekian, 2007).

### **1.3.8 Tensile Strength of Welded Specimen**

Tensile tests are done on weld joints to evaluate strength and plasticity and inspect the effect of welding defects on the joint performance. According to The Welding Institute (n.d.-a), optimum welding parameters in RFW lead to joints with superior or similar strength as the parent material. Udayakumar et al. (2013) investigated the mechanical and metallurgical properties of rotary friction welded super duplex stainless steel bars and concluded that the weld tensile strength exceeds that of the base metal because of the very fine grains in the weld zone, and fractures take place away from the weld zone. Welded specimens also exhibited better toughness than the base metal. Hasegawa et al. (1998) found that HDPE pipes that were welded at 34 and 50 rad/sec fractured in the base material and that sound welds had tensile strengths that are comparable to the base material. The strain at failure, however, was somewhat less than that of the base material.

# **CHAPTER TWO**

## **LITERATURE REVIEW**

Finite element modelling is the most adopted technique to investigate friction welding and processing of metals (Yang, 2010) because it allows for a thorough analysis of the stress state, considers both thermal and mechanical behaviors at each time step, and is capable of illustrating the flash formation. Even though FE modelling is very time consuming, it has been used by multiple researchers to study friction welding. Most studies concentrate on the evaluation of temperature, stress and strain fields because they are essential parameters that have direct effect on the quality of joints. Almost all research involving numerical modelling of FW is concerned with metals, and very few tackle plastics.

### **2.1 Numerical Modelling of Metals**

Cheng (1962) was a pioneer in numerical modelling of FW. He performed a simulation of FW of AISI 4140 steel through a 1D finite difference method. The study assumes that melting exists at the weld interface and considers temperature dependent thermal properties and axial shortening effects. There was a good agreement among the model predictions, experimental results, and analytical model data.

Wang & Nagappan (1970) performed a purely thermal 2D finite difference model for the IFW of AISI 1020 steel bars. No thermomechanical coupling was employed. The authors employed a heat flux at the weld interface in terms of rotational speed and position from the center of the interface and emphasized the high thermal gradients of the process. Temperature evolution at the end of the welding cycle compared well with the experimental data with an 8% error. Similar to other studies, the authors stated that the

weld time has a crucial effect on the temperature distribution. It was also reported that inertia and continuous drive friction welding differ in terms of temperature evolution: in inertia welding, the temperature peaks in 0.06 sec whereas in continuous drive FW, it peaks in about 20 sec. No explanation was provided for this difference. A very similar work was done by Wang and Lin (1977) who pointed out that the interface temperature increases sharply then reaches a steady state after 0.2 seconds in the IFW of low carbon steel bars.

Sahin et al. (1988) developed a 2D finite difference model of friction welding of copper and steel bars. The authors assumed a constant coefficient of friction and thermal properties. They concluded that the temperature reaches its highest value neither at the circumference nor at the center of the weld interface.

From an analytical viewpoint, Dave et al. (2001) built a thermal model that predicts the transient temperature profile during dissimilar IFW. The authors used experimental data to estimate the flywheel energy and resulting thermal input but did not take material deformation into account. The aim was to help parametric optimization for welding dissimilar materials. The model implements many assumptions such as average material properties and temperature across the weld interface. However, there was an agreement between predicted results and thermocouple readings.

Subsequent models of FW were developed using a fully coupled thermo-mechanical model because it can replicate the actual material behavior by taking into account the interactions between the temperature gradient and mechanical deformation. There are generally two approaches that are adopted in the literature to thermo-mechanically model the weld interface in FW. The first approach is the use of experimental data. This data is transformed into a heat flux or friction coefficient that is imposed at the weld interface. As a result, the thermal fields, material flow and residual stress of existing welds can be

represented numerically. The second approach is predictive, so there's no need for actual welds. A friction law is adopted to describe the weld interface conditions. The friction law is usually in terms of temperature, pressure, rotational speed and material properties, and it is coded into a subroutine to evaluate the coefficient of friction at each time step (C. Bennett, 2015; C. J. Bennett et al., 2007)

Sluzalec (1990) was the first to adopt a FE approach to investigate FW. The author built a 2D axisymmetric thermomechanical model to predict the temperature evolution, flash formation and stress and strain fields of mild steel. Temperature dependent material properties and coefficient of friction were employed. The predicted temperatures compared well with the experimental data.

Moal & Massoni (1995) used the FE method to simulate a fully coupled axisymmetric thermomechanical model of IFW of a nickel-based superalloy. The model accounted for torsion by including a three-component velocity vector. This resulted in a 2.5D model that successfully predicted the flywheel's slowdown. The authors used an incompressible material behavior, temperature dependent material properties, and speed and pressure dependent friction coefficient. The code "INWELD" incorporated adaptive remeshing to surpass the substantial element distortion. The model results such as rotational speeds compared well with the experiments, but the upset was overpredicted by 20% due to inaccurate model parameters.

Fu and Duan (1998) conducted a coupled thermal and deformation analysis to estimate the temperature, stress, strain rate fields and final weld shape of IFW of GH4169 superalloy. The thermal predictions and weld shapes were in good agreement with experimental data.

A purely thermal FE model was undertaken by Balasubramanian et al. (1999) to evaluate temperature distribution during the IFW of IN718. The authors proposed an

energy balance method to overcome the issue of determining the friction coefficient by assuming that 100% of the flywheel's kinetic energy is converted into frictional heat. This was an input to the FE model as a boundary condition. The predicted thermal profiles agreed well with experimental measurements. The study, however, did not include mechanical analysis.

Lee et al. (2001) extended the DEFORM-2D code to incorporate the effects of torsion, so a special 2.5D axisymmetric component was created. It has radial ( $r$ ), axial ( $z$ ), and circumferential ( $\theta$ ) velocity components but no velocity gradients in the circumferential direction. These velocity components are used to find the heating rate due to friction, by either a constant shear or Coulomb friction model. The model was validated both experimentally and analytically, and was of great use for DEFORM users wishing to model friction welding processes.

Similarly, D'Alvise et al. (2002) implemented a thermomechanical model of IFW of dissimilar materials in the FORGE2 commercial code. They expanded the study of Moal & Massoni to consider the welding of dissimilar materials. The model took inertia, forces and friction into account. The interface contact was presented through a friction law that is a function of temperature, pressure, and rotary speed. The model was capable of estimating temperature, strain and residual stress. The model was validated by comparing the predicted outer pipe radius (including the flash) and the flash length to experimental values. The resulting errors were 1.1 and 3.8% respectively.

Fu et al. (2003) established a 2D coupled thermo-mechanical model of IFW of 36CrNiMo4 steel tubes. A constant friction coefficient was employed with an elastoplastic material's constitutive model. DEFORM 2D software package was used to investigate the stress, strains, temperature and weld geometry. There was a close match between the

predicted thermal profiles and measured ones. Nonetheless, there was no validation of predicted stress and strain fields.

Liwen et al. (2004) performed a 2D thermo-mechanical model of IFW of GH4169 superalloy. Material properties varied with temperature and the simulation results included the temperature, stress and strain fields. There was a close match with thermocouple data, but no burn off validation was done.

L. Wang et al. (2005) built a coupled thermo-mechanical model of IFW of a nickel-based superalloy called RR1000. The model was performed on DEFORM software package, where instead of assuming a friction coefficient, an energy input method was employed. Experimental rotational speed curves were used to calculate the rate of kinetic energy loss and ultimately the energy input rate, which was loaded into DEFORM as a thermal boundary condition at the interface. Recorded upset data was also imposed as a boundary condition in the model. There was good agreement between the thermal profiles and experimental data, but residual stress predictions were overestimated by about 35%. Nevertheless, no torsion effects were taken into account, which affect the accuracy of the results. Since the model relies on experimental data, it cannot be used as a predictive tool.

An uncommon 3D model of CDFW of nickel-based superalloy was performed by Zhang et al. (2006) using DEFORM software. Both thermal effects and material deformation were considered and a rigid viscoplastic material model was used. Torsion was also included for the description of heat generation. Friction was described by a Coulomb friction law at a low temperature range, and, shear friction at a high temperature range. However, the equation of the friction coefficient was in terms of pressure, temperature, and linear velocity but the constants were not indicated. The authors state that there's a transition between low and high temperatures, but do not identify its ranges or how these are determined. The model was validated by comparing the temperature

evolution and flash geometry with model predictions. Compared to the ordinary 2D model, the 3D model does not appear to have any additional value.

C. J. Bennett et al. (2007) have modelled the IFW process of similar and dissimilar shafts made out of a nickel-based superalloy, Inconel 718 and a high strength steel, AerMet 100 on DEFORM-2D software. The study includes both a representative and predictive models. The representative model uses a pre-defined coefficient of friction calculated from experimental data and recreates the actual weld. The predictive model, however, implements a friction law that is founded on the work of D'Alvise et al. and that evaluates the coefficient of friction at each interfacial node and at each time step. For the similar materials weld, a good match exists between the model predictions and experimental data in terms of rotational speed but the upset is underestimated by 8%. As for the thermal predictions, they are close to actual measurements at the interface, overpredicted at 1 and 3mm away from the interface and underpredicted at 9mm away from the interface. This unexpected result is attributed to thermocouple locating inaccuracy.

Maalekian et al. (2008) investigated four different heat generation models to obtain the temperature profile during orbital friction welding of steel specimen using DEFORM software. The models were the constant coefficient of friction model, the slip-stick model, the power model and the inverse model. The last two models relied on experimental data and the inverse model turned out to be the best indicator of heat generation rate and can be used to evaluate the coefficient of friction. The authors also inferred that the heat generated because of friction was much more significant than that generated by material deformation. The predicted width of the HAZ compared well to the experimental one because the inverse model was capable of accurately determining the thermal input.



Akbari Mousavi & Kelishami (2008) performed a 3D simulation of CDFW on Abaqus to estimate the temperature profiles, final weld geometry, strain fields and Von-Mises stresses. Results showed that the Von-Mises stress and plastic strain fields are proportional to the axial pressure and that joints were broken at the base material during tensile tests.

El-Hadek (2009) analyzed the IFW of 36CrNiMo4 through a 3D FEM on ANSYS software. An elasto-plastic material model was adopted to examine flash formation and residual stresses. Experimental acceleration curves were employed to estimate the coefficient of friction. The authors deduced that the deformation on the outer and inner surfaces are not identical, that is, upper lip deformation is larger than lower lip deformations.

Grant et al. (2009) replicated the model of L. Wang et al. (2005) but used an enhanced material database, which led to a closer agreement between thermal and residual stress predictions and experimental measurements. The authors concluded that peak temperature and strain rate are proportional to the applied pressure whereas the width of the heat affected zone (HAZ) is inversely proportional to the applied pressure.

Mohammed et al. (2009) built a coupled thermo-mechanical axisymmetric model of IFW of a dissimilar high strength steel and a nickel-based superalloy on DEFORM software package. The paper aims at evaluating the friction conditions which control the weld formation and are determined by weld parameters, mainly rotational speed and axial pressure. The authors presented a representative model that removes the arbitrary choice of the efficiency of mechanical energy necessary for the weld by incorporating it in the friction coefficient calculation. They also proposed a predictive model that doesn't require any actual weld data to find the friction coefficient using a sub-layer flow theory. During the initial heating stage, the authors showed that frictional shear stress depends on the

interaction of surface asperities and is affected by the axial pressure and flow stress of the material.

Mohammed et al. (2010) performed a simulation of IFW of SCMV to AerMet-100 with the aim of investigating the importance of heat transfer modes during the process. Those are conduction, convection, radiation and heat transfer at the workpiece die contact interface. The authors concluded that conduction dominates the other modes during the welding stage. However, the heat transfer between specimen and die plays the most significant role during the cooling stage. A general approach was developed to optimize heat transfer characterization and was validated by comparing the numerical and experimental upsets of six different models.

Yang (2010) investigated IFW of INC718 using a FEM model and three analytical models. All developed models were capable of predicting the upset accurately. The author deduced the presence of a high compressive stress band near the mating surfaces, and it's the reason behind the softening of the material. He also showed that the upset is increased by the shear frictional stress, and by increasing the load and temperature. As for the effect of adiabatic heating from plastic deformation, the author states that it appears to have a small effect on heat generation, when compared with friction heating produced by shear stress.

Madhavan et al. (2011) aimed at determining the optimum parameters for CDFW of Ferrium S53 using a 2D axi-symmetric thermo-mechanical model coupled to an optimization code. A viscoplastic material behavior and Coulomb friction laws were applied. The experimental force, angular speed and axial shortening evolutions, as well as hardness profiles and friction times compared well with the model's predictions. were extracted from the model and compared for the experiment data. Upset level diverged

from experimental values by about 0.5mm, which was regarded as negligible. The numerical optimization results were also in a close match with experimental ones.

Khan (2011) investigated the friction welding of dissimilar materials: Al 6061 to SS 304 and Al 5052 to SS 304. A 2D thermo-mechanical model was developed using ANSYS and ABAQUS software. The model employed temperature dependent material properties and predicted temperature profiles, effective stress and material deformation. The author examined the effect of temperature and axial shortening on weld strength. He also designed a joint geometry that enhances the process by initiating welding in the center of the weld interface and ending it at the periphery. The FEM discrepancies were attributed to the model's numerical assumptions.

Li & Wang (2011) created a 2D FE model of DCFW of mild steel and considered the effects of pressure and rotating velocity on burn off and interface temperature. A close match among final burn off, width of HAZ and flash shape and experimental results was obtained.

The thermal expansion on INC718 during IFW through a fully coupled elasto-plastic model has been assessed by C. J. Bennett et al. (2011). The authors investigated the effects of axial pressure and initial rotational velocity on the minimum contact area, the time taken to recover 90% of the initial contact area, and the latter's evolution. Results showed that at first, the generated heat causes local thermal expansion and a non-uniform pressure distribution, which leads to a reduction in the contact area. However, after sufficient heat input, the axial force results in plastic flow which increases the contact area.

Other studies used numerical models to optimize the process parameters of friction stir processing of metals (Ammouri et al., 2012, 2013). The optimized process parameters

were used to automate friction processing in a sustainable and efficient way (Ammouri & Hamade, 2015).

Seli et al. (2012) investigated the mechanical properties of rotary friction welded alumina-mild joints. The coupled thermo-mechanical model successfully predicted the stress, strain and temperature fields. The maximum values were found within the HAZ and around the circumference of the weld interface because this region has the highest temperatures.

C. J. Bennett et al. (2013) have also modelled IFW of dissimilar high strength steels, AerMet® 100 and SCM5, using DEFORM 2D software package. The authors used existing weld data such as angular velocities to evaluate the thermal input to a fully coupled thermal and mechanical FE model. An emphasis was made on the solid-state phase transformations and resulting residual stress data which were well reproduced in the model. The coefficient of friction was implemented through a user subroutine. The difference between the predicted axial shortening and experimental one was 2.5%. Thermal profiles, velocity deceleration rate, welding time and upset rate compared well with experimental data.

A 3D axisymmetric FEA of IFW of copper and Al6061 was studied by El-Hadek (2014). The non-linear mechanical and thermal properties of both materials were found, then input into the model using ANSYS software. The model predicted the thermal profiles, deformation and residual stresses. Then, the Taguchi method was implemented to find the optimum weld parameters. The model was validated by comparing the predicted and experimental flash shapes.

F. F. Wang et al. (2014) looked into the effects of pressure, initial rotational velocity and flywheel inertia on the temperature profile and upset through a 2D axisymmetric model of IFW of GH4169. A method for optimizing weld conditions was

later discussed. The authors concluded that the upset increases linearly with the initial rotational speed and logarithmically with friction pressure, and that the width of the HAZ is significantly affected by axial pressure when the forging stage is fast.

C. Bennett (2015) has also performed a fully coupled thermo-mechanical FEA of IFW for CrMoV steel. The approach here is not predictive as previous weld data is employed leading to enhanced model accuracy. Nevertheless, it allows accurate predictions of temperature variations and residual stresses. Upset values, rotational speeds, thermal history and residual stresses have all been validated. One of the author's conclusions was that a higher welding pressure yields a narrower HAZ.

Hynes & Velu (2017) performed a thermo-mechanical FE model of FW of ceramics and metal with an interlayer of aluminum. The model was capable of predicting thermal distributions and microstructural evolution of the dissimilar weld joint.

Schmicker et al. (2016) created an in-house MATLAB code to simulate CDFW using a Carreau fluid material law that can properly estimate plastic flow based on accessible properties such as the yield point and melting point. A constant Coulomb friction law has been implemented and the effects of welding parameters on flash have been studied. A good qualitative agreement was found between simulated and experimental flash shapes. The authors deduced that the weld time significantly affects the flash shape and that the upset is linearly dependent on the rotational velocity.

Dawood et al. (2017) presented a new method to estimate the temperature evolution during RFW. A constant friction coefficient or slip-stick method are usually used. Here, the model implements phase transitions curves on COMSOL Multiphysics®. The model was validated through experiments available in the literature. Results showed a maximum error of 11.84% between the predicted and experimental temperature profiles. The error at

peak temperature is 3.72%. Those discrepancies were attributed to the different environment temperature where the experiments have been done.

Tashkandi (2021) has also performed a coupled thermo-mechanical simulation of CDFW of AL6061 on COMSOL Multiphysics® after determining the material properties that change with phase transformations. Temperature evolution was investigated and compared to experimental results. Some differences exist and are attributed to the flash formation phenomenon. As for the peak temperature, it matched closely with studies in the literature.

## **2.2 Numerical Modelling of Plastics**

Polymer material processing through FW is a challenge (Kouta et al., 2020) because of the extensive deformations at the weld interface. There are very few studies that include FE modelling of friction welding of plastics.

Kouta et al. (2020) carried out a FE simulation of IFW of identical Polyamide 6 (PA6) and Polyvinyl Chloride (PVC) pipes. A coupled thermo-mechanical model with an elasto-plastic material behavior predicted the Von Mises residual stress and thermal evolution. The authors performed an optimization study of process parameters using the Taguchi method. The optimal conditions were then correlated with output parameters using an Artificial Neural Networks. The data from the resulting model and FE model were in good agreement: temperature and residual stresses were only 1.3% and almost 0% away from each other, respectively.

A FE model of RFW of Polypropylene (PP) was investigated by MADEN & ÇETİNKAYA (2021) with an aim to propose a new joint design to prevent the accumulation of semi melted material that clogs sensitive water purification filters. The model was built on ABAQUS software and predicted the thermal profile and stress fields. Results showed that the temperature increases to 150°C in 13.1 milliseconds and peak

temperature for optimal conditions is 166.2°C, so it's well above the melting point of PP. An axial shortening of 1.98mm was reached with a maximum stress of 4.9253MPa.

## **2.3 Experimental Studies on RFW of Plastics**

Crawford & Tam (1981) investigated the welding characteristics of four thermoplastics: Nylon 66 and acetal which are semi-crystalline, and polymethylmethacrylate (PMMA) and polyvinyl chloride (PVC) which are amorphous. The sample pipes had 12.75 mm outside diameter and 7.45 mm inside diameter with 65 mm lengths and flat ends. Results showed that the resisting torque and burn-off rate remained mainly constant during the friction stage, but increased as the axial pressure and the rubbing velocity increased. The rate of heat generation was greatest in nylon 66 followed by acetal, PMMA and PVC. PVC, however, had the greatest burn-off rate followed by nylon66, PMMA and acetal. This shows that a complex interaction of material properties affects the degree of burn-off because PVC heats up slower than the other materials and has a high melt viscosity. The relatively slow burn-off rate for the other materials can be explained by the fact that low viscosity films are rapidly formed and squeezed out of the interface. As a result, cooler surfaces produce more heat to form a new viscous film. PVC, on the other hand, undergoes uniform bead formation. The highest tensile strength that could be reached was about 50% of the strength of the parent materials, even if the weld beads are eliminated. PMMA, for instance, gave a weld factor of 0.87 with a combination of low axial pressures, high rotary speeds and a final forging pressure. The authors concluded that good quality welds are not easy to achieve because welding conditions are not optimized.

Stokes (1988) who performed an analytical modelling based on the data found by Crawford & Tam (1981), concluded that changing the weld velocity affects the steady-

state film thickness more than the weld pressure. Also, if weld pressure is kept constant, increasing the weld velocity dramatically reduces the steady state viscosity. Nevertheless, if weld velocity is kept constant, changing the weld pressure has insignificant effect on viscosity.

Hasegawa et al. (1998) researched the influence of welding parameters on CDFW of HDPE pipes. The authors concluded that the initial torque, axial shortening and flash dimensions increase significantly with friction pressure. Torque and pressure values are also much less than those of metals, and good quality welds have tensile strengths that are comparable to the base material. The same authors performed a more detailed study on the same topic by looking into the steady torque value and friction heating values obtained during the process (Hasegawa et al., 2002). Results revealed that the axial shortening of the rotating and fixed pipes are different depending on the weld parameters, which have a narrower range than those of Carbon steel.

According to Stokes (1989), the most important parameter that affects the joint's strength is the weld penetration or displacement. High quality welds can be made for displacements greater than a threshold value. This threshold is the displacement at which the steady state is achieved (beginning of phase 3).

Tappe & Potente (1989) investigated the effects of welding parameters on the temperature, melt rate (axial velocity), and torque of multiple semi-crystalline thermoplastics, including HDPE. The rotary speed ranged between 800 and 4800 rpm (1 and 6.3 m/s). Tensile tests were also performed to establish weld quality. A comparison of theoretical predictions and experimental data was done and revealed a good match. The authors deduced that an increase in rotary speed and axial pressure causes an increase in axial velocity and torque. In regards to weld quality, a higher weld quality was achieved with higher friction time, until phase 3 is reached, after which friction time had no effect



on increased strength. Braking with a sudden stop also gave a higher weld quality than continuous braking. The authors deduced that for HDPE welds, speed had the highest effect on weld quality: weld factors close to 1 were achieved at speeds exceeding 3 m/s. However, no optimization was performed.

Potente & Uebbing (1997) studied the vibration and spin welding processes of different types and grades of polyamides. Weld quality was assessed by tensile tests and microtomes. The authors suggest that each application requires a different set of optimum parameters depending on the geometry of the parts, the material and the process parameters. Also, drying the material decreases the problematic bubble formation in the bead, but does not affect weld strength. To reach maximum joint strength, a critical minimum energy level is needed. If that level is exceeded, it results in excess bead formation and reduced strength.

Takasu (2003) introduced a new machine configuration where welding takes place by rotating a short pipe between the two long specimens that need to be welded. As a result, there is no need for large equipment and no reduction in work efficiency at the construction site. Furthermore, the author conducted experiments on workpieces manufactured by 3 different polyethylene pipe manufacturers at temperatures of -5, 23 and 40°C. The mechanical properties of the PE pipe weld zones satisfied the standard values of the Japanese Industrial Standards (JIS) and the weld zone showed similar or better results than that of conventional welding, and maintained an adequate long-term stability performance. Regardless of the differences in the surrounding temperatures and the piping supplied by the manufacturers, the welds have good quality. Takasu also states that, during the cooling stage, the welding pressure has to be maintained within the optimum range to manage joint elongation and creep performance.

Lin et al. (2004) conducted an experimental study on spin friction welding of PP with PP, HDPE with HDPE, and nylon-6 with nylon-6. Three different pressures (0.98, 1.37, and 1.77 MPa) were used for HDPE welding at 460 rpm for 8, 10, and 12 s to closely weld the two parts. C. B. Lin & Wu (2000), performed a very similar study on PMMA with PMMA, PVC with PVC and PMMA with PVC. Both studies showed that the heat affected zone is composed of three distinct regions: the plasticized region, the undeformed region, and the partly plasticized region. Lin et al. concluded that the bonding strength increases with increasing friction pressure: a friction pressure of 1.77 MPa at a spinning time of 8 s gives the best bonding strength because it produces a larger plasticized zone. In addition, the bonding strength with times of 8 and 10 s was always greater than that with a spinning time of 12 s. The authors optimized the process but ignored the effect of rotary speed. In addition, the optimization was performed through a trial-and-error methodology. According to Maalekian (2007), the optimization of the friction welding parameters is mainly based on the trial-error method.

Hassan & Khdir (2018) studied the influence of rotational speed and friction time on the microstructure and tensile strength of 27 mm rod joints of ABS with PE, ABS with ABS, and PE with PE. Speeds varied between 650 and 1030 RPM, time ranged between 60 and 105 sec, but feed rate was kept constant. Therefore, the optimization did not take the impact of feed rate into account. Also, it was through trial-and-error. The study reveals that ABS and PE cannot be welded through RFW. ABS welds fail at a critical rotary speed because the latter produces a localized flash temperature at the interface which leads to surface melting and thermal softening near the contact surfaces. As for PE welds, the best values of the tensile strength can be obtained at high speed with high friction time in the studied range (650-1030 RPM, 60-105sec). The ratio of joint tensile strength of the welded material to the ultimate tensile strength of the base materials, known as welding joint

efficiency, grows with both time and speed. The optimum efficiency of polyethylene is 58.5% and is obtained at 1030 rpm and 80 sec. Peak stress rises with friction time until reaching 80s. Then, it goes down. PE is viscoelastic and its properties are time dependent. That is, defects in the interface of the welded joints lowers the tensile strength. As the speed increases, the friction time decreases resulting in a low heat input and a weak weld. Also, the average burn-off length increases slightly with friction time, and gradually with increasing speed. As for the macrostructure of fracture location, it is a rough surface. The rate of heat generation across the interface is not uniform, which leads to a concentric rubbing phenomenon from the circumference to the central area of the weld interface.

Hamade et al. (2019) compared rotary friction welding to butt fusion welding of HDPE in terms of weld quality and energy consumption. RFW experiments were performed at a feed rate of 40mm/min and three RPM values equal to 1224 RPM, 1554 RPM and 1884 RPM. Therefore, the effect of rotary speed was only taken into account. The authors concluded that as the feed rate increases, the weld bead reduces in size. With an increase in rotary speed, color changes become apparent because of the higher temperature in the heat affected zone and the melting temperature is achieved quicker (less than 10 seconds). At a rotational speed of 1224 rpm for 8.5 seconds, the maximum temperature was 250°C, thus above the melting point of HDPE (130°C). Added to that, weld quality and the corresponding input parameters are related: as RPM increases, less thrust force, torque, current and weld time are required, and the feed depth is reached faster. This study shows that RFW consumes less power, time, and cost than conventional fusion welding processes.

Bindal et al. (2021) studied the effects of welding pressure and rotational speed on the joint overlap distance and weld strength for polypropylene parts welded in a shear type joint configuration. Spin time, spin initiate distance and pressure are preset. Burst tests are

performed and the fracture surfaces of failed burst tests are examined. To join the parts successfully, a minimum distance of 14.1mm at 64.1 kPa and 1100 rpm is required. The researchers deduced that a good quality weld with high strength results from a narrow range of welding pressures (64.5 to 65.2 kPa in their case), so process optimization should take place within that range. As for the joint overlap distance, it is proportional to rotational speed at optimal welding pressure, and is affected by spin time, spin initiate distance, and rotational speed.

## **2.4 Aim, Objectives and Scope**

Considering the reviewed literature, there are many studies on modelling and optimization of RFW of metals but very few on plastics, especially modelling studies. Only two studies that include modelling of RFW of plastics (Kouta et al., 2020; MADEN & ÇETİNKAYA, 2021) were found in the literature. The purpose of this research work is to optimize the input parameters of continuous drive rotary friction welding of HDPE pipes through numerical modelling and Design of Experiment (DOE) methodology.

To achieve this aim, the following objectives have been met:

1. Obtain the mechanical properties of HDPE:
  - a. Curve fit the data found in the literature using a modified Zerilli Armstrong model
  - b. Extrapolate the data to a wide range of temperatures, strain and strain rates
  - c. Transform the resulting true stress strain curves into stress vs plastic strain curves
  - d. Find the elastic properties of HDPE
  - e. Find the data that describe the thermal behavior of HDPE

2. Create the 2D finite element model by replicating the experimental study of Hamade et al. (2019):
  - a. Define the modelling technique and geometry
  - b. Design the mesh
  - c. Apply the proper boundary conditions and process parameters
  - d. Choose an appropriate friction coefficient
3. Validate the model based on a study in the literature to make sure that the model captures the physical aspects of friction welding
4. Create and run a test matrix using the Taguchi method:
  - a. Select the factors, levels and responses in the DOE. Factors are the most important input parameters according to the literature and levels include common process values
  - b. Run the tests using the generated model
5. Analyze the results:
  - a. Discuss the thermal and mechanical behavior of rotary friction welded HDPE
  - b. Calculate the S/N ratio and perform ANOVA to determine the optimal parameters
6. State the study's limitations and provide insights into future work

As for the scope of this study, the results will only be applicable to HDPE. The results are valid for the selected pipe diameter and thickness, so more research should be performed to draw a general conclusion about optimum parameters for different diameters and thicknesses. The forging state will not be considered because the model will be validated against a study in the literature, and that study doesn't take forging into account. The cooling stage of FW will also not be considered since the response used in the

optimization process is the power consumption, and no forging is applied, so there will be no power consumption during the cooling stage. In addition, this will avoid complexity and extra computation time. This study will optimize the three most significant parameters in the RFW process and will keep the other parameters constant.

# CHAPTER THREE

## 2D FEM MODEL

### 3.1 Modelling Using DEFORM 2D

During friction welding, heat is generated by friction between the two surfaces and plastic deformation (Nguyen & Weckman, 2006). Steep temperature gradients exist close to the welding interface, and in a few seconds, result in extensive deformation. The plastic work, along with friction, lead to increased temperatures (L. Wang et al., 2005). Since the mechanical deformation is under direct effect of the large temperature gradients, a coupled thermo-mechanical model is needed to accurately capture the process physics. The evaluation of the thermal and mechanical behavior at the weld interface is crucial for weld quality. A coupled thermo-mechanical model can replicate the process of friction welding by interpreting heat transfer equations and mechanical deformation simultaneously while considering their interactions.

Based on the input temperature and friction conditions in each time step, the velocity field is calculated for the deformation analysis. Then, the thermal analysis is performed to evaluate the temperature evolution by taking into account the heat generated by friction and plastic deformation, heat conduction between the specimen and heat losses to the environment (L. Wang et al., 2005).

Friction generated from torsion has a large effect on both heat generation and joint deformation. The commercial FEM code DEFORM-2D was chosen because it has a special element for torsion, called 2.5D element (DEFORM V11.0 Documentation). The 2D axisymmetric model contains three velocity components: radial, axial and circumferential. To maintain the axisymmetric computational efficiency while introducing

torsion, an assumption that no velocity gradient exists in the circumferential direction is made. This means that the circumferential velocity includes radial and axial terms only. This results in the 2.5D element that in addition to the shear stress component,  $\sigma_{rx}$ ,  $\sigma_{r\theta}$  and  $\sigma_{r\theta}$  can be evaluated (Lee et al., 2001).

In a coupled thermo-mechanical solution, DEFORM evaluates friction based on the minimum work-rate principle. In other words, it is assumed that material flows along the path of least resistance by evaluating the minimum of the work rate functional.

$$\delta\pi = \int_V \bar{\sigma} \cdot \delta\bar{\epsilon} \cdot dV - \int_S F_i \cdot \delta u_i \cdot dS + \bar{K} \cdot \int_V \dot{\epsilon}_v \cdot \delta\dot{\epsilon}_v \cdot dV = 0 \quad (1)$$

Where  $\bar{\epsilon}$  is the effective strain rate,  $\dot{\epsilon}_v$  is the volumetric strain rate,  $F$  is surface traction,  $u$  is the velocity, and  $\bar{K}$  is a penalty constant that avoids volume alteration by forcing a material incompressibility factor on the velocity field (Mohammed et al., 2009).

As for the thermal calculation, it is done by solving equation 2 (L. Wang et al., 2005):

$$\int_V kT\delta T dV + \int_V \rho c \dot{T} \delta T dV - \int_S q_n \delta T dV - \kappa \left( \int_V \sigma_{ij} \epsilon_{ij} \delta T dV + \int_S (f_s)_t (u_s)_t \delta T dS \right) = 0 \quad (2)$$

Where  $k$  is the thermal conductivity,  $\rho c$  is the heat capacity,  $q_n$  is the interface heat flux,  $\kappa$  is the coefficient used for the conversion from mechanical energy to thermal energy,  $f_s$  is the traction vector, and  $u_s$  is the sliding velocity vector.

### 3.2 Numerical Model

The current study replicates the experimental work of Hamade et al. (2019) through a numerical model. The steps undertaken to develop a 2D axisymmetric FE model of CDFW of HDPE are summarized below:

- Defining the modelling method and geometry
- Determining the necessary material properties
- Developing the mesh design



- Defining boundary conditions
- Determining the proper solving conditions
- Running the model and generating results

### 3.2.1 Modelling Method and Geometry

In this study, a 2D axisymmetric model is adopted. In the literature, 2D modelling has been a preference for FW because it yields the necessary information without the large computational effort of 3D modelling. The only study implementing a 3D model using DEFORM software package is that of Zhang et al. (2006), which compared to the ordinary 2D model, does not appear to have any additional value.

As for the geometry, an axisymmetric model is adopted because there's axial symmetry in FW. It is safe to assume that the pipes which have identical geometry and material are joined symmetrically (C. J. Bennett et al., 2007; D'Alvise et al., 2002; Fu et al., 2003; Q. Z. Zhang et al., 2006). As a result, only half of the longitudinal model can be employed, as shown in figure 8.

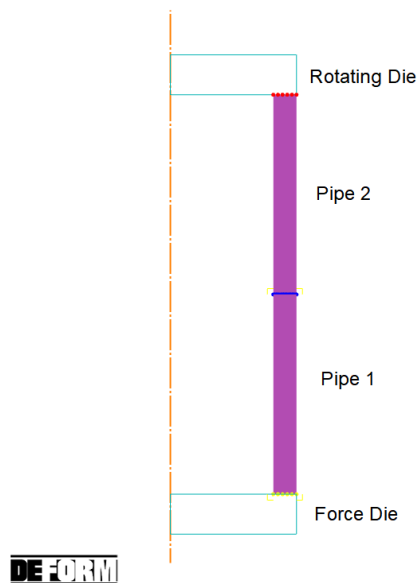


Figure 8 - Model Geometry

The pipes have an outside diameter of 63mm and a thickness of 5.8mm. A length of 50 mm was selected for each pipe such that their extremities stay at the ambient temperature 25°C during the entire simulation.

The rotating and stationary dies are modelled as rigid bodies. The pipes, however, are modelled as elasto-plastic bodies: this means that the pipes are elastic until the yield point is reached. After that, they are treated as plastic. Therefore, the total strain is a combination of elastic strain and plastic strain (DEFORM V11.0 Documentation).

### **3.2.2 Mesh Design**

The computation time and accuracy of results are directly influenced by element size. Since there are steep temperature gradients and large deformations during RFW, a sufficiently fine mesh is necessary at the weld interface to capture the details of the deformations and ensure precise results. The material further away from the mating surfaces, can be represented with a coarser mesh because it experiences little to no deformation. This still permits good thermal predictions while reducing the computational time and total number of elements.

The mesh consisted of a total of 5039 elements with 5212 nodes for the rotating pipe and 4984 elements with 5166 nodes for the stationary pipe. A 5000 element was assigned for each with three friction mesh windows to gradually increase the mesh size as the volume of material gets away from the weld interface. Their relative element sizes are 1, 1/10 and 1/100, as shown in figure 9. The largest element size is 1.16 mm, and the smallest is 0.14 mm.

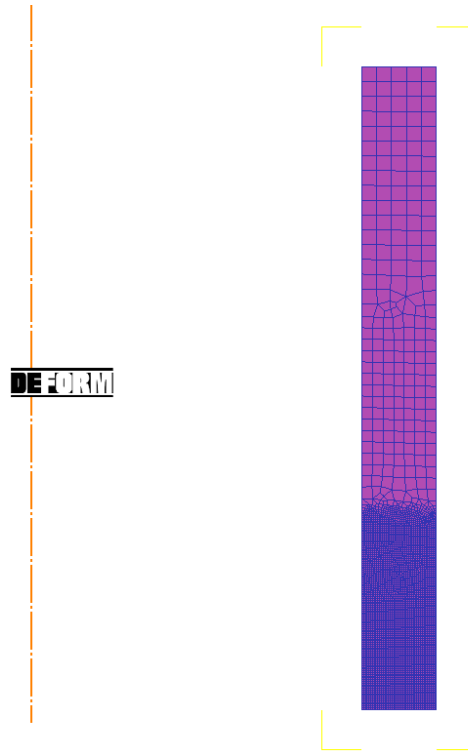


*Figure 9 - Model Mesh (rotating pipe)*

In DEFORM, when the solver cannot converge in a time step, automatic re-meshing is triggered. According to Yang (2010), DEFORM became the most popular FEM software to simulate FW because of this capability, which is very important where there is large plastic deformation. However, forcing a re-mesh is more effective because it maintains the solution precision, and prevents excessive iterations at difficult time steps (C. J. Bennett et al., 2007). For this model, re-mesh is triggered after a maximum step increment of 2. Provided the substantial deformation at the weld interface, this overcomes extreme element distortion.

### **3.2.3 Material Properties**

During FW, the material experiences a broad range of strains, strain rates and temperatures. As a result, a considerable material database is needed to replicate the material's behavior in the FE model. For this study, the required material properties include:

- Plastic data: flow stress
- Elastic data: young's modulus, Poisson's ratio, and thermal expansion
- Thermal data: thermal conductivity, heat capacity and density

### 3.2.3.1 *Plastic Data*

Flow stress data is a representation of true stress versus plastic strain, and it's sensitive to changes in temperature, strain and strain rate. Flow stress is key for proper modelling of friction welding (C. J. Bennett et al., 2007) because the resulting stress and strain fields and weld distortion depend on the plastic yield strength of the material (El-Hadek, 2009).

The flow stress data was extracted from the study of Zhang et al. (2021). The authors investigated the mechanical properties of HDPE by performing static and dynamic compression tests at different temperatures and strain rates. The data was processed and extrapolated to span the range of temperatures, strain and strain rates expected in the model. The DEFORM-2D FE software applies linear or logarithmic extrapolation beyond the limits of any data present in the flow stress table. This may lead to inaccuracies, which emphasizes the importance of data extrapolation beforehand.

Zhang et al. (2021) provided true stress – true strain curves for HDPE at a strain rate of  $0.001 \text{ s}^{-1}$  and temperature from  $-40$  to  $120^\circ\text{C}$ , a strain rate of  $935 \text{ s}^{-1}$  and temperature from  $-40$  to  $120^\circ\text{C}$ , and a temperature of  $25^\circ\text{C}$  and strain rate from  $0.001$  to  $5450 \text{ s}^{-1}$ . The steps taken to determine the true stress – plastic strain curves of HDPE at different temperatures and different strain rates are elaborated below.

Data was not provided in a numerical format, so a web-based tool was employed to extract data points from the provided stress strain plots.

After extracting the data, Excel was used to perform non-linear curve fitting. The modified Zerilli Armstrong model was found adequate to simulate the HDPE behavior

(Meyer, 2006). This constitutive equation was previously used in the studies of Ammouri & Hamade (2014-a, 2014-b) and Ammouri et al. (2015).

$$\sigma = C \sqrt{\varepsilon_r \left(1 - e^{-\frac{\varepsilon}{\varepsilon_r}}\right)} \quad (3)$$

Where  $\sigma$  is the true stress and  $\varepsilon$  is the true strain.  $C$  and  $\varepsilon_r$  are material constants that will be determined through curve fitting.  $\varepsilon_r$ , which Zerilli and Armstrong refer to as recovery strain, influences the strain at which stress saturation takes place (Meyer, 2006). Zerilli-Armstrong model was first applied on polymers in 2007 by accounting for increased strain hardening with rising strains at higher strain rates (Zerilli & Armstrong, 2007).

At each temperature and strain rate, the data was fitted to the Zerilli-Armstrong model to determine the constants  $C$  and  $\varepsilon_r$  that minimize the root mean square error (RMSE).

The results are shown in table 1 and figures 32 – 46 in Appendix A.

*Table 1 - Zerilli Armstrong model constants*

Temperature (°C)	Strain rate (s <sup>-1</sup> )	C	$\varepsilon_r$
25	0.001	79.954	0.220
50	0.001	58.309	0.171
70	0.001	37.476	0.273
90	0.001	27.257	0.449
120	0.001	15.119	0.818
25	935	331.289	0.025
50	935	276.029	0.030
70	935	231.040	0.039
90	935	197.006	0.052
120	935	176.280	0.057
25	0.01	92.711	0.198
25	0.1	107.278	0.202
25	2209	373.139	0.022
25	2900	388.338	0.021
25	5450	498.790	0.013

Curve fitting results are summarized in figure 10. Dashed lines represent the fit according to the modified Zerilli Armstrong model.

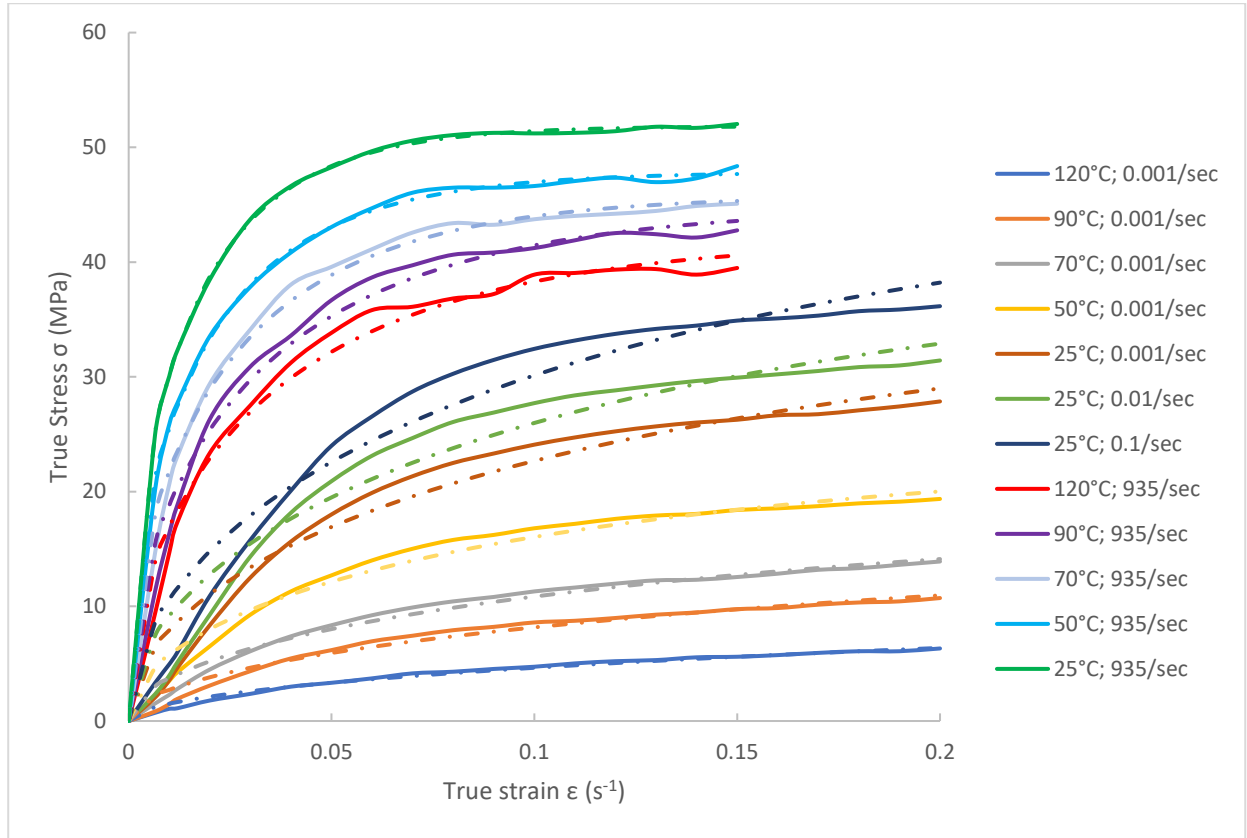


*Figure 10 - Zerilli Armstrong model results*

The typical tensile stress strain curves of HDPE show a non-linear behavior with no obvious yield point. As the temperature increases, the stress decreases and ductility increases, and as the strain rate increases, the stress increases. HDPE tends to have an almost fully plastic behavior at high temperatures (Brown et al., 2007).

After determining the model constants, the data is extrapolated to cover the temperatures and strain rates expected in the process simulation. The constants  $C$  and  $\epsilon_r$  are plotted against the temperature first. Results are summarized in figures 11 - 14 and show that both constants vary exponentially with temperature.

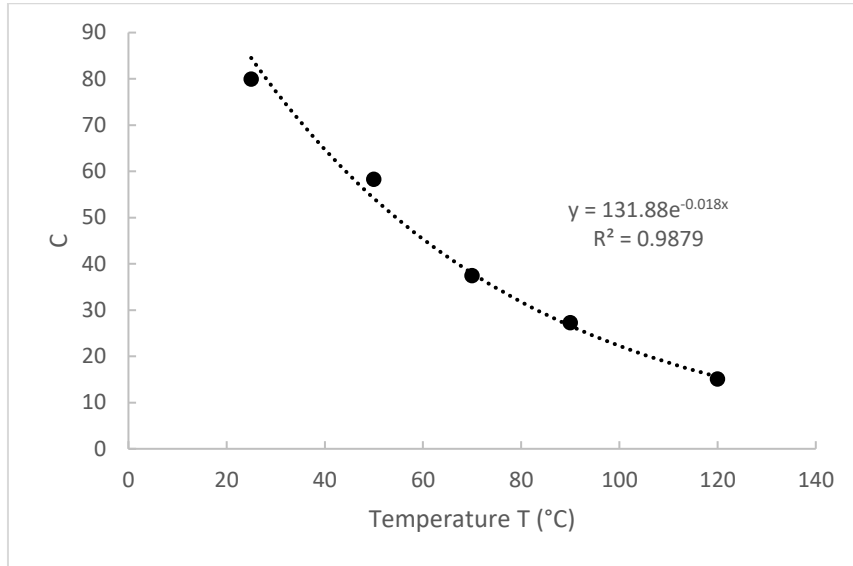


Figure 11 - Constant  $C$  vs Temperature at  $0.001\text{s}^{-1}$

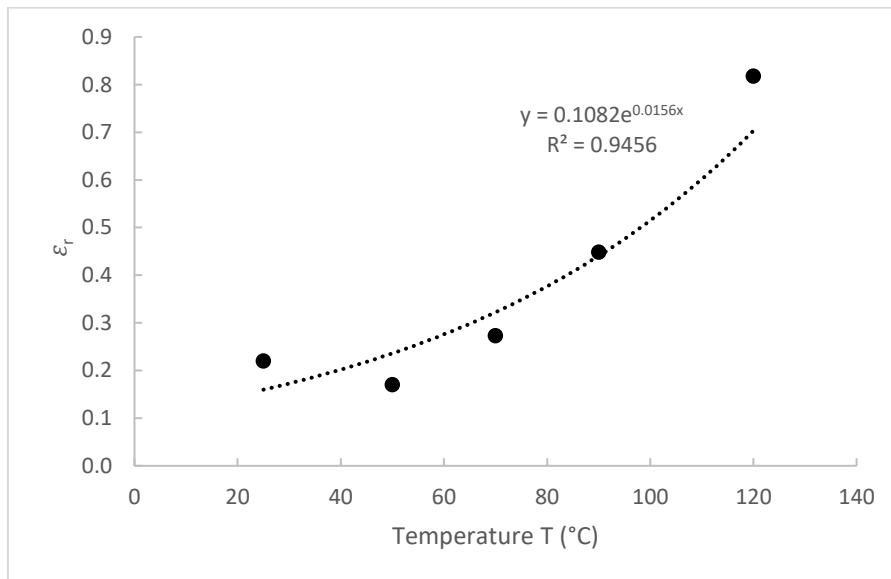


Figure 12 - Constant  $\epsilon_r$  vs Temperature at  $0.001\text{s}^{-1}$

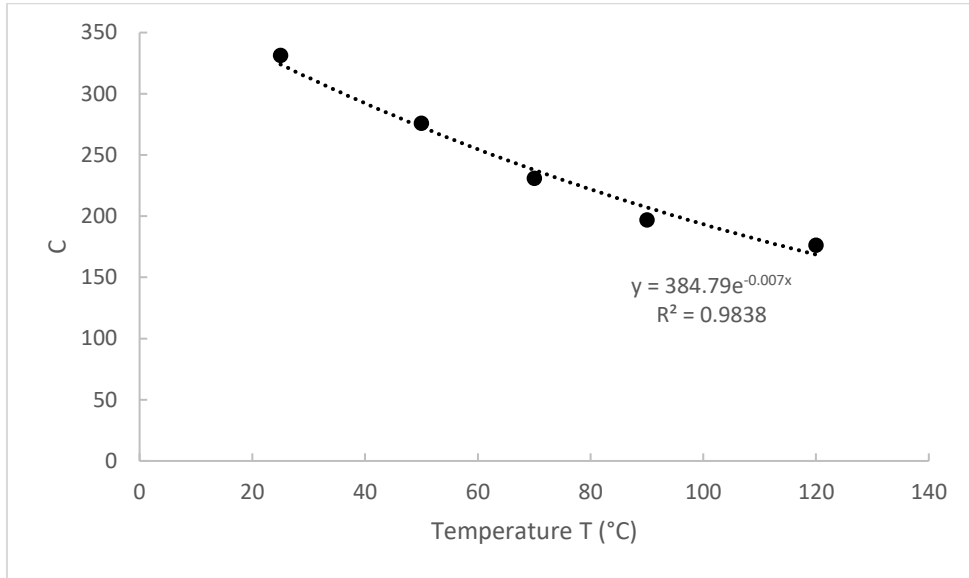


Figure 13 - Constant  $C$  vs Temperature at  $935s^{-1}$

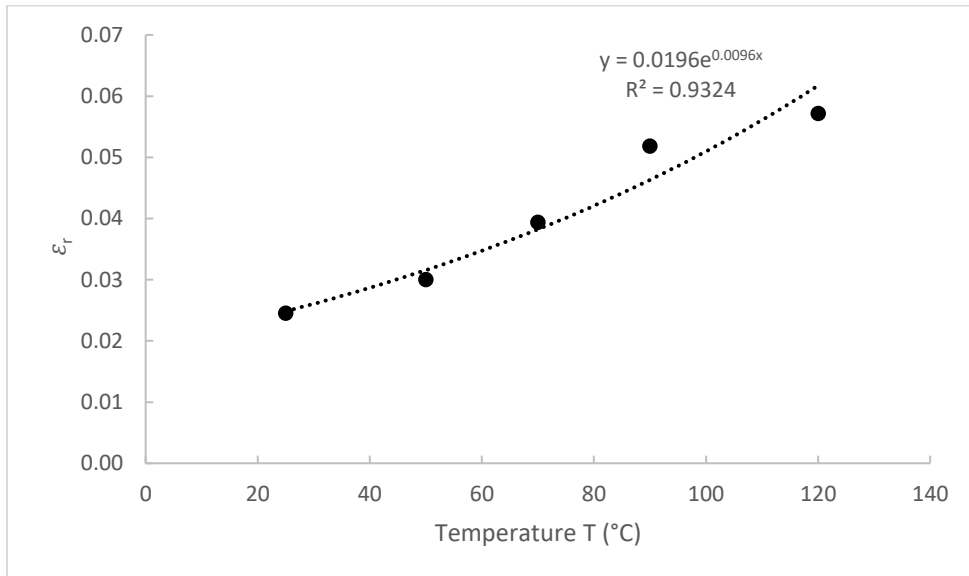


Figure 14 - Constant  $\epsilon_r$  vs Temperature at  $935s^{-1}$

The data extrapolated to higher temperatures at both  $0.001$  and  $935 s^{-1}$  is shown in table 2.



Table 2 - Zerilli Armstrong model constants extrapolated to higher temperatures

Strain rate (s <sup>-1</sup> )	Temperature (°C)	C	ε <sub>r</sub>
0.001	150	8.863	1.123
	180	5.165	1.794
	210	3.010	2.864
	240	1.754	4.573
	280	0.854	8.535
	350	0.242	25.438
	500	0.016	264.073
935	150	134.653	0.083
	180	109.147	0.110
	210	88.473	0.147
	240	71.715	0.196
	280	54.201	0.288
	350	33.205	0.564
	500	11.620	2.382

The strain rates 935, 2209, 2290 and 5450 s<sup>-1</sup> are very large values and will not be reached in the process. However, the high strain rates are needed to extrapolate to a strain rate of 10 s<sup>-1</sup> which is expected to be reached in the process. The flow stress data extraction and extrapolation was limited to the study of Zhang et al. (2021) because of the lack of flow stress data for HDPE covering a wide range of temperatures and strain rates. The flow stress data was extrapolated to higher strain rates at 25°C, and it was found that there is a power curve fit between the Zerilli Armstrong constants and the strain rate. As the strain rate increases, the tensile properties of HDPE increase (Brown et al., 2007; Drozdov & Christiansen, 2008; Fatemi et al., 2014; Milisavljević et al., 2012; Mortazavian & Fatemi, 2015). This is achieved using the power curve fit, as can be seen in figure 15. The stress-strain curves of 10, 100, 300 and 600 s<sup>-1</sup> lie between the ones at 0.1 and 935 s<sup>-1</sup>. The equations are  $C = 163.32\dot{\epsilon}^{0.1034}$  and  $\epsilon_r = 0.0731\dot{\epsilon}^{-0.16}$ . Extrapolated results are shown in table 3.

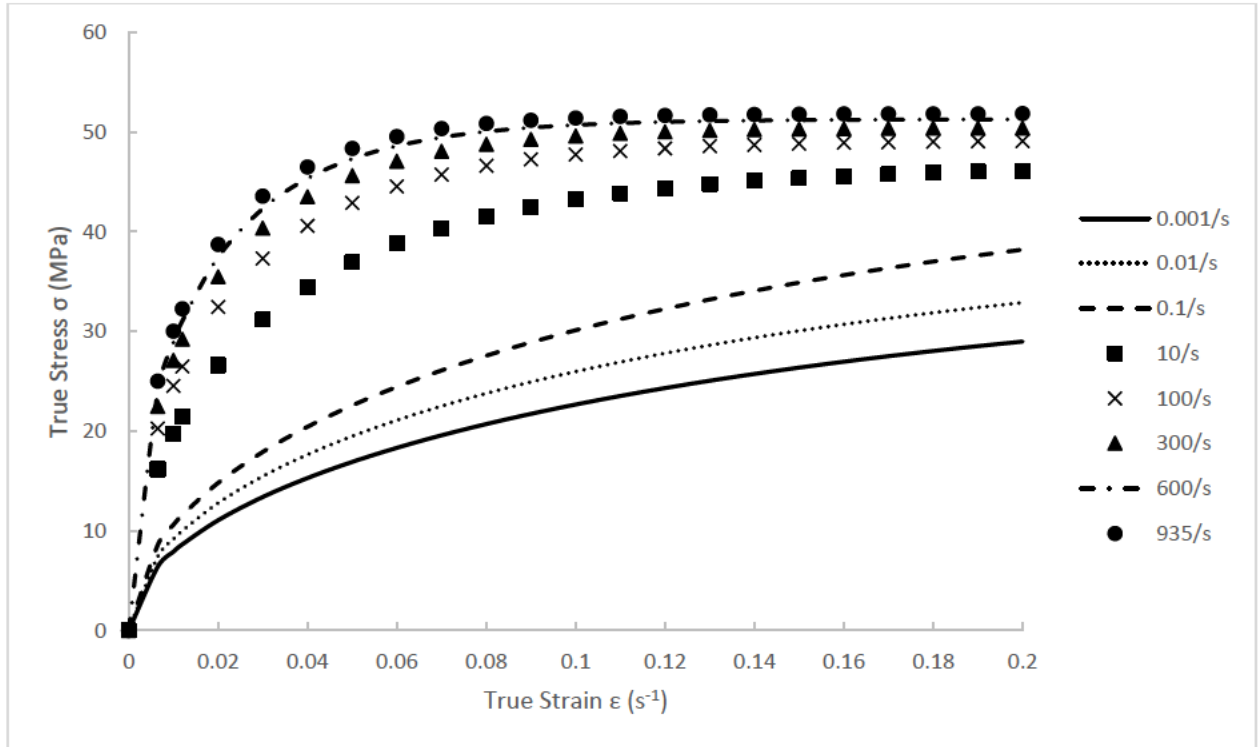


Figure 15 - True Stress True Strain Curves at 25°C and different strain rates

Table 3 - Zerilli Armstrong model constants extrapolated to higher strain rates at 25°C

Strain rate (s <sup>-1</sup> )	C	ε <sub>r</sub>
10	207.224	0.051
100	262.930	0.035
300	294.560	0.029
600	316.446	0.026

The same calculations (i.e., power curve fit) are done for temperatures 50, 70, 90, 120, 150, 180, 210, 240, 280, 350 and 500°C using the model constants at 0.001 and 935 s<sup>-1</sup>. Results are summarized in table 14 in Appendix A.

In DEFORM, the flow stress input is the true stress vs plastic strain. Therefore, the plastic strain should be calculated. The total strain is the summation of the elastic and plastic strain. The plastic strain can then be calculated using equations 4 and 5.

$$\varepsilon_P = \varepsilon_T - \varepsilon_E \quad (4)$$

$$\varepsilon_P = \varepsilon_T - \frac{\sigma}{E} \quad (5)$$

$\varepsilon_P$ ,  $\varepsilon_E$ ,  $\varepsilon_T$  are the plastic, elastic and total strain, respectively.  $\sigma$  is the true stress, and  $E$  is young's modulus.

The flow stress is temperature and strain rate dependent, which means that young's modulus is also temperature and strain rate dependent. To determine young's modulus, the slope of the linear portion in the stress strain curve was calculated, then extrapolated to higher temperatures and strain rates.

Similar to the extrapolation at new strain rates discussed earlier, a power curve fit was found to be the best fit of elastic modulus with strain rate, whereas an exponential fit was found to be the best fit with temperature, as seen in figure 16.

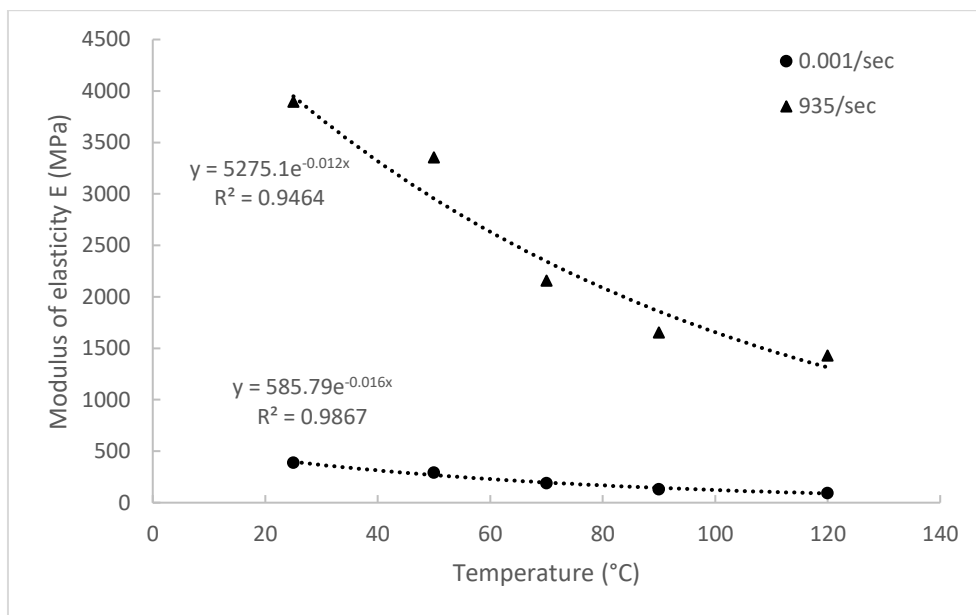


*Figure 16 - Variation of Elastic Modulus with Temperature*

Table 4 shows the resulting elastic moduli.

Table 4 - Extrapolated elastic moduli

Temperature (°C)	Strain Rate (s <sup>-1</sup> )							
	0.001	0.01	0.1	10	100	300	600	935
<b>25</b>	359.0	441.0	504.0	1597.8	2451.4	3006.9	3420.4	3898.0
<b>50</b>	273.0	415.6	632.7	1466.3	2232.1	2727.7	3095.5	3357.0
<b>70</b>	189.0	284.1	427.2	965.7	1451.9	1763.7	1994.1	2157.0
<b>90</b>	135.0	205.4	312.4	723.0	1099.9	1343.7	1524.5	1653.0
<b>120</b>	84.0	135.1	217.2	561.6	903.1	1132.8	1306.9	1432.0
<b>150</b>	50.7	81.7	131.5	341.1	549.2	689.4	795.7	872.0
<b>180</b>	31.4	51.6	84.7	228.7	375.7	476.1	552.9	608.4
<b>210</b>	19.4	32.6	54.6	153.4	257.0	328.9	384.2	424.4
<b>240</b>	12.0	20.6	35.2	102.9	175.9	227.3	267.1	296.1
<b>280</b>	6.3	11.1	19.6	60.4	106.0	138.7	164.4	183.2
<b>350</b>	2.1	3.8	7.0	23.8	43.7	58.5	70.3	79.1
<b>500</b>	0.2	0.4	0.8	3.2	6.6	9.2	11.4	13.1

After the determination of the modulus of elasticity at various temperatures and strain rates, the plastic strain was calculated. In the elasto-plastic model, the stress at which the plastic strain equals zero is equivalent to the yield stress. The yield stress rises as the accumulated effective plastic strain rises (DEFORM V11.0 Documentation).

Briscoe & Hutchings (1976) and Kukureka & Hutchings (1981) deduced that the yield stress of HDPE depends on the strain rate. As the strain rate increases, so does the yield stress (Drozdov & Christiansen, 2008; Fatemi et al., 2014; Mortazavian & Fatemi, 2015) because the molecular mobility of the polymer chains is reduced and it becomes stiffer (Lamri et al., 2020; Merah et al., 2006). The Young's modulus also increases as the strain rate increases (Brown et al., 2007; Milisavljević et al., 2012).

The flow behaviour of HDPE is strongly dependent on the temperature (Lamri et al., 2020) and strain rate (Brown et al., 2007). As the temperature increases, the yield point decreases (McKelvey et al., 2018). Temperature has a larger impact on stress than strain rate: according to Brown et al. (2007), an increase in temperature from  $-75$  to  $100^{\circ}\text{C}$  influences the stress-strain curve more than an increase in strain rate from  $10^{-4}$  to  $2600\text{ s}^{-1}$ . After reaching the yield stress, HDPE displays a flat flow behaviour (Brown et

al., 2007). Walley & Field (1994) studied the flow stress behaviour of polymers and concluded that polymers belong to three different categories in a yield stress versus logarithmic of strain rate plot:

- A linear trend, regardless of the strain rate
- A bilinear trend with a sudden rise in yield stress gradient at a  $10^3 \text{ s}^{-1}$  strain rate
- A reduction in yield stress at a  $10^3 \text{ s}^{-1}$  strain rate

According to Fatemi et al. (2014) and Siviour et al. (2005), HDPE belongs to the first category meaning that the yield stress varies linearly with the logarithmic of strain rate. PE may be the only polymer belonging to this category (Shen, 2012). To double check, the yield stress is plotted against the logarithmic of strain rate and shows a linear behavior (figure 17). According to Brown et al. (2007) and Merah et al. (2006), yield stress can be reasonably represented linearly as a function of temperature. When yield stress is plotted against temperature at  $0.001 \text{ s}^{-1}$  in figure 18, it exhibits a linear variation. This validates the accuracy of the data. According to Bonds (2000), the tensile strength of HDPE pipe material decreases from 21 MPa at  $23^\circ\text{C}$  to 10MPa at  $60^\circ\text{C}$ . The results shown in figure 18 at  $0.001 \text{ s}^{-1}$  are very similar.

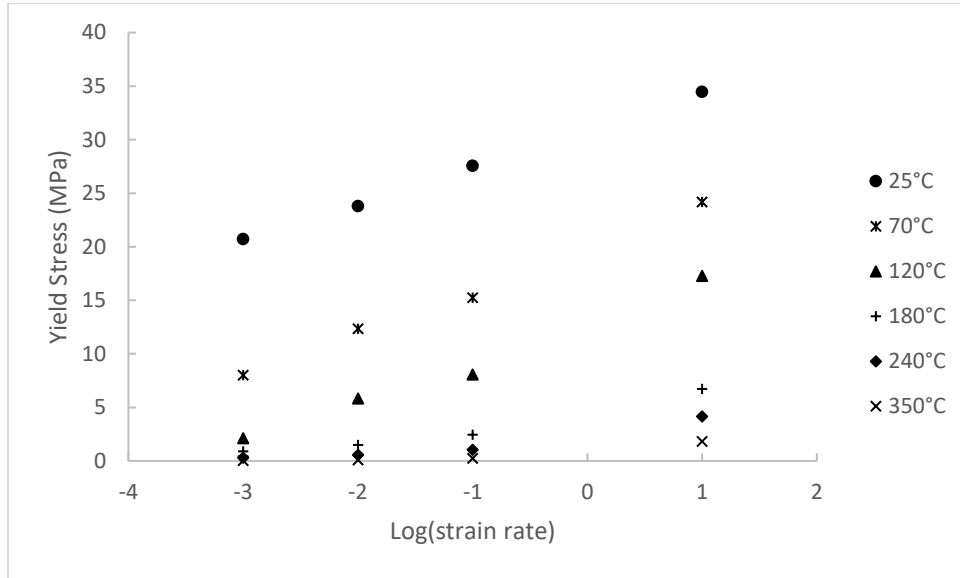


Figure 17 - Yield Stress variation with strain rate at different temperatures

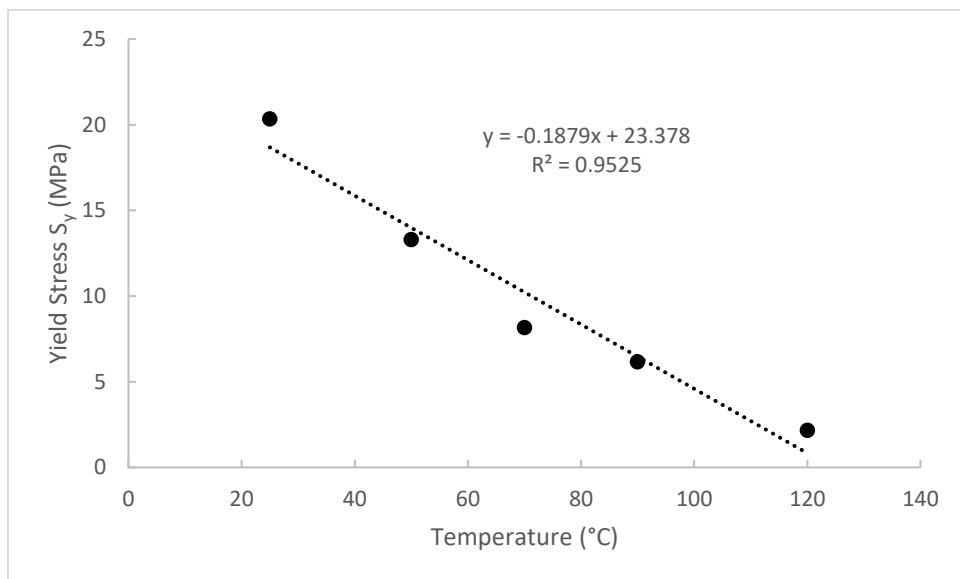


Figure 18 - Yield Stress variation with temperature at  $0.001s^{-1}$

The data was input into DEFORM in a tabular format because it is versatile and can represent HDPE behavior under the needed conditions. The tabular format requires data points at specific strains at each temperature and strain rate. Therefore, the true stress – plastic strain curves are plotted and used again in a web-based tool to gather the required data. The final dataset used in DEFORM is shown in tables 15 - 26 in Appendix A.

### 3.2.3.2 Elastic Data

The elastic data required in the finite element model include:

- Poisson ratio:  $\nu = 0.4$  (Balobanov et al., 2021; S. Li & Qi, 2014)
- Thermal expansion coefficient:  $\alpha = 0.000128/^\circ\text{C}$  (Alfredo Campo, 2008)
- Elastic modulus

As mentioned in section 3.2.3.1, the elastic modulus was calculated for the given conditions, then extrapolated to cover the temperatures and strain rates expected in the process. The extrapolated values were used to calculate the plastic strain. Here, DEFORM requires only the elastic modulus at the limiting strain rate, because it only includes the option of a modulus of elasticity as a function of temperature, not both temperature and strain rate. The limiting strain rate is defined as a threshold below which a plastic material is treated as a rigid material (DEFORM V11.0 Documentation). HDPE will behave elastically for a very short period before it reaches the yield point. At this point, the strain rate is relatively small. Therefore, it is assumed that the elastic modulus that DEFORM requires is that of the strain rate of  $0.001 \text{ s}^{-1}$ . In other words, the variation of the elastic modulus with temperature at  $0.001 \text{ s}^{-1}$  was used, and  $0.001 \text{ s}^{-1}$  is indicated as the limiting strain rate.

### 3.2.3.2 Thermal Data

The thermal data required in the finite element model include:

- Density:  $0.952 \text{ g/cm}^3$  (Hamade et al., 2019)
- Thermal conductivity
- Heat capacity

Temperature dependent thermal conductivity and heat capacity were used in the model to represent the real process conditions and yield acceptable results. Thermal properties vary with the material phase change as the temperature changes, so the use of constant thermal

properties would generate various errors (Tashkandi, 2021). The study of Woo et al. (1995) provides expressions for both properties as a function of temperature:

$$K_p = 0.17 + 5(\rho_p - 0.9) - 0.001 \times T \quad (T \leq 135^\circ\text{C}) \quad (6)$$

$$K_p = 0.25 \quad (T > 135^\circ\text{C})$$

$$C_p = 2250[1 + 5.5e^{-a(T-135)^2}] \quad (7)$$

$$a = 0.005 \quad (T \leq 135^\circ\text{C})$$

$$a = 0.05 \quad (T > 135^\circ\text{C})$$

Where  $K_p$  is the thermal conductivity in  $\frac{W}{m^\circ\text{C}}$ ,  $C_p$  is the heat capacity in  $J/Kg^\circ\text{C}$ ,  $T$  is the material temperature and  $\rho_p$  is the material density.

The data used in the model is summarized in table 5. DEFORM requires that heat capacity be equivalent to heat energy per unit volume. Therefore, the specific heat of HDPE is converted to heat capacity by multiplying it by the density.

*Table 5 - Thermal properties of HDPE*

Temperature ( $^\circ\text{C}$ )	Thermal conductivity ( $\frac{W}{m^\circ\text{C}}$ )	Heat Capacity ( $\text{N/mm}^2^\circ\text{C}$ )
25	0.405	2.142
50	0.380	2.142
75	0.355	2.142
100	0.330	2.168
125	0.305	9.287
135	0.295	13.923
140	0.250	5.517
150	0.250	2.142
450	0.250	2.142

### 3.2.4 Process Parameters

The process parameters implemented in the model are the same as case A3 and B3 in the matrix tested by Hamade et al. (2019). The rotational speed is applied on the rotary die, while an axial speed is applied on the other die. The rotation and translation are applied for a total axial shortening of 5 mm. The forging time and forging pressure were



not taken into account because they were not considered by Hamade et al. (2019). Table 6 summarizes the model input parameters for both experiments.

*Table 6 - Model input process parameters*

Input Parameters	Experiments	
	A3	B3
Rotational speed (RPM)	1224	1554
Feed rate (mm/sec)	0.667	0.667
Axial shortening (mm)	5	5

### 3.2.5 Boundary Conditions

The initial temperature for the specimen was set at 25°C. A sticking boundary condition was added between the pipes and adjacent die to make sure that rotational and translational movement are being transferred from the dies to the pipes. The contact interface is permitted to move radially during the upset stage. Heat transfer includes conduction, convection and radiation and has an important role in establishing weld quality because the temperature significantly affects the mechanical and thermal behaviors at the weld interface. The outer and inner surfaces of the pipes are assumed to have an adiabatic boundary condition in the model since the process is very short, and convection and radiation are negligible compared to conduction between the specimens. This assumption was implemented in most previous studies (El-Hadek, 2009; Fu et al., 2003; W. Li & Wang, 2011; Maalekian et al., 2008; Nguyen & Weckman, 2006; L. Yang, 2010). Mohammed et al. (2010) concluded that conduction dominates the other heat transfer mechanisms during the welding stage, and that considering convection and radiation has little influence because the temperature gradient in the pipes surpasses that between the pipes and the environment. Conduction also remains the controlling heat transfer mode during the primary stage of cooling. L. Wang et al. (2005) has also stated that the heat exchange with the environment is only necessary during the cooling phase, which is not simulated in this study.

### 3.2.6 Inter-Object Relations and Friction Coefficient

The temperature at the weld interface increases because the kinetic energy is being converted into thermal energy due to friction. Therefore, the friction plays a very important role in the process of welding. However, the frictional behavior of materials is not well understood because of the complexity of the process (Blau, 2017).

The coefficient of friction is usually determined experimentally because it is a function of many parameters: interface temperature, rotational speed, material properties, the presence of surface films and surface rigidity (Maalekian et al., 2008). Even for the same material, several coefficients of friction values have been reported because of the various affecting parameters. According to Maalekian et al. (2008), describing the friction coefficient analytically is the most difficult task. This is due to the fast shift in interface conditions and material properties during the welding process (Mohammed et al., 2009). The Coulomb friction law is the most common approach used to simplify the determination of the frictional behavior. It states that the frictional stress  $F_s$  is directly proportional to the normal pressure  $P$  (interface pressure between the specimen), and the proportionality factor is the Coulomb coefficient of friction  $\mu$ :

$$F_s = \mu P \tag{8}$$

In addition to the Coulomb friction implementation, it is assumed that the coefficient of friction depends on the material temperature to avoid complexity in the process modelling. According to Ringius & Thorsell (2017), the modification of the friction coefficient mainly influences the temperature gradient.

The coefficient of friction used in this study is extracted from the work of Spalding et al. (1993) and is shown in figure 19. It was assumed that the data varies exponentially with temperature, because friction decreases as the material changes from a solid phase to a liquid phase. At very high temperatures, the coefficient of friction approaches zero. This

assumption yielded reasonable results and the best match between the simulated and experimental results, as will be shown in section 3.2.9.

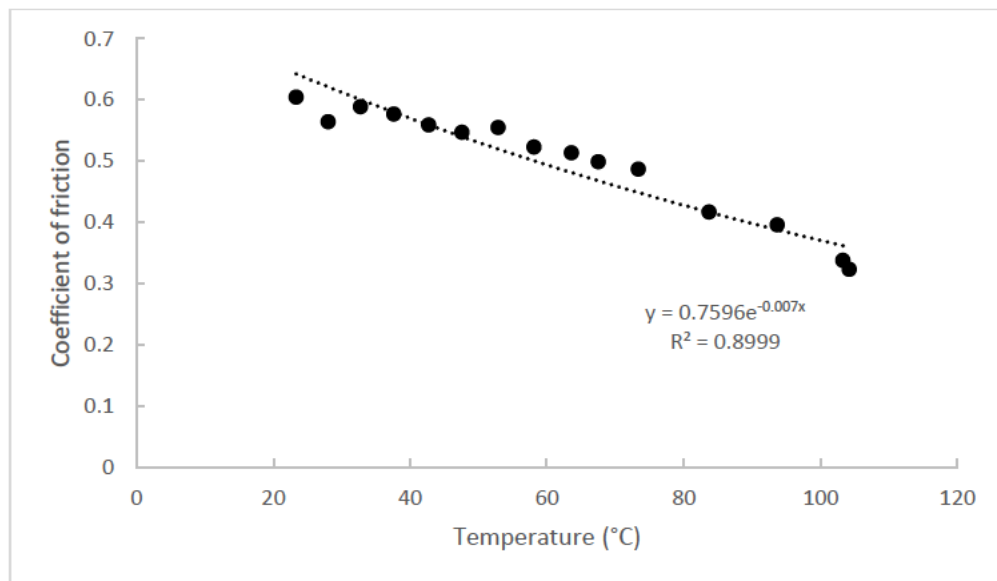


*Figure 19 - Variation of coefficient of friction with temperature*

For inter-object relations, a sticking condition is applied between the workpieces and the dies, where the dies are the master objects, and the workpieces are the slave objects. Self-contact was also applied on both pipes. In other words, a master-slave relationship between the object and itself allows the simulation to proceed even after a defect or fold (DEFORM V11.0 Documentation). When the nodes of the welding interface contact the workpiece, a penalty condition is applied to avoid the penetration of the flash into the pipe, and the flash self contact allows it to slide over the specimen surface. Contact is generated between the workpieces as well, so that they do not pass past each other during the simulation. Heat transfer coefficient was taken as per what DEFORM recommends and that is 11 N/sec/mm/°C.

### **3.2.7 Simulation Controls**

As mentioned earlier, the model is thermo-mechanical so both deformation and heat transfer equations are considered. Torsion is also implemented so that there is no

velocity gradient in the circumferential direction. 2500 simulation steps with 0.002 mm/step account for the total depth achieved (5 mm) and show accurate results. The total welding time for a 40 mm/min feed depth is 7.5 sec. The force die is the primary die in DEFORM.

### **3.2.8 Model Assumptions**

A number of assumptions are made to simplify the model complexity and reduce the computation time:

- An axisymmetric model is assumed because of the friction welding symmetry
- The convection and radiation heat losses are neglected, as previously discussed
- The friction coefficient is based on Coulomb friction law which is the most common in predictive models, and it is a function of temperature only because no experimental data is available, and it is very complex to determine analytically. It is also assumed that the coefficient of friction varies exponentially with temperature.
- The rotational speed does not have any acceleration time: it is immediately applied on the rotating die then immediately removed (Ringius & Thorsell, 2017).

### **3.2.9 Model Results and Validation**

#### **3.2.9.1 Model Validation**

Figures 20 and 21 show the predicted and experimental load data for experiment A3 and B3. The peak loads match closely with a deviation of 2.56% and 10.84% for A3 and B3, respectively. There is a difference between the predicted and experimental data when the load stabilizes, and this can be attributed to the mesh characteristics, coefficient of friction, or material data, especially that flow stress and elastic modulus have been extrapolated to higher temperatures and strain rates with limited data from the literature. There is also a good match between the model and experimental peak torque values. The

peak torques are equal to 7.8 and 6.7 N.m, which correspond to an error of 11.4% and 13.08% for A3 and B3, respectively.

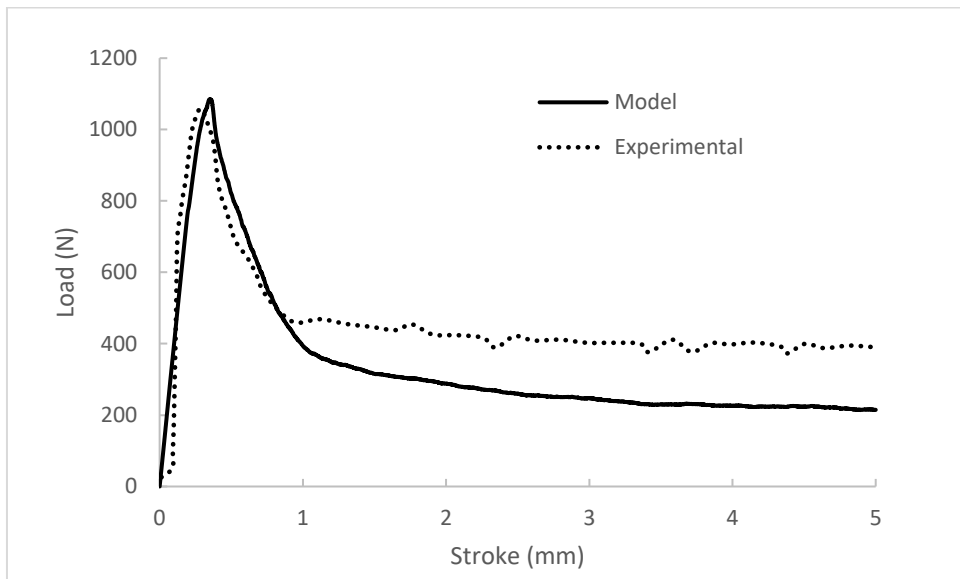


Figure 20 - Predicted vs Experimental Load Curves - Experiment A3

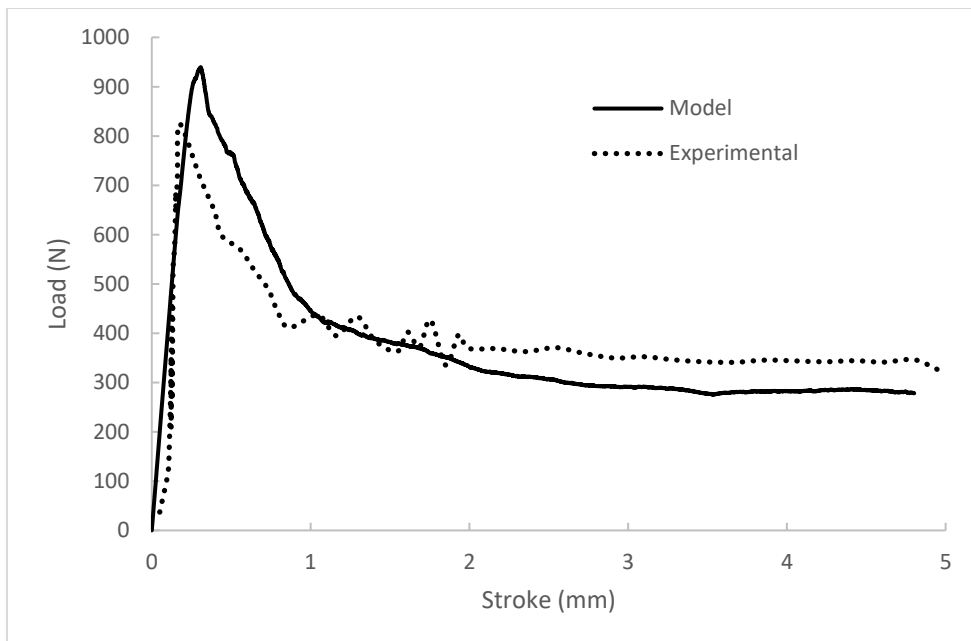
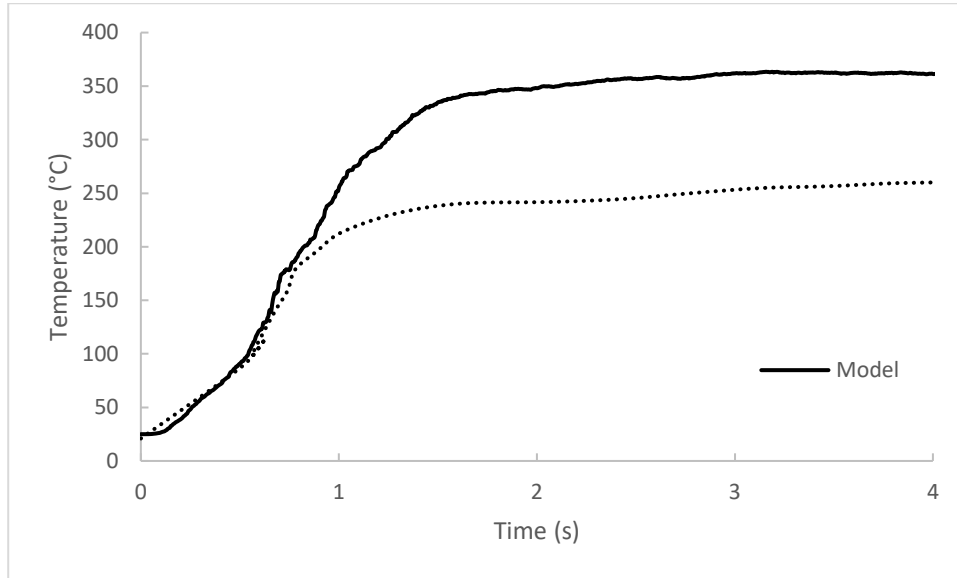
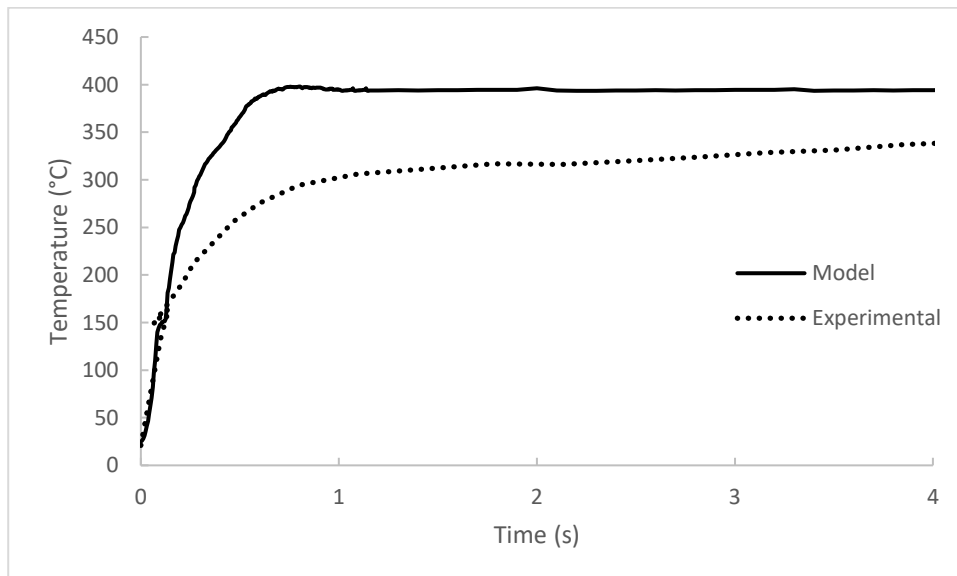


Figure 21 - Predicted vs Experimental Load Curves - Experiment B3



*Figure 22 - Predicted vs Experimental Thermal Profiles - Experiment A3*



*Figure 23 - Predicted vs Experimental Thermal Profiles - Experiment B3*

Figures 22 and 23 show the thermal profiles at the weld interface for A3 and B3. The discrepancy between experimental and simulated results is explained by the fact that the model shows the temperature at the welding interface, whereas the experimental data shows the temperature at a certain distance away from the interface. Hamade et al. (2019) use K-type thermocouples to measure the temperature profiles. These thermocouples are

not placed at the interface so that they won't get damaged from the deformation. The temperature gradient is very large in the region around the weld interface, so it is reasonable to have such a difference between the predicted and experimental values.

#### 3.2.9.2 Process Characteristics

It is widely believed that process optimization is directly linked to the employment of statistics to determine the optimum conditions. Statistics is absolutely needed, but first, the process should be well understood.

RFW experiences steep temperature gradients and extreme levels of deformation over a narrow weld region (Fu et al., 2003; Grant et al., 2009). This has a significant impact on the joint strength, flash formation and heat affected zone (Maalekian et al., 2008; Mohammed et al., 2009). In other words, the mechanical and thermal properties experience very fast changes which makes the process interactions very complex. The FE model results for experiment A3 will be used to better understand the FW process.

#### *Temperature Distribution*

The interface temperature increases rapidly from room temperature to about 256°C within 1 s (figure 22). This high gradient results from the rapid release of energy and low thermal conductivity of polyethylene, and leads to a narrow heat affected zone, which is preferable to minimize the variation in HDPE properties (Mohammed et al., 2009).

As the friction time increases, the friction and plastic deformation generate heat which gets carried away into the pipe through conduction. Therefore, the heated region expands away from the weld interface. Figure 24 illustrates the deformation, temperature evolution and HAZ size after 0.5, 1, 3.5 and 7.5 seconds of friction. Figure 25 is a representation of the weld in 3D.

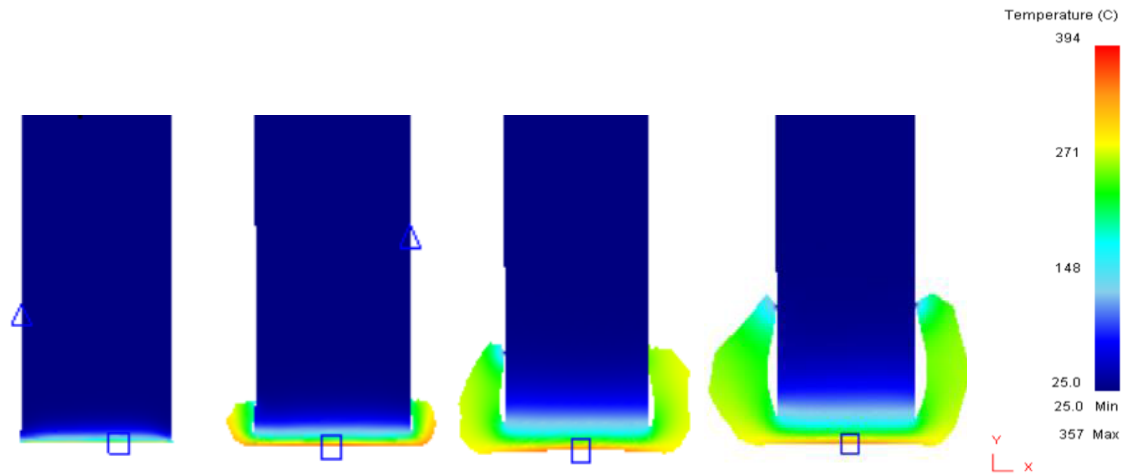


Figure 24 - Deformation and Temperature Evolution at friction time 0.5, 1, 3.5 and 7.5 sec, respectively

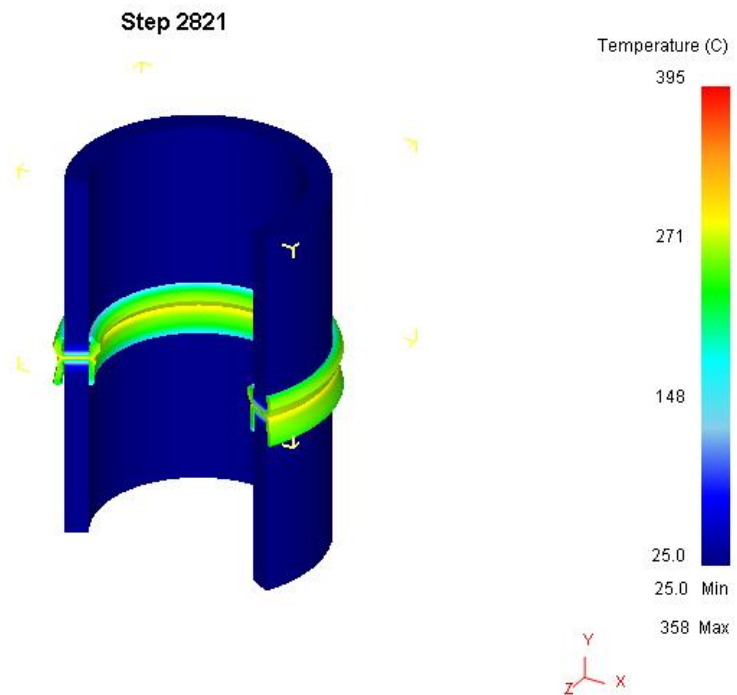
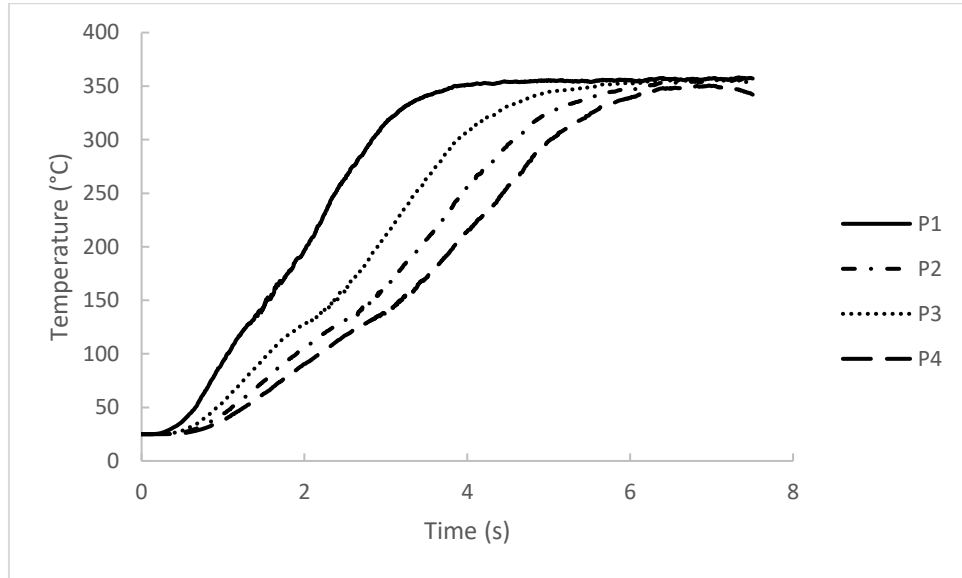


Figure 25 - 3D representation of the welded pipe

After 2 s, the temperature at the interface reaches a steady level of 350°C, due to a thermal balance between the heat generated at the interface and the heat dissipated through the flash. (W. Li & Wang, 2011; F. F. Wang et al., 2014; L. Wang et al., 2005; L. W. Zhang et al., 2007).





*Figure 26 - Thermal History at the Weld Interface*

The FE model can be used to track the temperature evolution at the weld interface. Figure 26 shows the thermal history of four points located at the friction interface (P1 (28.6 ,52.5); P2 (29.6, 52.5); P3(30.6 ,52.5); P4(31.6 ,52.5)). Each point undergoes a different thermal evolution which proves that the heat generation at the weld interface is not uniform. However, all the points at the weld interface reach the same temperature plateau.

### *Mechanical Deformation*

The high temperatures and axial load result in plastic deformation of the material which will eventually extrude outwards forming a flash (American Welding Society, 1983). Axial shortening or upset is the global shortening of the pipes that results from flash formation (Madhavan et al., 2011; Q. Z. Zhang et al., 2006).

At the start of welding, the heat input is not sufficient to cause plastic deformation, so there is almost no axial shortening (W. Li & Wang, 2011; F. F. Wang et al., 2014; L. Yang, 2010). The material deforms elastically at first, then shortens quickly (F. F. Wang et

al., 2014). The flash is asymmetric because the linear velocity along the radial direction is not uniform, which results in nonuniform heat generation and nonuniform material extrusion (Fu et al., 2003; F. F. Wang et al., 2014). In addition, when the rotational speed increases, the frictional heat input to the joint increases (Chander et al., 2012), leading to an increase in the amount of deformed and ejected thermoplastic. At these high rotational speeds, the flash symmetry on the inner and outer sides is lost (Palanivel et al., 2017).

The flash and HAZ are some of the key features of a high-quality weld. The HAZ is the region of the base material which has undergone a change in its properties due to the extensive heat input rates during welding (C. Bennett, 2015). According to Madhavan et al. (2011), a limited HAZ size is one of the key features of a good quality friction weld, because it is desirable to have a joint with the least alteration in the base material properties. Therefore, the smaller the HAZ size is, the better. HDPE has a low thermal conductivity, which leads to a restriction of heat conduction over extended distances (Sheikh-Ahmad et al., 2019). In addition, the welded specimen is a pipe, meaning that the heat dissipates on both the outside and inside. Both of these features prevent the formation of a wide HAZ (Palanivel et al., 2017).

Self-cleaning is also one of the key features for a high-quality weld. The initial contact interface contains contaminants such as oxide debris and oily residues, which might cause weak joints or unbonded regions in the weld if not removed (W. Li & Wang, 2011; Madhavan et al., 2011). Therefore, it is critical that a high proportion of the material originally present at the weld interface be expelled as flash, to guarantee that the weld interface is free of foreign impurities. Any remaining material that is not expelled as flash should be dispersed through the bulk of the material (Madhavan et al., 2011; L. Wang et al., 2005). Depending on the pipe wall thickness, a minimum upset is thus necessary to

expel contaminants. The fact that RFW does not include any filler material also guarantees the integrity of the welded joint (Grant et al., 2009).

The FE model can be used to track the flow of material and find out if there is sufficient self-cleaning. Point tracking was performed on 7 measurement points along the weld interface. Figure 27 indicates that at low level of upset (0.88 mm), much of the previous weld surface is expelled as flash because of the steep temperature gradient in the HAZ. This shows that the weld is sufficiently self-cleaned.



*Figure 27 - Point-tracking of weld interface*

The numerical model was validated based in experiments in the literature, and was sufficient to predict the peak load, peak torque, general process behavior and temperature evolution. Therefore, it is numerically efficient considering the various study limitations and assumptions. The developed model has a limited yet predictive capability, that is sufficient to study the effect of process input parameters on the mechanical and thermal properties of the RFW process.

# CHAPTER FOUR

## DESIGN OF EXPERIMENT: TAGUCHI

### 4.1 Definition and Advantages

Now that the process is well understood, parameter optimization can be performed. To identify the optimum RFW parameters, a strategically designed experiment is used. Design of experiments (DOE) is a strategic methodology that allows the investigation of the relationship between factors and responses to solve problems. Factors are the process input variables, and responses are the process output variables. DOE is a set of structured experiments that aim to collect data and make discoveries. Figure 28 shows the intentional variation “X” that is introduced in the process to measure the responses “Y” while controlling unintentional variation.

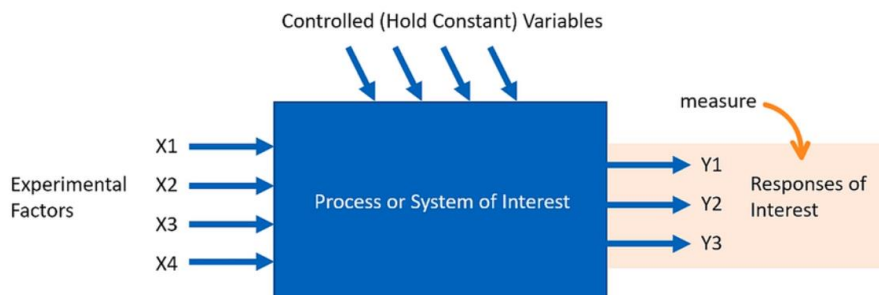


*Figure 28 - Designed experiment*

Designed experiments are better than trial and error and one-factor-at-a-time experiments because they allow an understanding of the relationships and interactions among input variables, require fewer experiments thus are less time consuming, and produce a statistical model that predicts the response as a function of input variables and their combined effect. The objective of a designed experiment is the reduction of the number of experiments required to determine the optimum parameters (Bilici et al., 2011; Wolf et al., 2013).

## 4.2 DOE Steps and Design Generation

DOE requires planning because it includes a set of steps. The steps taken in this study are:

### *1 – Defining the problem and the objectives*

The problem tackled in this study is the lack of optimal parameters that result in a good quality rotary friction weld of HDPE. Therefore, the objective is to find settings for these parameters that lead to a good quality weld with the least power consumption.

### *2 – Identifying the response variable or variables*

The response variable selected in this investigation is power consumption. According to Hodge (1965), the power required for FW is 10% that of butt welding. According to Gel'dman & Sander (1959), this value is 10-25%. In the study of Hamade et al. (2019), the power consumption of RFW ranged between 6.25 to 13.3% of that of butt fusion welding of HDPE pipes. With the use of optimized parameters, the power consumption will be even lower than that. This proves one of the main advantages of RFW when compared to butt fusion welding, and that is a reduced power consumption thus a more sustainable and environmentally friendly manufacturing process.

The power consumption will be calculated as:

$$P (W) = Torque (N.m) \times Rotational\ speed \left(\frac{rad}{sec}\right) \quad (9)$$

The torque in equation 9 refers to the peak torque that the process experiences. The variation of the torque is similar to that of the load i.e., the torque peaks at the start of the process before reaching a stagnant level. The developed model succeeds in the prediction of the peak torque, which is why the latter is chosen for the calculation of the power consumption. The calculated power will be an overestimation of the actual value but is a relative representation of the power consumption variation when the process parameters

vary. In other words, the power consumption calculated using equation 9 will serve the purpose of the optimization process.

### 3 – Identifying the factors and factor levels

The important factors that affect the process of RFW have been identified through the literature, and are the feed rate, rotational velocity, and friction time (W. Li et al., 2016; Maalekian, 2007; Uday et al., 2010).

There are more parameters that affect the process such as forging force, forging time, and burn-off rate (rate of upset during phase of constant upset rate). However, this study will only be limited to three factors, and the forging stage is not taken into account.

The selected factor levels are three and are shown in table 7.

*Table 7 - Factors and factor levels*

Factor	Code	Level			Unit
		1	2	3	
Rotary Speed	A	800	1012	1224	RPM
Feed rate	B	20	30	40	mm/min
Friction time	C	6	7.5	9	sec

### 4 – Identifying constraints and limitations

DOE limitations include the model capabilities: the test matrix is run using the FE model that is developed, meaning that the results will be affected by the assumptions and limitations of the model

### 5 – Generating the design

Taguchi method is selected to generate the experimental design. The runs will then be performed using the developed FE model. Taguchi methods are statistical methods built to enhance the quality of manufactured products, engineering processes, marketing and advertising, and many more (Karna & Sahai, 2012). The aim is to optimize the design parameters and lead to a robust system response. In other words, Taguchi methods focus

on determining the factor levels yielding the best settings of a performance measure with minimum variation. The Taguchi design has been proven to be a robust and simple methodology for the optimization of welding input parameters (Juang & Tarn, 2002). It is a fractional factorial design, meaning that it significantly decreases the time and cost associated with a designed experiment. For a 3-factor 3-level design, a full factorial design which takes into account all the combinations of factor levels, requires 27 experiments. Taguchi, however, only requires 9 experiments, as will be discussed later in this section.

The approach used in this study is based on Taguchi method. The Signal-Noise ratio (S/N) and Analysis of variance (ANOVA) are used to study the effect of control variables on the welding process and investigate the relationships between factors and response.

The Signal-Noise ratio is the quality characteristic in Taguchi, that should be maximized to obtain the best performance (Hafeez et al., 2002). The signal is a representation of the desired values for the output characteristic, and the noise is a representation of the undesired values, meaning that the S/N ratio is the ratio of the mean to standard deviation (Bilici et al., 2011; El-Hadek, 2014). It measures the deviation of the quality characteristic from the desired value.

There are 3 scenarios for the Signal-Noise ratio: the larger the better, the smaller the better, and the nominal the best. As previously mentioned, the lower the power consumption, the better. Therefore, the smaller the better is selected for the calculation of the S/N ratio.

$$\frac{S}{N} = -10 \log\left(\frac{1}{n} \sum_i Y_i^2\right) \quad (10)$$

where n is the number of observations in the i<sup>th</sup> trial, and Y is the corresponding parameter being optimized.

Taguchi provides orthogonal arrays (OA) which are sets or matrices of experiments that help in generating the optimum results. According to Montgomery (2021), the employment of OA allows the estimation of a maximum number of main effects from a minimum number of experiments. The appropriate OA is sufficient to study the effects of parameters on the response variable.

For a three factor and three level design, L9 is the suggested orthogonal array based on Taguchi method. It has 8 degrees of freedom (DOF): each factor is assigned 2 DOF and the remaining 2 DOF are assigned to the error. Tables 8 illustrates the coded and uncoded designs.

*Table 8 - Taguchi design*

Standard Order	Coded Design			Uncoded Design		
	A	B	C	A	B	C
1	1	1	1	800	20	6
2	1	2	2	800	30	7.5
3	1	3	3	800	40	9
4	2	1	2	1012	20	7.5
5	2	2	3	1012	30	9
6	2	3	1	1012	40	6
7	3	1	3	1224	20	9
8	3	2	1	1224	30	6
9	3	3	2	1224	40	7.5

After the steps mentioned, the model runs should be performed, the data analyzed, and a confirmation run conducted. Then, conclusions about the process optimization are drawn. These will be discussed in chapters 5 and 6.



# CHAPTER FIVE

## OPTIMIZATION RESULTS & DISCUSSION

### 5.1 Designed Experiment Results

Table 9 shows the maximum force, maximum torque and maximum temperature reached during the different experiments in the test matrix. As the axial velocity increases, the axial pressure increases (Tappe & Potente, 1989). As the rotational speed increases or the axial velocity decreases, the peak interface temperature increases. This is in line with the results obtained by Tappe & Potente (1989). The intensity of heat generation increases with rotational speed (W. Li et al., 2016). According to Crawford & Tam (1981), the heat generation is proportional to the rotational speed at a fixed pressure. According to W. Li & Wang (2011), the interface reaches a stable temperature faster when the rotational speed is increased, which leads to a quick start of material extrusion. For example, material extrusion starts at 1, 0.86 and 0.78 sec for model runs 1, 4 and 7, respectively. This also results in a decrease in peak load. In other words, when the relative velocity between the pipes increases, more friction heat is generated thus more material is plasticized and a lower force is required to eject it out as flash. This is shown in the peak load values reached in the test matrix.

Similar to the work of Stokes & Poslinski (1995), the torque decreases at high rotational velocities and low pressures. The power consumption is determined by the torque and rotational speed. Therefore, at a constant rotational speed, the torque is proportional to the applied pressure, thus the power input is proportional to the applied pressure (W. Li et al., 2016).

*Table 9 - Maximum force, torque, and temperature of the L9 test matrix*

<b>Experiment</b>	<b>Maximum force (N)</b>	<b>Maximum torque (N.mm)</b>	<b>Maximum temperature (°C)</b>
1	1275	7416	303
2	1800	8629	286
3	1913	9789	280
4	1017	6182	343
5	1144	7628	335
6	1206	8635	318
7	892	5454	395
8	1026	6733	389
9	1084	7889	363

## **5.2 Analysis of signal to noise ratio**

Table 10 shows the model results for the power consumption and the corresponding S/N ratio.

*Table 10 – Power consumption and signal to noise ratios*

<b>Experiment</b>	<b>Power (W)</b>	<b>S/N</b>
1	621	-55.868
2	719	-57.133
3	820	-58.280
4	655	-56.329
5	808	-58.155
6	915	-59.231
7	698	-56.879
8	861	-58.709
9	1009	-60.085

Since the matrix design is orthogonal, the effect of each welding parameter at different levels can be separated. For instance, the mean S/N ratio for feed rate at levels 1 can be calculated by taking the average of the S/N ratios of experiments 1, 4 and 7. The results are illustrated in table 11, which shows the mean S/N ratios at each level.

Table 11 - Response table for signal to noise ratios (smaller is better)

Level	Rotational speed	Feed Rate	Friction Time
1	-57.09	-56.36	-57.94
2	-57.91	-58.00	-57.85
3	-58.56	-59.20	-57.77
Delta	1.46	2.84	0.16
Rank	2	1	3

Table 11 shows that the feed rate is the most influential parameter on the power consumed, while friction time is the least. The optimum combination of input parameters is level 1 of rotational speed, level 1 of feed rate and level 3 of friction time. These optimum parameters are graphically represented in the S/N response graph (figure 29). The dashed line is a representation of the total mean S/N ratio of the nine experiments.

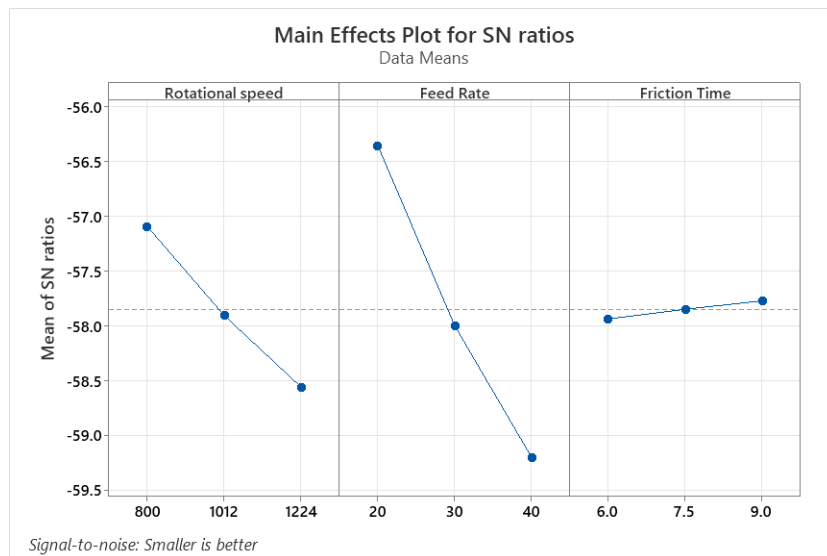


Figure 29 - Main effects plot for S/N ratios

Figure 30 is the main effects plot for means. It shows that the power consumption increases as the rotational speed and feed rate increase. Friction time seems to have very little effect on the power consumed (figures 29 and 30).

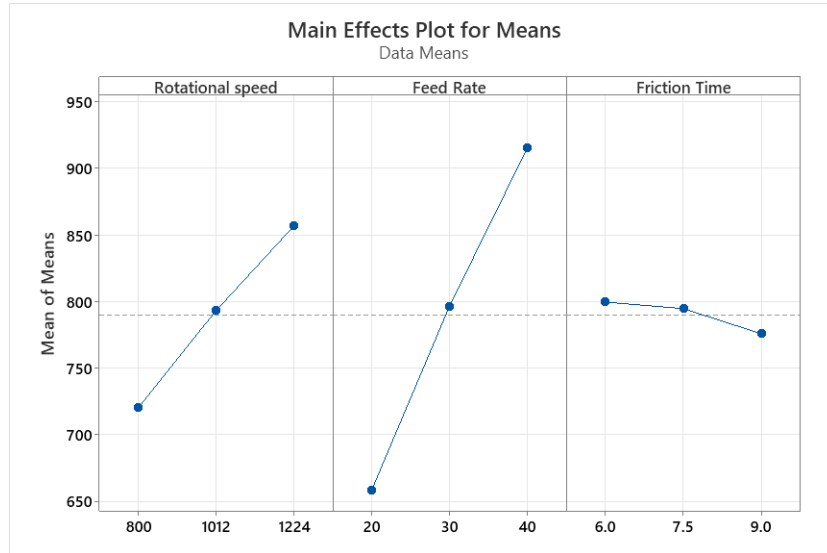


Figure 30 - Main effects plot for means

### 5.3 Analysis of Variance (ANOVA)

Analysis of variance (ANOVA) can be used to identify the relative importance of process parameters on the power consumed, in addition to the S/N ratio. Taguchi method does not allow the determination of the influence of each parameter on the process, but ANOVA allows the determination of the statistically significant parameter and the percentage contribution of each (Bilici et al., 2011; Gopalsamy et al., 2009; Kalsi & Sharma, 2011; Wahyudin et al., 2018). Therefore, ANOVA enables data based decision making (Wahyudin et al., 2018).

Table 12 illustrates the results of ANOVA for S/N ratios. The total sum of squared deviations (SST) is split into two components, the sum of squared deviations (SSD) and the sum of squared error (SSE), and is calculated as:

$$SST = \sum_{i=1}^n (\eta_i - \eta_m)^2 \quad (11)$$

Where  $\eta_i$  is the S/N ratio for the  $i$ th experiment,  $\eta_m$  is the total S/N ratio, and  $n$  is the total number of experiments.

The mean square is the ratio of sum of squared deviations (SSD) to the degrees of freedom. This is used to calculate the F value of Fisher test. ANOVA tests whether the

factor has an influence on the response by evaluating the F value of fisher test, or the P-value. The F value is equal to the mean of squared deviations divided by the mean of squared error. The factor is considered statistically significant when  $F > 4$  (W. H. Yang & Tarnq, 1998). The P-value is the probability that the null hypothesis is true. A small P-value means that the probability that the outcome occurs by chance is small. The P-value is measured against a threshold called the significance level  $\alpha$ . The common  $\alpha$  value is 0.05, and it is linked to a confidence level of 95%. This means that the same result is achieved 95% of the time if the experiment is performed again and again (Sheikh-Ahmad et al., 2019).

According to the ANOVA results in table 12, the feed rate and rotational speed are found to be important for the power consumed, because their F-value is higher than 4 and their P-value is lower than 0.05, meaning that they are statistically significant. It is found that the feed rate is the dominant factor on the power consumed, whereas the friction time, whose p-value equals 0.79, doesn't have a significant effect.

*Table 12 - Analysis of variance for S/N ratios*

Source	Degrees of Freedom	Sum of Squares	Mean Square	F	P	Contribution %
Rotational speed	2	3.2279	1.61395	21.08	0.045	20.67
Feed Rate	2	12.1951	6.09753	79.66	0.012	78.09
Friction Time	2	0.0407	0.02035	0.27	0.790	0.26
Residual Error	2	0.1531	0.07655			0.98
Total	8	15.6167				

The percentage contribution is the ratio of the Sum of Squares for the factor to the total

Sum of squares:

$$\text{Contribution \%} = \frac{\text{Sum of Squares}_f}{\text{Sum of Squares}_{total}} \quad (12)$$

The results are shown in the last column in table 12. The feed rate is the most influential parameter with a contribution of 78%, the rotational speed ranks second with a

contribution of almost 21%, and the friction time has very little influence with a contribution of 0.26%. Therefore, the conclusions obtained by both Taguchi and ANOVA match closely.

## 5.4 Regression Model

A linear regression analysis was performed to develop a predictive model for the dependent variable, which is the power consumed, as a function of rotational speed, feed rate and friction time. The predictive equation has a high  $R^2$  value (0.97) and shown in equation 13.

$$\text{Power (W)} = 138.7 + 0.3217 \text{ Rotational speed} + 12.842 \text{ Feed rate} - 7.94 \text{ Friction time} \quad (13)$$

Figure 31 shows the normal probability plot, which is used to investigate the significance of the model coefficients. The residuals fall close to the straight line, meaning that the residual errors are normally distributed, and the model coefficients are significant.

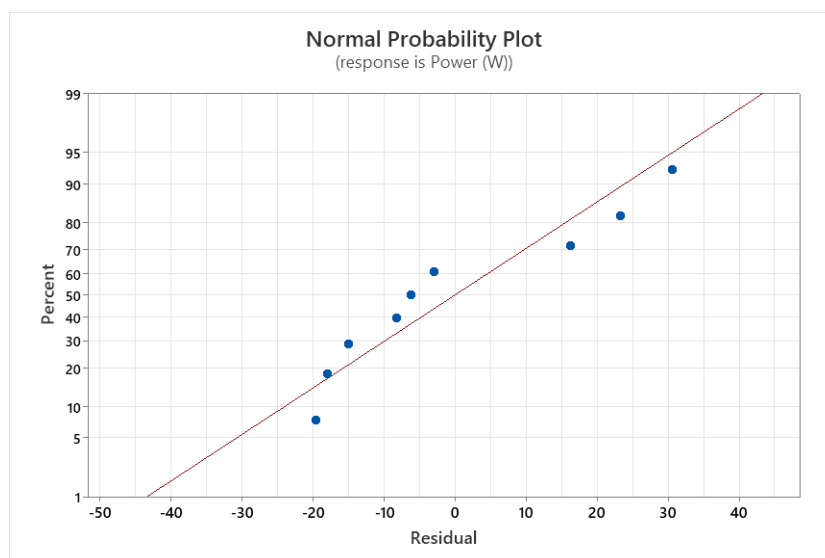


Figure 31 - Normal probability plot

## 5.5 Confirmation Test

After the determination of the optimum input parameters using the Taguchi design, their corresponding response is predicted and verified using the model. This is done to verify that the selected quality characteristic is improved using the optimum set of parameters (Mazumdar & Hoa, 1995).

The predicted S/N ratio denoted as  $\hat{\eta}$  is calculated as:

$$\hat{\eta} = \eta_m + \sum_{i=0}^o (\bar{\eta}_i - \bar{\eta}_m) \quad (14)$$

where  $\eta_m$  is the total mean S/N ratio,  $\bar{\eta}_i$  is the mean S/N ratio at the optimum level, and  $o$  is the number of factors.

Based on the S/N and ANOVA analysis, the optimum parameters are A1B1C3. This combination is input to the FE model and the resulting power consumed and S/N ratio are shown in table 13, along with the predicted values. The model S/N ratio was calculated using equation 10 and the predicted power consumed was calculated using the regression model. There is a good agreement between the predicted and actual power consumed values, with an error of 5.7%. The predicted and model S/N ratios are also very close with a 0.5% error. This shows that validity of the Taguchi design and analysis.

*Table 13 - Confirmation test results*

	Prediction	Model
<b>Power Consumed (W)</b>	581.44	617.08
<b>S/N Ratio</b>	-55.5195	-55.8057

As discussed in Chapter 4, the interface temperature and self-cleaning are important factors in determining the quality of the weld. In terms of temperature, it is desirable that the interface temperature be as low as possible because it has a direct effect on material deformation and the formation of the HAZ, thus on the mechanical properties of the welded pipes (Alves et al., 2012; W. Li et al., 2016). In the optimum experiment,

the maximum temperature reached during the process is 300°C. Among the 9 experiments performed, the lowest temperature is 280°C (experiment 3) and the highest is 396°C (experiment 7). The temperature in the optimum design might not be the lowest but is on the lower end of the scale. As discussed in section 5.1, the rotational speed has a large influence on the heat generation and stable weld interface temperature. This means that a rotational speed of 800 rpm is a favorable to reduce the interface temperature.

As for self-cleaning, point-tracking was performed at the weld interface in the model, and the original interface is extruded out after 2.6 sec of friction time and 0.87 mm of upset. Therefore, the final weld is free of surface contaminants.



## CHAPTER SIX

### CONCLUSION, LIMITATIONS & FUTURE WORK

The selection of welding parameters has a profound effect on heat generation, material flow and joint structural integrity during the process of rotary friction welding. The developed 2D axisymmetric model was capable of predicting the thermal and mechanical behavior of HDPE and provide results that were comparable with experimental data reported in the literature. The developed model was used to predict the optimum parameters to be used in a rotary friction welding of a pipe of specific geometry. The Taguchi method showed that the optimum parameters for the friction welding of the 63 mm diameter pipe with 5.8 mm thickness were a rotational velocity of 800 rpm, a feed rate of 20 mm/min and a friction time of 9 sec. The optimized welding parameters yielded a good quality weld with minimum power consumption. This reduces greenhouse gas emissions and abide by the Paris Agreement which calls for a net zero Carbon goal by 2050 (United Nations, 2022). It also reduces the operational cost as the process doesn't require neither a skilled welder nor filler materials. In addition, the flow behavior of HDPE was successfully modelled using the Zerilli Armstrong model. This can be directly used in other studies that require the flow stress data of HDPE or can be extended to other thermoplastics which have a similar flow behavior.

Nevertheless, this study included multiple limitations. There was a lack of flow stress data for HDPE at the different temperature and strain rate ranges existing during RFW, which necessitated the various extrapolations. The optimal parameters are valid for the ranges of stresses, strains, strain rates, and temperatures that were used in the Zerilli Armstrong constitutive equation used in the study. To improve the accuracy of the model,

further flow stress data need to be collected for HDPE at different temperatures and strain rates to reduce the dependence on extrapolated data that was used in this study. Further improvements to the model accuracy could be achieved by conducting experimental tests to estimate the coefficient of friction in the process that was based on data collected from the literature. Future work should also include additional welding parameters such as the forging pressure and cooling time, and different pipe geometries to cover a wider range of applications. Despite these limitations, this work laid down the infrastructure and methodology needed for reaching the full potential of the optimization of process parameters of friction welding of HDPE pipes.

## REFERENCES

- Ahmet Z. Sahin, Bekir S. Yibas, M.Ahmed, and J.Nickel. Analysis of the friction welding process in relation to the welding of copper and steel bars. *Journal of Materials Processing Technology*, 82:127–136, 1998.
- Akbari Mousavi, S. A. A., & Kelishami, A. R. (2008). Experimental and numerical studies of the effects of process parameters in the continuous friction welding process. *Materials Science Forum*, 580–582, 335–338.  
<https://doi.org/10.4028/www.scientific.net/msf.580-582.335>
- Alfredo Campo, E. (2008). 3 Thermal Properties of Polymeric Materials. *Selection of Polymeric Materials*, 103–140. <https://doi.org/10.1016/B978-0-8155-1551-7.50005-X>
- Alves, E. P., Neto, F. P., An, C. Y., & da Silva, E. C. (2012). Experimental determination of temperature during rotary friction welding of AA1050 aluminum with AISI 304 stainless steel. *Journal of Aerospace Technology and Management*, 4(1), 61–68.  
<https://doi.org/10.5028/jatm.2012.04013211>
- Ammouri, A., Kheireddine, A. H., Lu, T., & Hamade, R. F. (2012). Model-based optimization of process parameters in the friction stir processing of AZ31b with adaptive cooling.
- Ammouri, A. H., & Hamade, R. (2014-a). Comparison of material flow stress models toward more realistic simulations of friction stir processes of Mg AZ31B. In *Advanced Materials Research* (Vol. 922, pp. 18-22). Trans Tech Publications Ltd.  
<https://doi.org/10.4028/www.scientific.net/AMR.922.18>
- Ammouri, A. H., & Hamade, R. F. (2014-b). On the selection of constitutive equation for modeling the friction stir processes of twin roll cast wrought AZ31B. *Materials & Design*, 57, 673-688. <https://doi.org/10.1016/j.matdes.2014.01.057>
- Ammouri, A. H., & Hamade, R. F. (2015, November). Toward an affordable automation scheme of friction stir processing. In *ASME International Mechanical Engineering Congress and Exposition* (Vol. 57359, p. V02AT02A056). American Society of

Mechanical Engineers. <https://doi.org/10.1115/IMECE2015-53314>

Ammouri, A. H., Kheireddine, A. H., Kridli, G. T., & Hamade, R. F. (2013, November). FEM optimization of process parameters and in-process cooling in the friction stir processing of magnesium alloy AZ31B. In ASME International Mechanical Engineering Congress and Exposition (Vol. 56185, p. V02AT02A079). American Society of Mechanical Engineers. <https://doi.org/10.1115/IMECE2013-62468>

Ammouri, A. H., Kridli, G., Ayoub, G., & Hamade, R. F. (2015). Relating grain size to the Zener-Hollomon parameter for twin-roll-cast AZ31B alloy refined by friction stir processing. *Journal of Materials Processing Technology*, 222, 301–306. <https://doi.org/10.1016/j.jmatprotec.2015.02.037>

Andrzej Sluzalec. Thermal effects in friction welding. *International Journal of mechanical science*, 32:467–478, 1990.

Balobanov, V., Verho, T., Heino, V., Ronkainen, H., & Pelto, J. (2021). Micromechanical performance of high-density polyethylene: Experimental and modeling approaches for HDPE and its alumina-nanocomposites. *Polymer Testing*, 93, 106936. <https://doi.org/10.1016/j.polymertesting.2020.106936>

Bennett, C. (2015). Finite element modelling of the inertia friction welding of a CrMoV alloy steel including the effects of solid-state phase transformations. *Journal of Manufacturing Processes*, 18, 84–91. <https://doi.org/10.1016/j.jmapro.2015.01.003>

Bennett, C. J., Attallah, M. M., Preuss, M., Shipway, P. H., Hyde, T. H., & Bray, S. (2013). Finite element modeling of the inertia friction welding of dissimilar high-strength steels. *Metallurgical and Materials Transactions A: Physical Metallurgy and Materials Science*, 44(11), 5054–5064. <https://doi.org/10.1007/s11661-013-1852-2>

Bennett, C. J., Hyde, T. H., & Shipway, P. H. (2011). A transient finite element analysis of thermoelastic effects during inertia friction welding. *Computational Materials Science*, 50(9), 2592–2598. <https://doi.org/10.1016/j.commatsci.2011.03.048>

Bennett, C. J., Hyde, T. H., & Williams, E. J. (2007). Modelling and simulation of the inertia friction welding of shafts. *Proceedings of the Institution of Mechanical*

*Engineers, Part L: Journal of Materials: Design and Applications*, 221(4), 275–284.  
<https://doi.org/10.1243/14644207JMDA154>

Bilici, M. K., Yüklér, A. I., & Kurtulmuş, M. (2011). The optimization of welding parameters for friction stir spot welding of high density polyethylene sheets. *Materials and Design*, 32(7), 4074–4079.  
<https://doi.org/10.1016/j.matdes.2011.03.014>

Bindal, T., Saxena, R. K., & Pandey, S. (2021). Investigating friction spin welding of thermoplastics in shear joint configuration. *SN Applied Sciences*, 3(2).  
<https://doi.org/10.1007/s42452-021-04217-z>

Blau, P. J. (2017). Friction, Lubrication, and Wear Technology. *Friction, Lubrication, and Wear Technology*, 18, 1879. <https://doi.org/10.31399/asm.hb.v18.9781627081924>

Bonds, R. W. (2000). Ductile iron pipe versus HDPE pipe. In *Plastics Engineering*.  
<http://www.dipra.org/pdf/DIPvsHDPE.pdf>

Briscoe, B. J., & Hutchings, I. M. (1976). Impact yielding of high density polyethylene. *Polymer*, 17(12), 1099–1102. [https://doi.org/10.1016/0032-3861\(76\)90013-6](https://doi.org/10.1016/0032-3861(76)90013-6)

Brown, E. N., Willms, R. B., Gray, G. T., Rae, P. J., Cady, C. M., Vecchio, K. S., Flowers, J., & Martinez, M. Y. (2007). Influence of molecular conformation on the constitutive response of polyethylene: A comparison of HDPE, UHMWPE, and PEX. *Experimental Mechanics*, 47(3), 381–393. <https://doi.org/10.1007/s11340-007-9045-9>

C.J.Cheng. Transient temperature distribution during friction welding of two similar materials in tubular form. *Welding Research Supplement*, pages 542–550, 1962.

Cai, W., Daehn, G., Vivek, A., Li, J., Khan, H., Mishra, R. S., & Komarasamy, M. (2019). A state-of-the-art review on solid-state metal joining. *Journal of Manufacturing Science and Engineering, Transactions of the ASME*, 141(3).  
<https://doi.org/10.1115/1.4041182>

Chander, G. S., Reddy, G. M., & Rao, A. V. (2012). Influence of Rotational Speed on Microstructure and Mechanical Properties of Dissimilar Metal AISI 304-AISI 4140 Continuous Drive Friction Welds. *Journal of Iron and Steel Research International*, 19(10), 64–73. [https://doi.org/10.1016/S1006-706X\(12\)60154-X](https://doi.org/10.1016/S1006-706X(12)60154-X)

Dawood, A. B., Butt, S. I., Hussain, G., Siddiqui, M. A., Maqsood, A., & Zhang, F. (2017). Thermal model of rotary friction welding for similar and dissimilar metals. *Metals*, 7(6). <https://doi.org/10.3390/met7060224>

D'Alvise, L., Massoni, E., & Walloe, S. J. (2002). Finite element modelling of the inertia friction welding process between dissimilar materials. *Journal of Materials Processing Technology*, 125–126, 387–391. [https://doi.org/10.1016/S0924-0136\(02\)00349-7](https://doi.org/10.1016/S0924-0136(02)00349-7)

DEFORM V11.0 Documentation.

Donohue, J. J. (American F. W. (2001). *The Friction Welding Advantage*. American Welding Society. <https://app.aws.org/wj/2001/05/0027/>

Drozdov, A. D., & Christiansen, J. de C. (2008). Thermo-viscoelastic and viscoplastic behavior of high-density polyethylene. *International Journal of Solids and Structures*, 45(14–15), 4274–4288. <https://doi.org/10.1016/j.ijsolstr.2008.03.008>

El-Hadek, M. A. (2009). Sequential transient numerical simulation of inertia friction welding process. *International Journal for Computational Methods in Engineering Science and Mechanics*, 10(3), 224–230. <https://doi.org/10.1080/15502280902795086>

El-Hadek, M. A. (2014). Numerical Simulation of the Inertia Friction Welding Process of Dissimilar Materials. *Metallurgical and Materials Transactions B: Process Metallurgy and Materials Processing Science*, 45(6), 2346–2356. <https://doi.org/10.1007/s11663-014-0148-2>

Fatemi, A., Mellot, S., Khosrovaneh, A., & Buehler, C. (2014). Tensile and fatigue

behaviors of two thermoplastics including strain rate, temperature, and mean stress effects. *SAE Technical Papers, 1*. <https://doi.org/10.4271/2014-01-0901>

Fu, L.; Duan, L. Y. (1998) The coupled deformation and heat flow analysis by finite element method during friction welding. *Welding Journal*, Volume 77, 202-207.

Fu, L., Duan, L. Y., & Du, S. G. (2003). Numerical Simulation of Inertia Friction Welding Process by Finite Element Method. *Welding Journal, March 2003*, 65–70.

Gel'dman, A. S., and Sander, M. P. 1959. Power and heating in the friction welding of thick-walled steel pipes. *Svarochnoe Proizvodstvo (Welding Production)*: 53–61

Gopalsamy, B. M., Mondal, B., & Ghosh, S. (2009). Taguchi method and anova: An approach for process parameters optimization of hard machining while machining hardened steel. *Journal of Scientific and Industrial Research*, 68(8), 686–695.

Grant, B., Preuss, M., Withers, P. J., Baxter, G., & Rowlson, M. (2009). Finite element process modelling of inertia friction welding advanced nickel-based superalloy. *Materials Science and Engineering A*, 513–514(C), 366–375.  
<https://doi.org/10.1016/j.msea.2009.02.005>

Grewell, D., & Benatar, A. (2007). Welding of plastics: Fundamentals and new developments. *International Polymer Processing*, 22(1), 43–60.  
<https://doi.org/10.3139/217.0051>

Hafeez, K., Rowlands, H., Kanji, G., & Iqbal, S. (2002). Design optimization using ANOVA. *Journal of Applied Statistics*, 29(6), 895–906.  
<https://doi.org/10.1080/02664760220136203>

Hamade, R. F., Andari, T. R., Ammouri, A. H., & Jawahir, I. S. (2019). Rotary friction welding versus fusion butt welding of plastic pipes – Feasibility and energy perspective. *Procedia Manufacturing*, 33, 693–700.  
<https://doi.org/10.1016/j.promfg.2019.04.087>

Hasegawa, M., Asada, T., & Ozawa, Y. (2002). Study of friction welding of polyethylene. *Welding International*, 16(7), 537–543. <https://doi.org/10.1080/09507110209549572>

Hasegawa, M., Asada, T., Ozawa, Y., & Taki, N. (1998). Study of friction welding of polyethylene pipes. *Welding International*, 12(9), 682–687. <https://doi.org/10.1080/09507119809452035>

Hassan, G. I., & Khdir, Y. K. (2018). Effect of Rotary Friction Welding Parameters on the Mechanical Behavior ABS/PE Polymers. *Academic Journal of Nawroz University*, 7(4), 104. <https://doi.org/10.25007/ajnu.v7n4a278>

Jenney, C. L., & O'Brien, A. (1991). Welding Handbook\_Volume 1\_WELDING SCIENCE AND TECHNOLOGY. *American Welding Society*, 1, 982.

Juang, S. C., & Tarng, Y. S. (2002). Process parameter selection for optimizing the weld pool geometry in the tungsten inert gas welding of stainless steel. *Journal of Materials Processing Technology*, 122(1), 33–37. [https://doi.org/10.1016/S0924-0136\(02\)00021-3](https://doi.org/10.1016/S0924-0136(02)00021-3)

K.Lee, A.Samant, W.T.Wu, and S.Srivatsa. Finite element modelling of the inertia welding process. In *NUMIFORM, Toyohashi, Japan, 2001*

Kalsi, N. S., & Sharma, V. S. (2011). A statistical analysis of rotary friction welding of steel with varying carbon in workpieces. *International Journal of Advanced Manufacturing Technology*, 57(9–12), 957–967. <https://doi.org/10.1007/s00170-011-3361-z>

Karna, S. K., & Sahai, R. (2012). An overview on Taguchi Method. *International Journal of Engineering and Mathematical Sciences*, 1, 11–18.

Khan, I. A. (2011). *Experimental and numerical investigation on the friction welding process*. 411525, 411525.

Kouta, H., Elsanabary, S., Elhadek, M., & Elkaseer, A. (2020). FE Simulation of Inertia Friction Welding of Similar PVC-PVC and PA6-PA6 Hollow Cylinders for Process



Optimization FE Simulation of Inertia Friction Welding of Similar PVC-PVC and PA6- PA6 Hollow Cylinders for Process Optimization. *Sylwan*, February.

Kukureka, S. N., & Hutchings, I. M. (1981). Measurement of the mechanical properties of polymers at high strain rates by Taylor impact. *Blazynski, T.Z. (Ed.) Proc. 7th Int. Conf. on High Energy Rate Fabrication, University of Leeds*, 29–38.

Lamri, A., Shirinbayan, M., Pereira, M., Truffault, L., Fitoussi, J., Lamouri, S., Bakir, F., & Tcharkhtchi, A. (2020). Effects of strain rate and temperature on the mechanical behavior of high-density polyethylene. *Journal of Applied Polymer Science*, 137(23). <https://doi.org/10.1002/app.48778>

Li, S., & Qi, K. (2014). *The Mechanical and Fracture Property of HDPE-Experiment Result Combined with Simulation* [Blekinge Institute of Technology Karlskrona, Sweden]. <https://www.diva-portal.org/smash/get/diva2:830762/FULLTEXT01.pdf>

Li, W., Vairis, A., Preuss, M., & Ma, T. (2016). Linear and rotary friction welding review. *International Materials Reviews*, 61(2), 71–100. <https://doi.org/10.1080/09506608.2015.1109214>

Li, W., & Wang, F. (2011). Modeling of continuous drive friction welding of mild steel. *Materials Science and Engineering A*, 528(18), 5921–5926. <https://doi.org/10.1016/j.msea.2011.04.001>

Lin, C. Bin, Wu, L. C., & Chen, Y. Y. (2004). Friction welding of similar materials: Polypropylene, high-density polyethylene, and nylon-6. *Journal of Applied Polymer Science*, 91(5), 2771–2780. <https://doi.org/10.1002/app.13459>

Lin, C. B., & Wu, L. C. (2000). Friction welding of similar and dissimilar materials: PMMA and PVC. *Polymer Engineering and Science*, 40(8), 1931–1941. <https://doi.org/10.1002/pen.11325>

Maalekian, M. (2007). Friction welding - Critical assessment of literature. *Science and Technology of Welding and Joining*, 12(8), 738–759.

<https://doi.org/10.1179/174329307X249333>

Maalekian, M., Kozeschnik, E., Brantner, H. P., & Cerjak, H. (2008). Comparative analysis of heat generation in friction welding of steel bars. *Acta Materialia*, 56(12), 2843–2855. <https://doi.org/10.1016/j.actamat.2008.02.016>

MADEN, H., & ÇETİNKAYA, K. (2021). Joining Analysis of Polypropylene Parts in Rotary Friction Welding Process and Developing of Joints Profile. *Journal of Polytechnic*, 0900(3), 1263–1273. <https://doi.org/10.2339/politeknik.824615>

Madhavan, V., D'Alvise, L., Lepot, I., Vatovec, A., & Nunn, M. (2011). Optimisation of Welding Parameters for the Continuous Drive Rotary Friction Welding Process on Simple Tubular Geometries for Steel. *64th Annual Assembly & International Conference of the International Institute of Welding*, July. <https://doi.org/10.13140/2.1.2134.6885>

Mazumdar, S. K., & Hoa, S. V. (1995). Application of Taguchi method for process enhancement of on-line consolidation technique. *Composites*, 26(9), 669–673. [https://doi.org/10.1016/0010-4361\(95\)98916-9](https://doi.org/10.1016/0010-4361(95)98916-9)

McKelvey, D., Menary, G. H., Martin, P. J., & Yan, S. (2018). Large strain, high rate semi-solid deformation of high density polyethylene at elevated temperatures. *Polymer Engineering and Science*, 58(9), 1516–1522. <https://doi.org/10.1002/pen.24723>

Merah, N., Saghir, F., Khan, Z., & Bazoune, A. (2006). Effect of temperature on tensile properties of HDPE pipe material. *Plastics, Rubber and Composites*, 35(5), 226–230. <https://doi.org/10.1179/174328906X103178>

Meyer, H. W. (2006). A Modified Zerilli-Armstrong Constitutive Model Describing the Strength and Localizing Behavior of Ti-6Al-4V. *Materials Research*, 1–29.

Milisavljević, J., Petrović, E., Ćirić, I., Mančić, M., Marković, D., & Dordević, M. (2012). Tensile testing for different types of polymers. *29th DANUBIA-ADRIA Symposium on Advances in Experimental Mechanics, DAS 2012, September*, 266–269.

- Moal, A., & Massoni, E. (1995). Finite element simulation of the inertia. *Engineering Computations*, 12, 6.
- Mohammed, M. B., Bennett, C. J., Hyde, T. H., & Williams, E. J. (2009). The evaluation of coefficient of friction for representative and predictive finite element modelling of the inertia friction welding. *ASME Turbo Expo*, 1–9.
- Mohammed, M. B., Bennett, C. J., Shipway, P. H., & Hyde, T. H. (2010). Optimization of heat transfer in the finite element process modelling of inertia friction welding of SCMV and AerMet 100. *WIT Transactions on Engineering Sciences*, 68, 253–265. <https://doi.org/10.2495/HT100221>
- Montgomery, D. C. (2021). *Design and analysis of Experiments*. John Wiley & Sons, Inc.
- Mortazavian, S., & Fatemi, A. (2015). Tensile and fatigue behaviors of polymers for automotive applications. *Materialwissenschaft Und Werkstofftechnik*, 46(2), 204–213. <https://doi.org/10.1002/mawe.201400376>
- Mousavi, S. A. A. A., & Kelishami, A. R. (2008). Experimental and numerical analysis of the friction welding process for the 4340 steel and mild steel combinations. *Welding Journal (Miami, Fla)*, 87(7).
- Nguyen, T. C., & Weckman, D. C. (2006). A thermal and microstructure evolution model of direct-drive friction welding of plain carbon steel. *Metallurgical and Materials Transactions B: Process Metallurgy and Materials Processing Science*, 37(2), 275–292. <https://doi.org/10.1007/BF02693157>
- Palanivel, R., Laubscher, R. F., & Dinaharan, I. (2017). An investigation into the effect of friction welding parameters on tensile strength of titanium tubes by utilizing an empirical relationship. *Measurement: Journal of the International Measurement Confederation*, 98, 77–91. <https://doi.org/10.1016/j.measurement.2016.11.035>

- Plastics Pipe Institute (2019). Smooth-wall High-Density Polyethylene pipe systems. Retrieved December 2020, from <https://plasticpipe.org/>
- Potente, H., & Uebbing, M. (1997). Friction welding of polyamides. *Polymer Engineering and Science*, 37(4), 726–737. <https://doi.org/10.1002/pen.11716>
- R. J. Crawford, Y. T. (1981). Friction welding of plastics. *Journal of Materials Science*.
- Ringius, H., & Thorsell, C. (2017). *FE modeling of friction welding* [Chalmers University of Technology]. <http://publications.lib.chalmers.se/records/fulltext/242403/242403.pdf>
- Seli, H., Awang, M., Ismail, A. I. M., Rachman, E., & Ahmad, Z. A. (2013). Evaluation of properties and FEM model of the friction welded mild steel-Al6061-alumina. *Materials Research*, 16(2), 453–467. <https://doi.org/10.1590/S1516-14392012005000178>
- Sercer, M., & Raos, P. (n.d.). Joining of Plastics and Composites. *UNESCO -Encyclopedia of Life Support Systems (EOLSS)*, 36.
- Sheikh-Ahmad, J. Y., Ali, D. S., Deveci, S., Almaskari, F., & Jarrar, F. (2019). Friction stir welding of high density polyethylene—Carbon black composite. *Journal of Materials Processing Technology*, 264(September 2018), 402–413. <https://doi.org/10.1016/j.jmatprotec.2018.09.033>
- Shen, Y. (2012). *The Chemical and Mechanical Behaviors of Polymer / Reactive Metal Systems Under High Strain Rates* (Issue December). Georgia Institute of Technology.
- Siviour, C. R., Walley, S. M., Proud, W. G., & Field, J. E. (2005). The high strain rate compressive behaviour of polycarbonate and polyvinylidene difluoride. *Polymer*, 46(26), 12546–12555. <https://doi.org/10.1016/j.polymer.2005.10.109>
- Spalding, M. A., Kirkpatrick, D. E., & Hyun, K. S. (1993). Coefficients of dynamic friction for low density polyethylene. *Polymer Engineering & Science*, 33(7), 423–430. <https://doi.org/10.1002/pen.760330708>

- Stokes, V. K. (1988). Analysis of the friction (spin)-welding process for thermoplastics. *Journal of Materials Science*, 23(8), 2772–2785. <https://doi.org/10.1007/BF00547450>
- Stokes, V. K. (1989). Joining Methods for Plastics and Plastic Composites: An overview. *Polymer Engineering & Science*, 29(19), 1310–1324. <https://doi.org/https://doi.org/10.1002/pen.760291903>
- Stokes, V. K., & Poslinski, A. J. (1995). Effects of variable viscosity on the steady melting of thermoplastics during spin welding. *Polymer Engineering & Science*, 35(5), 441–459. <https://doi.org/10.1002/pen.760350510>
- Takasu, N. (2003). Friction welding of plastics. *Welding International*, 17(11), 856–859. <https://doi.org/10.1533/wint.2003.3198>
- Tappe, P., & Potente, H. (1989). New results on the spin welding of plastics. *Polymer Engineering & Science*, 29(23), 1655–1660. <https://doi.org/10.1002/pen.760292306>
- Tashkandi, M. A. (2021). Finite element modeling of continuous drive friction welding of Al6061 alloy. *Materials Science- Poland*, 39(1), 1–14. <https://doi.org/10.2478/msp-2021-0001>
- The Welding Institute. (n.d.-a). *Diffusion Bonding*. <https://www.twi-global.com/what-we-do/our-processes/diffusion-bonding>
- The Welding Institute. (n.d.-b). *Friction Welding of Plastics*. <https://www.twi-global.com/technical-knowledge/job-knowledge/friction-welding-of-plastics-059>
- The Welding Institute. (n.d.-c). *What is Friction Welding?* [https://www.twi-global.com/technical-knowledge/faqs/faq-what-is-friction-welding#:~:text=The way by which the,rotary friction welding \(RFW\).](https://www.twi-global.com/technical-knowledge/faqs/faq-what-is-friction-welding#:~:text=The way by which the,rotary friction welding (RFW).)
- Uday, M. B., Fauzi, M. N. A., Zuhailawati, H., & Ismail, A. B. (2010). Advances in friction welding process: A review. *Science and Technology of Welding and Joining*,

15(7), 534–558. <https://doi.org/10.1179/136217110X12785889550064>

- Udayakumar, T., Raja, K., Tanksale Abhijit, A., & Sathiya, P. (2013). Experimental investigation on mechanical and metallurgical properties of super duplex stainless steel joints using friction welding process. *Journal of Manufacturing Processes*, 15(4), 558–571. <https://doi.org/10.1016/j.jmapro.2013.06.010>
- United Nations. (n.d.). *Net zero coalition*. United Nations. Retrieved December 7, 2022, from <https://www.un.org/en/climatechange/net-zero-coalition#:~:text=Currently%2C%20the%20Earth%20is%20already,reach%20net%20zero%20by%202050>.
- V.R. Dave, M.J. Cola, M.J. Hussien, Heat generation in the inertia welding of dissimilar tubes, *Weld. Res. Suppl.* (2001) 246s–252s.
- Wahyudin, Kharisma, A., Murphiyanto, R. D. J., Perdana, M. K., & Kasih, T. P. (2018). Application of Taguchi method and ANOVA in the optimization of dyeing process on cotton knit fabric to reduce re-dyeing process. *IOP Conference Series: Earth and Environmental Science*, 109(1). <https://doi.org/10.1088/1755-1315/109/1/012023>
- Walley, S. M., & Field, J. E. (1994). Strain Rate Sensitivity of Polymers in Compression from Low to High Rates. In *DYMAT Journal* (Vol. 1, Issue 3, pp. 211–227).
- Wang, F. F., Li, W. Y., Li, J. L., & Vairis, A. (2014). Process parameter analysis of inertia friction welding nickel-based superalloy. *International Journal of Advanced Manufacturing Technology*, 71(9–12), 1909–1918. <https://doi.org/10.1007/s00170-013-5569-6>
- Wang, G., Li, J., Wang, W., Xiong, J., & Zhang, F. (2018). Study on the effect of energy-input on the joint mechanical properties of rotary friction-welding. *Metals*, 8(11). <https://doi.org/10.3390/met8110908>
- Wang, L., Preuss, M., Withers, P. J., Baxter, G., & Wilson, P. (2005). Energy-input-based finite-element process modeling of inertia welding. *Metallurgical and Materials Transactions B: Process Metallurgy and Materials Processing Science*, 36(4), 513–

523. <https://doi.org/10.1007/s11663-005-0043-y>

- Wang, K. K. and Lin, W. (1974) Flywheel friction welding research. *Weld. J.*, 53, 233–242.
- WANG K. K. & NAGAPPAN P. (1970). Transient Temperature Distribution in Inertia Welding of Steels. *Weld J (NY)*, 49(9), 419–426.
- Wolf, A., Henes, D., Bogdanski, S., Lutz, T., & Krämer, E. (2013). Statistical analysis of parameter variations using the taguchi method. *Notes on Numerical Fluid Mechanics and Multidisciplinary Design*, 122, 247–264. [https://doi.org/10.1007/978-3-642-36185-2\\_10](https://doi.org/10.1007/978-3-642-36185-2_10)
- Woo, M. W., Wong, P., Tang, Y., Triacca, V., Gloor, P. E., Hrymak, A. N., & Hamielec, A. E. (1995). Melting behavior and thermal properties of high density polyethylene. *Polymer Engineering and Science*, 35(2), 151–156. <https://doi.org/10.1002/pen.760350205>
- Yang, L. (2010). Modelling of the Inertia Welding of Inconel 718. *Department of Metallurgy and Materials, January*, 160. <http://theses.bham.ac.uk/760/>
- Yang, W. H., & Tarng, Y. S. (1998). Design optimization of cutting parameters for turning operations based on the Taguchi method. *Journal of Materials Processing Technology*, 84(1–3), 122–129. [https://doi.org/10.1016/S0924-0136\(98\)00079-X](https://doi.org/10.1016/S0924-0136(98)00079-X)
- Z. Liwen et al. (2004). Numerical simulation of inertia friction welding process of GH4169 alloy. *Journal De Physique IV*, 120, 681–687. <https://doi.org/10.1051/jp4:2004120078>
- Zerilli, F. J., & Armstrong, R. W. (2007). A constitutive equation for the dynamic deformation behavior of polymers. *Journal of Materials Science*, 42(12), 4562–4574. <https://doi.org/10.1007/s10853-006-0550-5>
- Zhang, K., Li, W., Zheng, Y., Yao, W., & Zhao, C. (2021). Compressive properties and

constitutive model of semicrystalline polyethylene. *Polymers*, 13(17), 1–18.  
<https://doi.org/10.3390/polym13172895>

Zhang, L. W., Pei, J. B., Zhang, Q. Z., Liu, C. D., Zhu, W. H., Qu, S., & Wang, J. H. (2007). The coupled fem analysis of the transient temperature field during inertia friction welding of GH4169 alloy. *Acta Metallurgica Sinica (English Letters)*, 20(4), 301–306. [https://doi.org/10.1016/S1006-7191\(07\)60043-X](https://doi.org/10.1016/S1006-7191(07)60043-X)

Zhang, Q. Z., Zhang, L. W., Liu, W. W., Zhang, X. G., Zhu, W. H., & Qu, S. (2006). 3D rigid viscoplastic FE modelling of continuous drive friction welding process. *Science and Technology of Welding and Joining*, 11(6), 737–743.  
<https://doi.org/10.1179/174329306X153222>



# APPENDIX

## APPENDIX A: Flow Stress Data

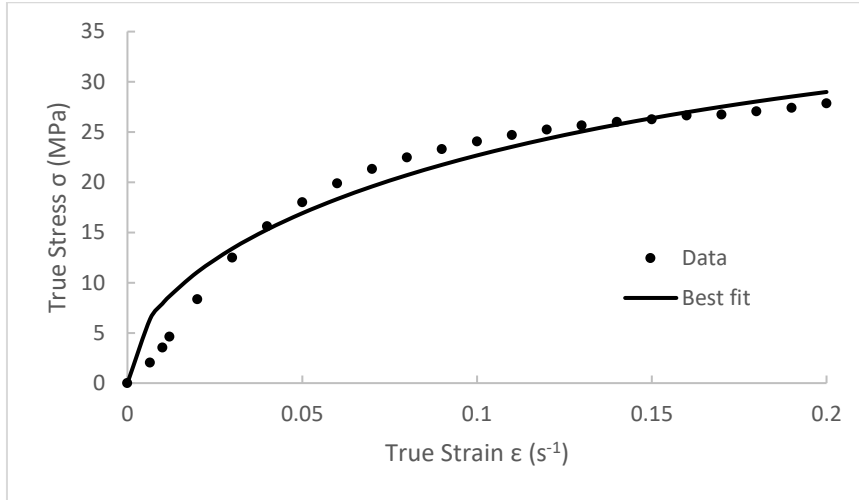


Figure 32 - Model Fit at 25°C and 0.001s<sup>-1</sup>

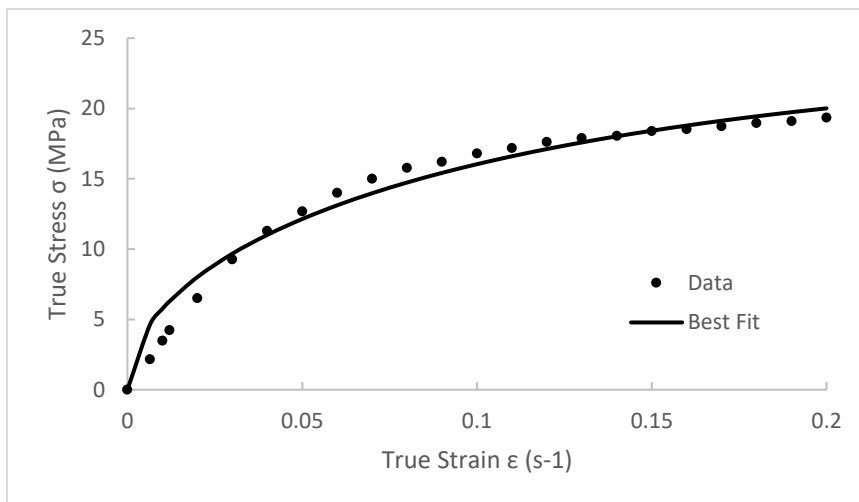


Figure 33 - Model Fit at 50°C and 0.001s<sup>-1</sup>

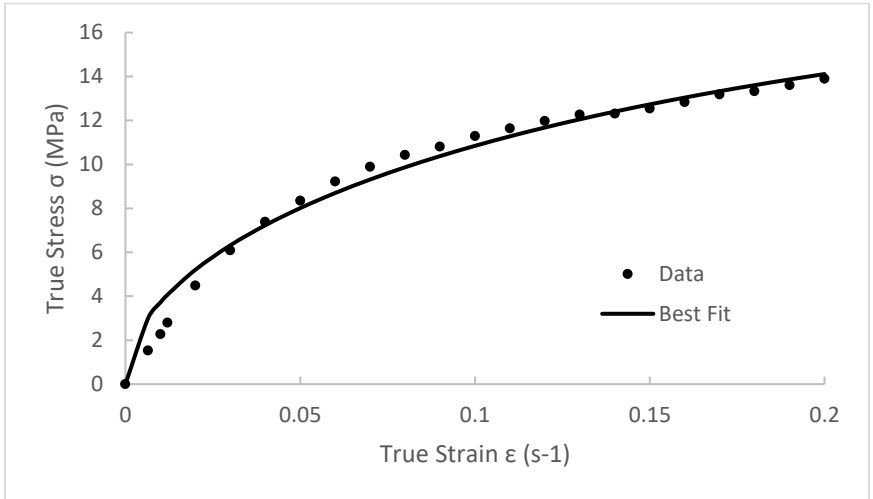


Figure 34 - Model Fit at 70°C and 0.001s<sup>-1</sup>

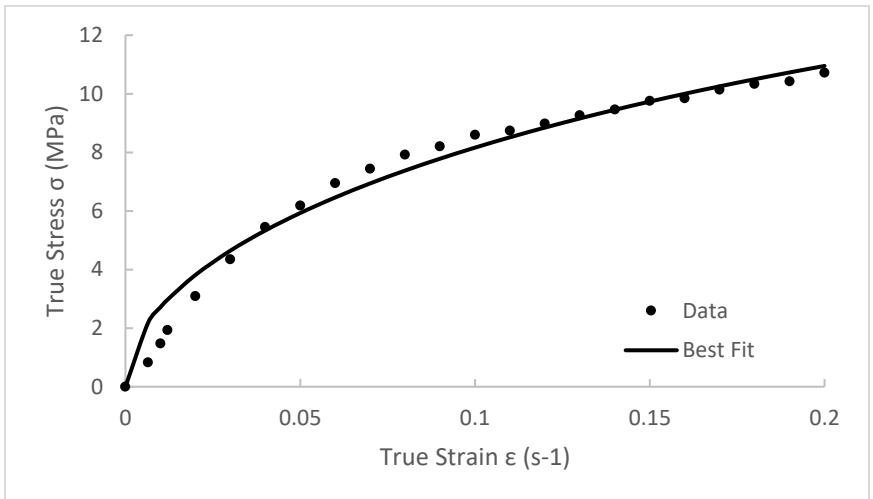


Figure 35 - Model Fit at 90°C and 0.001s<sup>-1</sup>

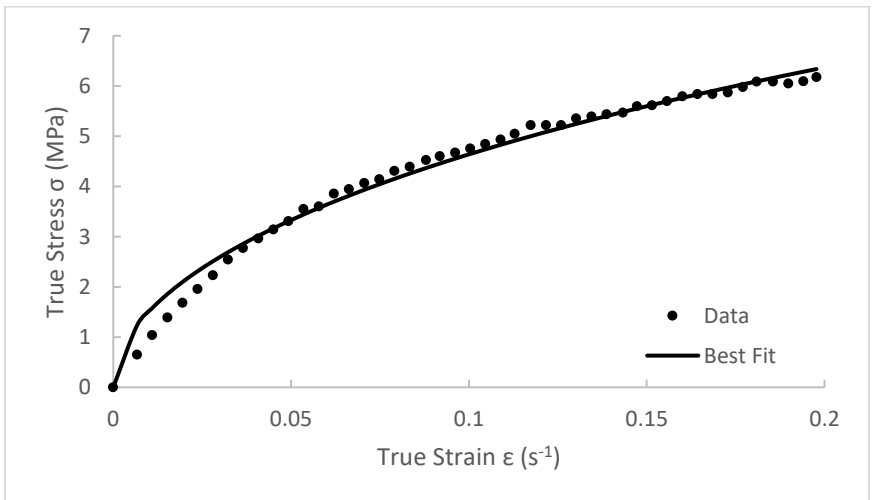


Figure 36 - Model Fit at 120°C and 0.001s<sup>-1</sup>

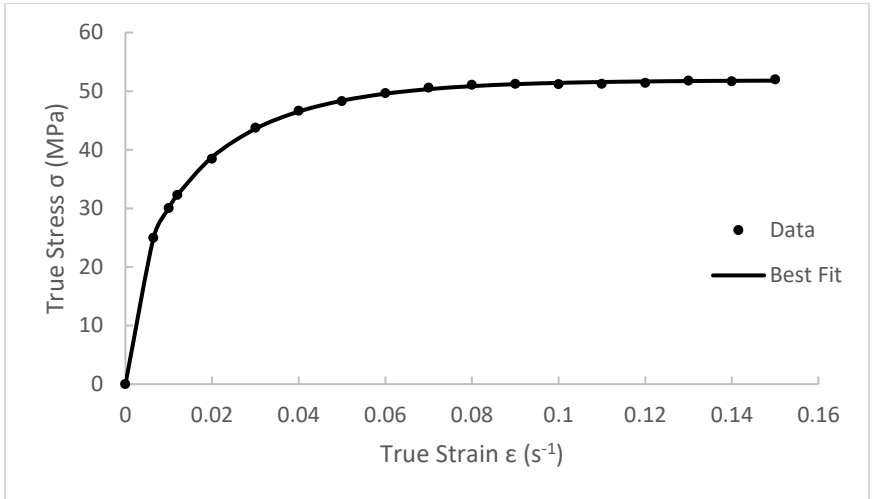


Figure 37 - Model Fit at 25°C and 935s<sup>-1</sup>

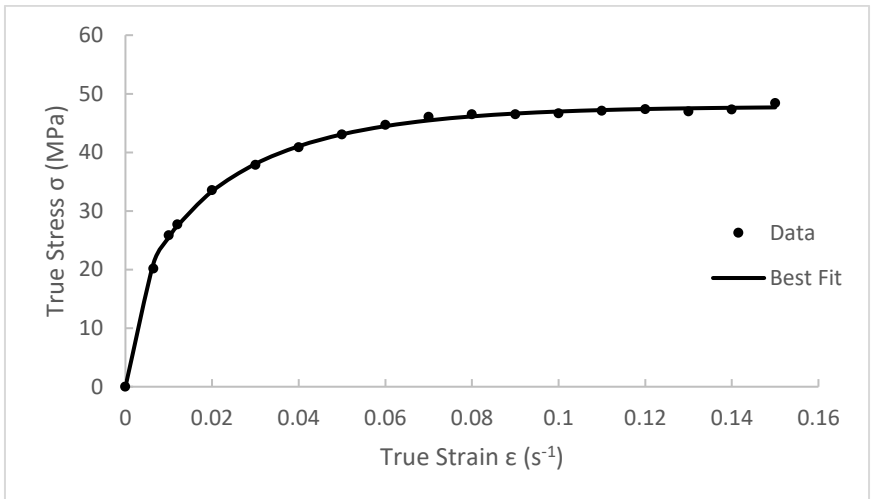


Figure 38 - Model Fit at 50°C and 935s<sup>-1</sup>

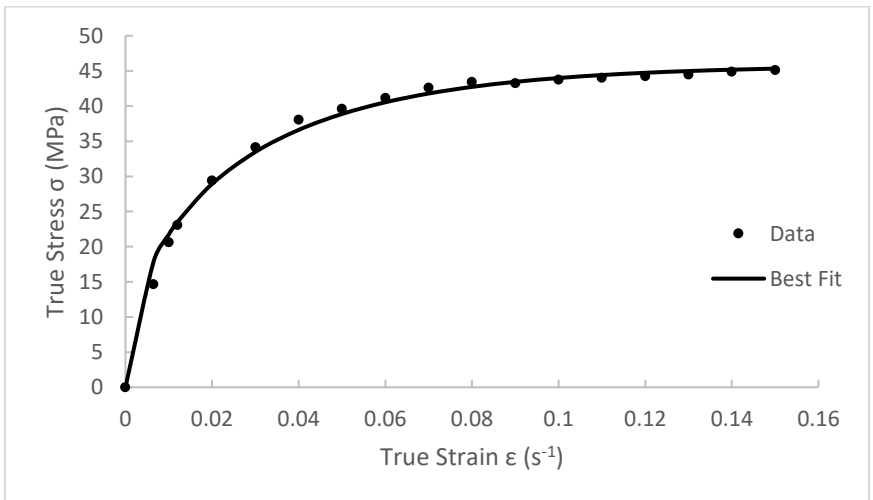


Figure 39 - Model Fit at 70°C and 935s<sup>-1</sup>

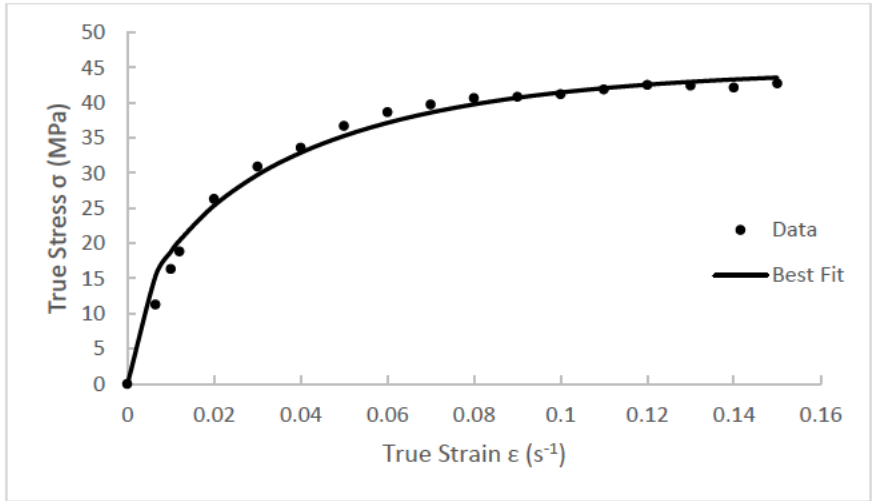


Figure 40 - Model Fit at 90°C and 935s<sup>-1</sup>

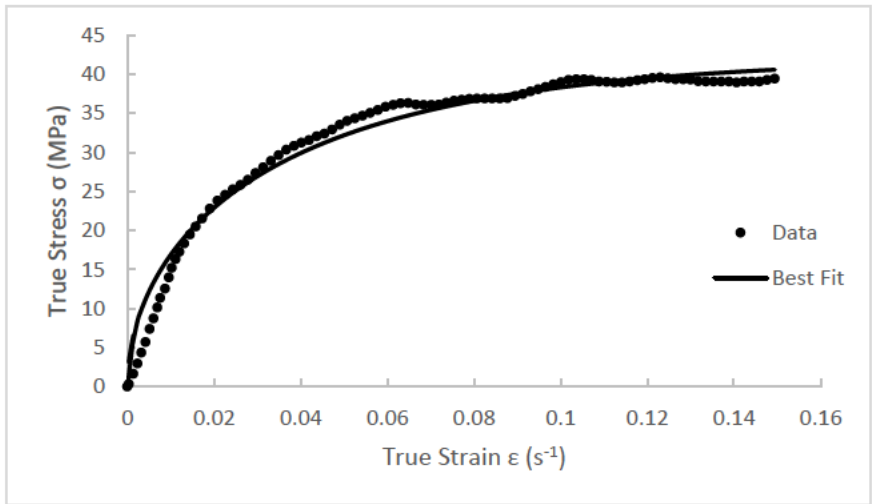


Figure 41 - Model Fit at 120°C and 935s<sup>-1</sup>

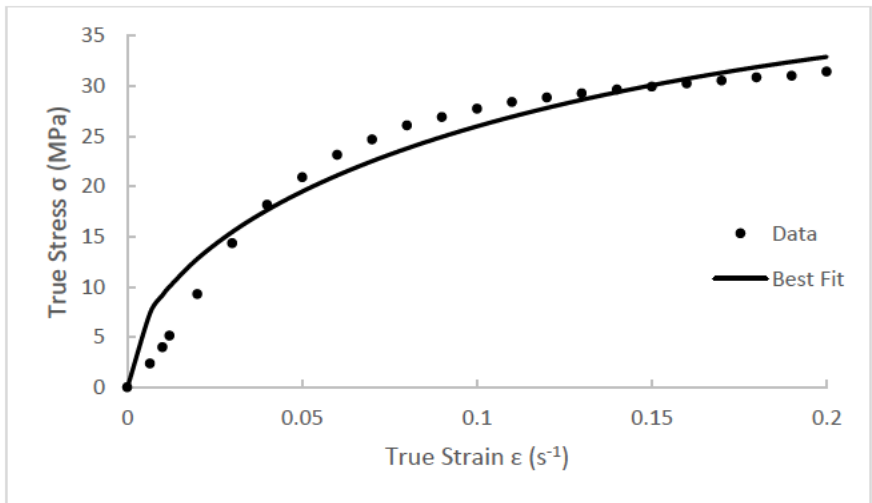


Figure 42 - Model Fit at 25°C and 0.01s<sup>-1</sup>

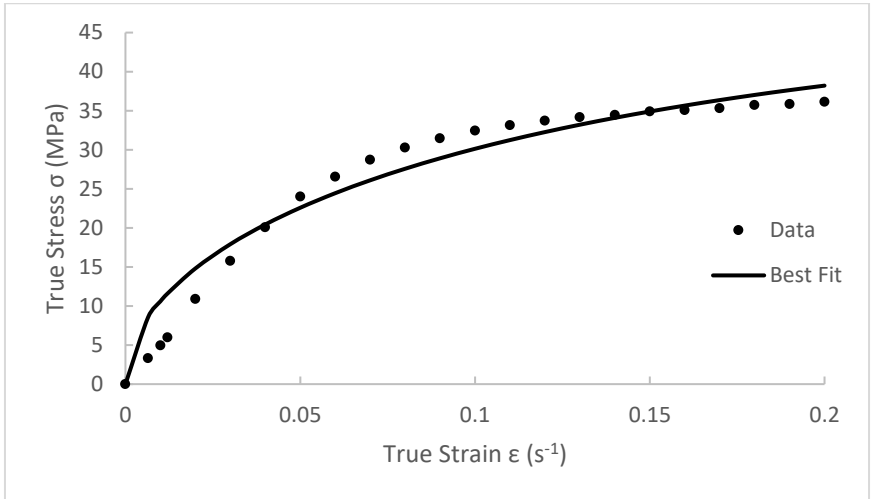


Figure 43 - Model Fit at 25°C and 0.1s<sup>-1</sup>

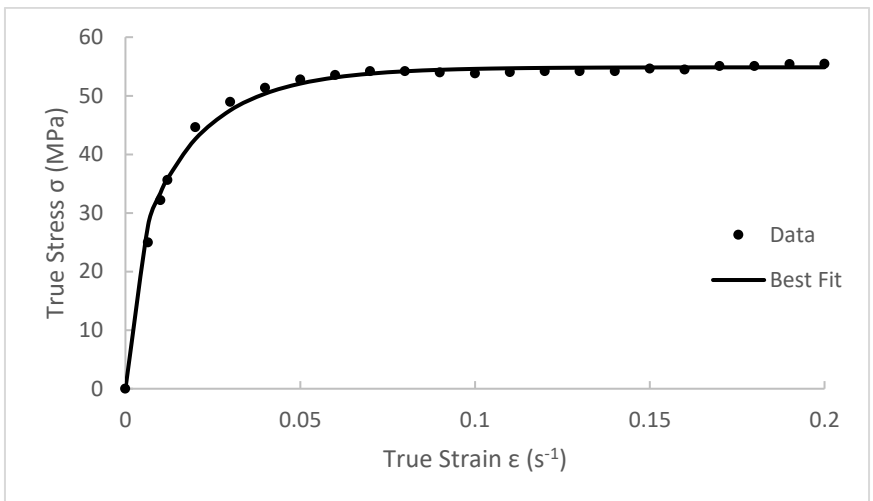


Figure 44 - Model Fit at 25°C and 2209s<sup>-1</sup>

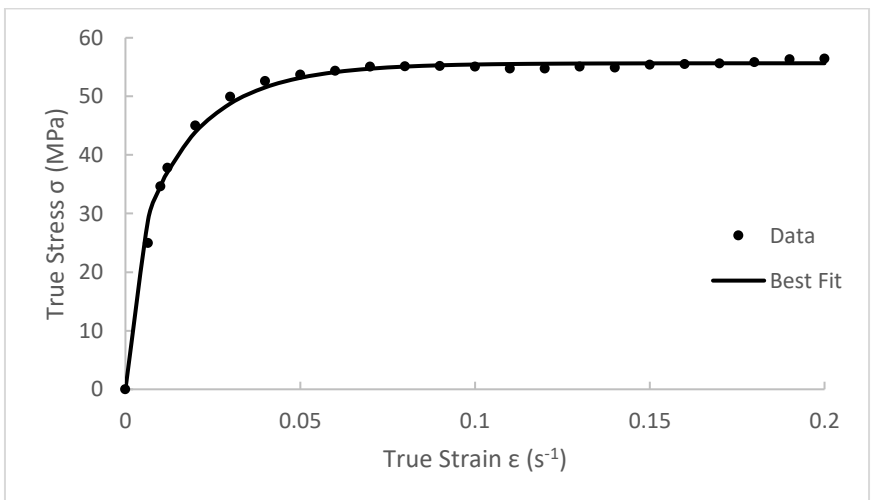
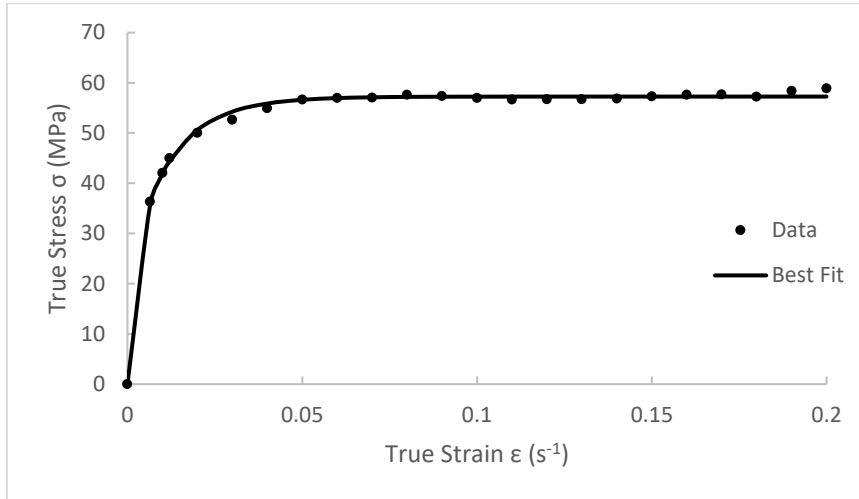


Figure 45 - Model Fit at 25°C and 2900s<sup>-1</sup>



*Figure 46 - Model Fit at 25°C and 5450s<sup>-1</sup>*

Table 14 - Zerilli Armstrong model constants extrapolated to higher strain rates at different temperatures

Temperature (°C)	Strain rate (s <sup>-1</sup> )	C	ε <sub>r</sub>
50	0.001	58.309	0.171
	0.01	75.648	0.127
	0.1	98.152	0.095
	10	165.234	0.053
70	0.001	37.476	0.273
	0.01	50.822	0.198
	0.1	68.921	0.143
	10	126.752	0.075
90	0.001	27.257	0.449
	0.01	37.956	0.313
	0.1	52.866	0.218
	10	102.560	0.106
120	0.001	15.119	0.818
	0.01	22.818	0.525
	0.1	34.425	0.336
	10	78.355	0.137
150	0.001	8.863	1.123
	0.01	13.980	0.727
	0.1	22.049	0.469
	10	54.852	0.196
180	0.001	5.165	1.794
	0.01	8.610	1.125
	0.1	14.351	0.705
	10	39.873	0.277
210	0.001	3.010	2.864
	0.01	5.302	1.743
	0.1	9.341	1.060
	10	28.985	0.392
240	0.001	1.754	4.573
	0.01	3.266	2.699
	0.1	6.080	1.593
	10	21.070	0.555
280	0.001	0.854	8.535
	0.01	1.711	4.829
	0.1	3.429	2.741
	10	13.771	0.883
350	0.001	0.242	25.438
	0.01	0.552	13.441
	0.1	1.259	7.103
	10	6.543	1.984
500	0.001	0.016	264.073
	0.01	0.049	119.755
	0.1	0.147	54.487
	10	1.328	11.280

Table 15 - Flow Stress Data at 25°C

Strain	Strain rate (sec <sup>-1</sup> )			
	0.001	0.01	0.1	10
<b>0</b>	20.350	23.780	28.030	35.500
<b>0.01</b>	21.521	24.322	28.295	35.584
<b>0.02</b>	21.967	24.796	28.748	36.603
<b>0.03</b>	22.516	25.401	29.339	37.663
<b>0.04</b>	23.203	26.225	30.371	39.329
<b>0.05</b>	24.095	26.909	31.402	40.871
<b>0.06</b>	25.056	28.110	32.627	42.054
<b>0.075</b>	26.257	29.482	34.291	43.346
<b>0.1</b>	27.938	31.356	36.451	44.650
<b>0.125</b>	29.242	32.827	37.357	45.457
<b>0.15</b>	30.237	33.925	39.433	45.963
<b>0.17</b>	31.027	34.707	40.394	46.235
<b>0.2</b>	32.056	35.831	41.733	46.605
<b>0.5</b>	36.312	40.196	46.579	47.155
<b>1</b>	37.446	41.185	46.607	48.132
<b>1.4</b>	37.584	41.256	46.622	48.187

Table 16 - Flow Stress Data at 50°C

Strain	Strain rate (sec <sup>-1</sup> )			
	0.001	0.01	0.1	10
<b>0</b>	13.310	17.150	20.990	28.670
<b>0.01</b>	13.755	18.120	21.184	30.442
<b>0.02</b>	14.442	18.483	21.604	30.957
<b>0.03</b>	15.299	18.922	22.177	31.617
<b>0.04</b>	16.145	19.430	22.831	32.406
<b>0.05</b>	16.746	20.068	23.568	33.388
<b>0.06</b>	17.337	20.587	24.386	34.037
<b>0.075</b>	18.074	21.427	25.344	35.025
<b>0.1</b>	19.125	22.608	26.678	36.276
<b>0.125</b>	19.943	23.521	27.594	37.000
<b>0.15</b>	20.510	24.163	28.301	37.420
<b>0.17</b>	20.925	24.526	28.610	37.701
<b>0.2</b>	21.550	25.063	29.008	37.818
<b>0.5</b>	23.696	26.811	30.237	38.151
<b>1</b>	24.059	26.994	30.319	38.181
<b>1.4</b>	24.094	26.975	30.289	38.145



Table 17 - Flow Stress Data at 70°C

<b>Strain</b>	<b>Strain rate (sec<sup>-1</sup>)</b>			
	<b>0.001</b>	<b>0.01</b>	<b>0.1</b>	<b>10</b>
<b>0</b>	8.170	12.010	15.850	23.530
<b>0.01</b>	8.652	12.859	15.960	25.212
<b>0.02</b>	9.390	13.228	16.378	25.876
<b>0.03</b>	10.103	13.671	16.870	26.713
<b>0.04</b>	10.768	14.114	17.510	27.648
<b>0.05</b>	11.284	14.656	18.174	28.484
<b>0.06</b>	11.801	15.098	18.814	29.493
<b>0.075</b>	12.466	15.837	19.774	30.428
<b>0.1</b>	13.376	16.845	21.029	31.634
<b>0.125</b>	14.139	17.731	21.988	32.569
<b>0.15</b>	14.680	18.346	22.702	33.159
<b>0.17</b>	15.148	18.912	23.219	33.529
<b>0.2</b>	15.738	19.429	23.711	33.873
<b>0.5</b>	18.494	21.988	25.802	34.636
<b>1</b>	19.429	22.579	26.073	34.685
<b>1.4</b>	19.601	22.603	26.048	34.660

Table 18 - Flow Stress Data at 90°C

<b>Strain</b>	<b>Strain rate (sec<sup>-1</sup>)</b>			
	<b>0.001</b>	<b>0.01</b>	<b>0.1</b>	<b>10</b>
<b>0</b>	6.180	10.020	13.860	21.062
<b>0.01</b>	6.430	10.477	14.666	21.540
<b>0.02</b>	7.043	10.762	14.931	21.757
<b>0.03</b>	7.717	11.089	15.176	22.574
<b>0.04</b>	8.228	11.539	15.462	23.514
<b>0.05</b>	8.677	11.927	15.769	24.760
<b>0.06</b>	9.127	12.233	16.136	25.762
<b>0.075</b>	9.678	12.703	16.647	26.987
<b>0.1</b>	10.454	13.703	17.688	28.581
<b>0.125</b>	11.107	14.541	18.648	29.684
<b>0.15</b>	11.638	15.133	19.424	30.542
<b>0.17</b>	12.169	15.602	20.078	30.909
<b>0.2</b>	12.638	16.276	20.649	31.480
<b>0.5</b>	15.738	19.580	23.769	33.211
<b>1</b>	17.464	20.876	24.555	33.272
<b>1.4</b>	17.904	21.113	24.607	33.281

Table 19 - Flow Stress Data at 120°C

<b>Strain</b>	<b>Strain rate (sec<sup>-1</sup>)</b>			
	<b>0.001</b>	<b>0.01</b>	<b>0.1</b>	<b>10</b>
<b>0</b>	2.180	6.020	8.400	17.540
<b>0.01</b>	3.410	6.029	8.472	17.771
<b>0.02</b>	3.822	6.294	8.972	18.360
<b>0.03</b>	4.175	6.647	9.325	18.831
<b>0.04</b>	4.529	6.971	9.708	19.449
<b>0.05</b>	4.823	7.324	10.032	20.214
<b>0.06</b>	5.088	7.619	10.532	20.832
<b>0.075</b>	5.441	8.001	11.238	21.891
<b>0.1</b>	5.971	8.590	12.180	23.362
<b>0.125</b>	6.441	9.237	13.004	24.451
<b>0.15</b>	6.765	9.708	13.681	25.334
<b>0.17</b>	7.089	10.120	14.122	25.923
<b>0.2</b>	7.471	10.620	14.769	26.423
<b>0.5</b>	9.973	13.681	18.095	28.748
<b>1</b>	11.886	15.505	19.537	29.013
<b>1.4</b>	12.621	16.094	19.831	29.013

Table 20 - Flow Stress Data at 150°C

<b>Strain</b>	<b>Strain rate (sec<sup>-1</sup>)</b>			
	<b>0.001</b>	<b>0.01</b>	<b>0.1</b>	<b>10</b>
<b>0</b>	1.750	2.390	3.750	9.140
<b>0.01</b>	1.948	3.004	4.479	10.598
<b>0.02</b>	2.218	3.397	5.163	12.070
<b>0.03</b>	2.440	3.765	5.699	13.195
<b>0.04</b>	2.636	4.060	6.152	14.175
<b>0.05</b>	2.808	4.330	6.570	14.969
<b>0.06</b>	2.980	4.576	6.925	15.661
<b>0.075</b>	3.202	4.896	7.422	16.567
<b>0.1</b>	3.522	5.363	8.118	17.826
<b>0.125</b>	3.793	5.781	8.679	18.817
<b>0.15</b>	4.014	6.126	9.163	19.568
<b>0.17</b>	4.211	6.372	9.524	20.025
<b>0.2</b>	4.458	6.741	10.011	20.708
<b>0.5</b>	6.136	8.984	12.793	23.572
<b>1</b>	7.550	10.594	14.395	24.210
<b>1.4</b>	8.175	11.195	14.816	24.280

Table 21 - Flow Stress Data at 180°C

<b>Strain</b>	<b>Strain rate (sec<sup>-1</sup>)</b>			
	<b>0.001</b>	<b>0.01</b>	<b>0.1</b>	<b>10</b>
<b>0</b>	0.890	1.480	2.450	6.720
<b>0.01</b>	1.081	1.797	3.024	8.277
<b>0.02</b>	1.250	2.091	3.476	9.372
<b>0.03</b>	1.385	2.317	3.829	10.289
<b>0.04</b>	1.514	2.523	4.153	10.976
<b>0.05</b>	1.622	2.690	4.428	11.613
<b>0.06</b>	1.717	2.837	4.683	12.173
<b>0.075</b>	1.845	3.053	5.007	12.912
<b>0.1</b>	2.049	3.367	5.498	13.982
<b>0.125</b>	2.218	3.641	5.920	14.822
<b>0.15</b>	2.360	3.867	6.263	15.434
<b>0.17</b>	2.476	4.034	6.528	15.918
<b>0.2</b>	2.638	4.289	6.891	16.580
<b>0.5</b>	3.725	5.905	9.155	19.692
<b>1</b>	4.739	7.263	10.758	20.821
<b>1.4</b>	5.254	7.866	11.342	20.981

Table 22 - Flow Stress Data at 210°C

<b>Strain</b>	<b>Strain rate (sec<sup>-1</sup>)</b>			
	<b>0.001</b>	<b>0.01</b>	<b>0.1</b>	<b>10</b>
<b>0</b>	0.520	0.910	1.600	5.650
<b>0.01</b>	0.586	1.107	1.938	6.475
<b>0.02</b>	0.701	1.279	2.232	7.207
<b>0.03</b>	0.783	1.427	2.498	7.871
<b>0.04</b>	0.849	1.553	2.706	8.457
<b>0.05</b>	0.915	1.668	2.886	8.950
<b>0.06</b>	0.981	1.759	3.066	9.388
<b>0.075</b>	1.063	1.897	3.303	9.957
<b>0.1</b>	1.178	2.091	3.624	10.797
<b>0.125</b>	1.277	2.274	3.925	11.507
<b>0.15</b>	1.359	2.423	4.151	12.035
<b>0.17</b>	1.441	2.571	4.339	12.438
<b>0.2</b>	1.540	2.697	4.636	13.038
<b>0.5</b>	2.212	3.816	6.359	16.076
<b>1</b>	2.897	4.839	7.800	17.590
<b>1.4</b>	3.287	5.372	8.421	17.920

Table 23 - Flow Stress Data at 240°C

<b>Strain</b>	<b>Strain rate (sec<sup>-1</sup>)</b>			
	<b>0.001</b>	<b>0.01</b>	<b>0.1</b>	<b>10</b>
<b>0</b>	0.300	0.560	1.050	4.140
<b>0.01</b>	0.349	0.661	1.320	4.971
<b>0.02</b>	0.415	0.775	1.518	5.550
<b>0.03</b>	0.467	0.865	1.680	6.040
<b>0.04</b>	0.510	0.945	1.822	6.453
<b>0.05</b>	0.543	1.017	1.935	6.842
<b>0.06</b>	0.576	1.083	2.054	7.189
<b>0.075</b>	0.628	1.168	2.215	7.629
<b>0.1</b>	0.694	1.291	2.432	8.265
<b>0.125</b>	0.756	1.400	2.636	8.789
<b>0.15</b>	0.808	1.495	2.802	9.265
<b>0.17</b>	0.851	1.575	2.934	9.624
<b>0.2</b>	0.908	1.675	3.124	10.114
<b>0.5</b>	1.324	2.418	4.363	12.900
<b>1</b>	1.760	3.157	5.502	14.651
<b>1.4</b>	2.020	3.564	6.062	15.199

Table 24 - Flow Stress Data at 280°C

<b>Strain</b>	<b>Strain rate (sec<sup>-1</sup>)</b>			
	<b>0.001</b>	<b>0.01</b>	<b>0.1</b>	<b>10</b>
<b>0</b>	0.120	0.295	0.590	3.030
<b>0.01</b>	0.154	0.341	0.740	3.576
<b>0.02</b>	0.187	0.400	0.855	3.930
<b>0.03</b>	0.210	0.449	0.950	4.270
<b>0.04</b>	0.233	0.492	1.032	4.538
<b>0.05</b>	0.252	0.531	1.104	4.793
<b>0.06</b>	0.269	0.564	1.173	5.020
<b>0.075</b>	0.292	0.610	1.262	5.331
<b>0.1</b>	0.328	0.679	1.396	5.798
<b>0.125</b>	0.361	0.741	1.511	6.152
<b>0.15</b>	0.384	0.790	1.613	6.491
<b>0.17</b>	0.407	0.833	1.695	6.760
<b>0.2</b>	0.437	0.889	1.803	7.128
<b>0.5</b>	0.651	1.300	2.577	9.366
<b>1</b>	0.883	1.738	3.350	11.139
<b>1.4</b>	1.022	1.989	3.774	11.850

Table 25 - Flow Stress Data at 350°C

<b>Strain</b>	<b>Strain rate (sec<sup>-1</sup>)</b>			
	<b>0.001</b>	<b>0.01</b>	<b>0.1</b>	<b>10</b>
<b>0</b>	0.034	0.095	0.250	1.830
<b>0.01</b>	0.045	0.112	0.285	1.980
<b>0.02</b>	0.056	0.133	0.327	2.150
<b>0.03</b>	0.064	0.148	0.361	2.286
<b>0.04</b>	0.071	0.162	0.389	2.414
<b>0.05</b>	0.075	0.174	0.418	2.541
<b>0.06</b>	0.078	0.185	0.443	2.652
<b>0.075</b>	0.087	0.201	0.476	2.813
<b>0.1</b>	0.095	0.222	0.523	3.017
<b>0.125</b>	0.105	0.242	0.569	3.229
<b>0.15</b>	0.113	0.260	0.608	3.416
<b>0.17</b>	0.118	0.274	0.639	3.561
<b>0.2</b>	0.127	0.292	0.680	3.748
<b>0.5</b>	0.185	0.430	0.986	5.074
<b>1</b>	0.255	0.579	1.316	6.340
<b>1.4</b>	0.297	0.669	1.513	6.994

Table 26 - Flow Stress Data at 500°C

<b>Strain</b>	<b>Strain rate (sec<sup>-1</sup>)</b>			
	<b>0.001</b>	<b>0.01</b>	<b>0.1</b>	<b>10</b>
<b>0</b>	0.002	0.007	0.029	0.546
<b>0.01</b>	0.003	0.009	0.034	0.572
<b>0.02</b>	0.003	0.011	0.039	0.598
<b>0.03</b>	0.004	0.012	0.043	0.621
<b>0.04</b>	0.004	0.013	0.047	0.642
<b>0.05</b>	0.005	0.014	0.050	0.667
<b>0.06</b>	0.005	0.015	0.053	0.688
<b>0.075</b>	0.005	0.017	0.057	0.721
<b>0.1</b>	0.006	0.019	0.063	0.765
<b>0.125</b>	0.007	0.021	0.068	0.807
<b>0.15</b>	0.007	0.022	0.072	0.845
<b>0.17</b>	0.008	0.023	0.076	0.871
<b>0.2</b>	0.008	0.025	0.081	0.911
<b>0.5</b>	0.012	0.038	0.119	1.218
<b>1</b>	0.017	0.052	0.161	1.563
<b>1.4</b>	0.019	0.061	0.187	1.773